

UNIVERSITÄT LEIPZIG

UNIVERSITY OF LEIPZIG
FACULTY OF PHYSICS AND EARTH SCIENCES

DIPLOMA THESIS

Seasonal Dependence of Geometrical and Optical
Properties of Tropical Cirrus Determined from
Lidar, Radiosonde, and Satellite Observations over
the Polluted Tropical Indian Ocean (Maldives).

in partial fulfillment of the requirements for the degree of

Diplom-Meteorologe
(Graduate Meteorologist)

Submitted by
Patric Seifert
on January 30, 2006

Presented to
Prof. G. Tetzlaff and
Prof. J. Heintzenberg

Abstract

Cirrus clouds detected with a six-wavelength aerosol lidar in the tropical region of the Maldives (4.1° N, 73.3° E) were characterized in terms of seasonal geometrical, optical, and thermal properties. The dataset was collected during the Indian Ocean Experiment between February 1999 and March 2000. Cirrus visible optical depth, mean extinction coefficient, and lidar ratio were derived from the 532-nm elastic-backscatter lidar signals. Temperature information from radiosondes launched frequently at the lidar site was used to characterize the thermal structure of the tropical troposphere and the temperature dependence of the optical and geometrical cirrus properties. Descending stratospheric Kelvin waves were observed which seem to influence cirrus formation close to the tropopause. Deep convection is most likely responsible for the formation of cirrus below 14 km height. Cirrus clouds were detected during 51% of the time at altitudes between 7 and 18 km, but were on average located below altitudes reported in other tropical cirrus studies. Trajectories and satellite data providing outgoing longwave radiation and aerosol optical depth were used to characterize the source regions of the cirrus clouds and suggested that clouds were probably affected by anthropogenic pollution. An impact of pollution on the cirrus optical properties could not be quantified.

Zusammenfassung

Zirren, gemessen mit einem Sechswellenlängenlidar auf den tropischen Malediven (4.1° N, 73.3° O), wurden anhand ihrer saisonalen geometrischen, optischen und thermischen Eigenschaften charakterisiert. Der Datensatz entstand zwischen Februar 1999 und März 2000 bei Messungen im Rahmen des Indian Ocean Experiment. Optische Dicken, mittlere Extinktionskoeffizienten und Extinktion-zu-Rückstreuverhältnisse der Zirren wurden aus dem elastischen Lidarrückstreusignal bei 532 nm bestimmt. Von der Lidarstation aus gestartete Radiosonden lieferten Temperaturprofile, die zur Charakterisierung der tropischen Troposphäre und der Temperaturabhängigkeit der optischen und geometrischen Zirruseigenschaften verwendet wurden. Absinkende stratosphärische Kelvinwellen wurden beobachtet, die scheinbar die Bildung von Zirren in Tropopausennähe beeinflussen. In Höhen unter 14 km ist höchstwahrscheinlich hochreichende Konvektion für die Zirusbildung verantwortlich. In 51% der Messzeit wurden Zirren beobachtet, die sich üblicherweise in Höhen zwischen 7 und 18 km befanden, jedoch im Mittel tiefer lagen, als in anderen Studien über tropische Zirren berichtet wird. Anhand von Trajektorien und Satellitendaten, die Informationen zu ausgehender langwelliger Strahlung und optischen Dicken des Aerosols lieferten, wurden Quellregionen der Zirren charakterisiert und Indizien gefunden, die einen Einfluss von anthropogener Verschmutzung auf Zirren vermuten lassen. Ein quantitativer Nachweis für den Einfluss von Verschmutzung auf die optischen Zirruseigenschaften konnte nicht gefunden werden.

Table of Contents

1	Introduction	1
2	Indian Ocean Experiment	4
2.1	Description of the Experiment	4
2.2	Lidar System	6
2.3	Radio Soundings	7
2.4	Satellite Data	8
2.5	Trajectories	10
3	Lidar Data Analysis	12
3.1	Lidar Principle	12
3.2	Determination of Cloud Base and Top Height	13
3.3	Determination of Cirrus Cloud Optical Properties	15
3.3.1	Klett Method	17
3.3.2	Raman Lidar Method	20
3.4	Error Discussion	21
3.4.1	Reference-Value Estimate	21
3.4.2	Lidar-Ratio Estimate	23
3.4.3	Error due to Multiple Scattering	26
4	Tropical Cirrus	28
4.1	Basic Cirrus Properties	28
4.2	Cirrus Formation Processes	30
4.3	Anthropogenic Pollution and Cirrus	35
4.4	Are There Indications for Polluted Cirrus Clouds?	36
5	Results and Discussion	43
5.1	Geometrical Cirrus Properties	46

5.1.1	Results	46
5.1.2	Discussion	49
5.2	Optical Cirrus Properties	55
5.2.1	Results	55
5.2.2	Discussion	58
6	Summary	69
A	List of Abbreviations	72
	Bibliography	73

Chapter 1

Introduction

Since the early 1980's cirrus clouds do not any longer just play a role for the forecast of upcoming fronts or as scenic phenomena in the sky creating impressive optical rarities like halos, arcs, and sun dogs. As scientists got increasingly concerned about climate change, research programs were established which also focused on the global cloud system and were of use for the setup of first cirrus cloud climatologies. In 1984 the establishment of the International Cloud Climatology Project (ISCCP, Schiffer and Rossow 1983) providing a five-year global cloud climatology marked the first step into this direction (Lynch et al. 2002). In 1986, Liou published a review paper that documented the current understanding and knowledge about cirrus. The collection of results from previous publications revealed the important role cirrus clouds play for the weather and climate in a global perspective.

20% to 35% of the globe are regularly covered with cirrus (Liou 1986; Wylie et al. 1994). The highest rates of coverage can be found in the area of the intertropical convergence zone (ITCZ) with an average value of 45% (Wylie et al. 1994). Such values lead to a significant impact of cirrus clouds on local meteorological processes as well as on the global heat budget of the atmosphere. The role cirrus clouds play for the radiation balance of the earth-atmosphere system is determined by the greenhouse-versus-albedo effect (Liou 1986; Wylie et al. 1994). Ice clouds modify the incoming solar radiation by scattering and absorption and the outgoing infrared radiation by absorption and emission (Wendisch et al. 2005). Whereas the scattering of solar radiation causes a netto cooling effect for the earth's surface, the absorption and emission of infrared radiation leads to a trapping of energy in the earth-atmosphere system. The way in which these two effects interact and thus influence the radiation balance of the atmosphere strongly depends on the optical properties, height, thickness, and temperature of the cirrus layers. The influence of various feedback effects in conjunction

with other clouds (i.e., convective clouds), pollution, and large-scale processes, such as changes in the vertical distribution of radiative heating (Stephens 2002) or sea surface temperature (Ramanathan and Collins 1991), is not yet completely understood.

Several field campaigns have been carried out in various regions of the globe to improve the knowledge on the climate impact of cirrus clouds. The main instruments used to gather information on the high, cold, and often tenuous clouds are satellites, aircraft, radar (**radio detection and ranging**), and lidar (**light detection and ranging**). Satellite data cover large areas of the globe, but usually have a low spatial and vertical resolution. Aircraft can only probe a small volume of a cloud, but they are of importance for the collection of information on the microphysical properties of cloud particles. Measurements with a high vertical and temporal resolution can only be achieved with radar and lidar. Since the lidar technique works at wavelengths in the ultraviolet, visible, and infrared range, observed optical effects and properties of the probed air column can easily be applied to solar radiation without the risk of high errors.

Because of a limited number of vertically and temporally highly resolved measurements of microphysical properties, especially in the tropical region, an accurate determination of the radiative forcing of cirrus clouds can still hardly be assessed. With measurements in Nauru (Comstock et al. 2002), Réunion Island (Cadet et al. 2003), eastern central India (Sivakumar et al. 2003), and the Seychelles (Pace et al. 2003), representing the most prominent campaigns, a few regions of the tropics have already been subject of climatological cirrus studies.

This work contributes extensive cirrus cloud statistics and information about cirrus cloud optical properties at the Maldives in the Indian Ocean. In the scope of the Indian Ocean Experiment (INDOEX) the transportable lidar system of the Leibniz Institute for Tropospheric Research (IFT, Leipzig, Germany) performed more than 30,000 minutes of multi-wavelength backscatter, extinction, and depolarization profiling at Hulule (4° N, 73° E). Four individual field campaigns have been carried out in February/March 1999, July 1999, October 1999, and March 2000 so that the underlying dataset covers both, two seasons of the dry northeast monsoon as well as one season of the rainy southwest monsoon. During the northeast monsoon high concentrations of anthropogenic aerosol particles have been observed in the lower troposphere over the Maldives (Franke et al. 2003). As an additional goal, this work uses lidar, radio soundings, satellite data, and backward trajectories to investigate whether there is an evidence for the impact of anthropogenic pollution on cirrus clouds in the region of the Maldives.

Chapter 2 gives an introduction to the INDOEX field campaign and the equipment that provided the dataset for this study. The theoretical basics of the lidar data analysis methods as well as an error discussion can be found in Chapter 3. Information on cirrus formation processes and the possible impact of anthropogenic pollution on these clouds are presented in Chapter 4. Results of the data analysis, including statistics of macrophysical and optical cirrus cloud properties, are documented in Chapter 5. A summary is given in Chapter 6.

Chapter 2

Indian Ocean Experiment

2.1 Description of the Experiment

During the 1990's climate model diagnostics revealed the large uncertainty of the role aerosols play for the global climate. The demand for field campaigns grew. Results of field studies are a basic need for model validation. The tropical Indian Ocean is a unique region providing optimal conditions for investigations of aerosol particles and effects triggered by them.

The monsoon climate in the INDOEX region is characterized by the presence of two completely different air masses, clean maritime air south of the ITCZ and polluted continental air north of the ITCZ (see Fig. 2.1). Maritime, so-called pristine air, provides suitable conditions for measurements of the background aerosol not influenced by anthropogenic emissions at all. The continental aerosol, in turn, gives scientists the opportunity to track anthropogenic pollution from its source and to follow the long-range transport over the Asian continent and the Indian Ocean to the ITCZ. There, finally both air masses collide. At the ITCZ convergence, lifting and mixing of air masses are the dominating processes. Thus the ITCZ represents a unique place for investigations of aerosol particle transformations and indirect aerosol effects like the Twomey effect and other aerosol–cloud interactions (Lohmann and Feichter 2005).

The circumstances mentioned above motivated the realization of the Indian Ocean Experiment (Ramanathan et al. 1996). The importance of this international field campaign is reflected in the high number of participating countries and institutions. A period of three years was used to prepare for the intensive field phase. A Pre-INDOEX research phase from 1995 to 1997 and the first INDOEX field phase in 1998 were used to collect data and ideas useful for a successful realization of the intensive field phase which started in early 1999.

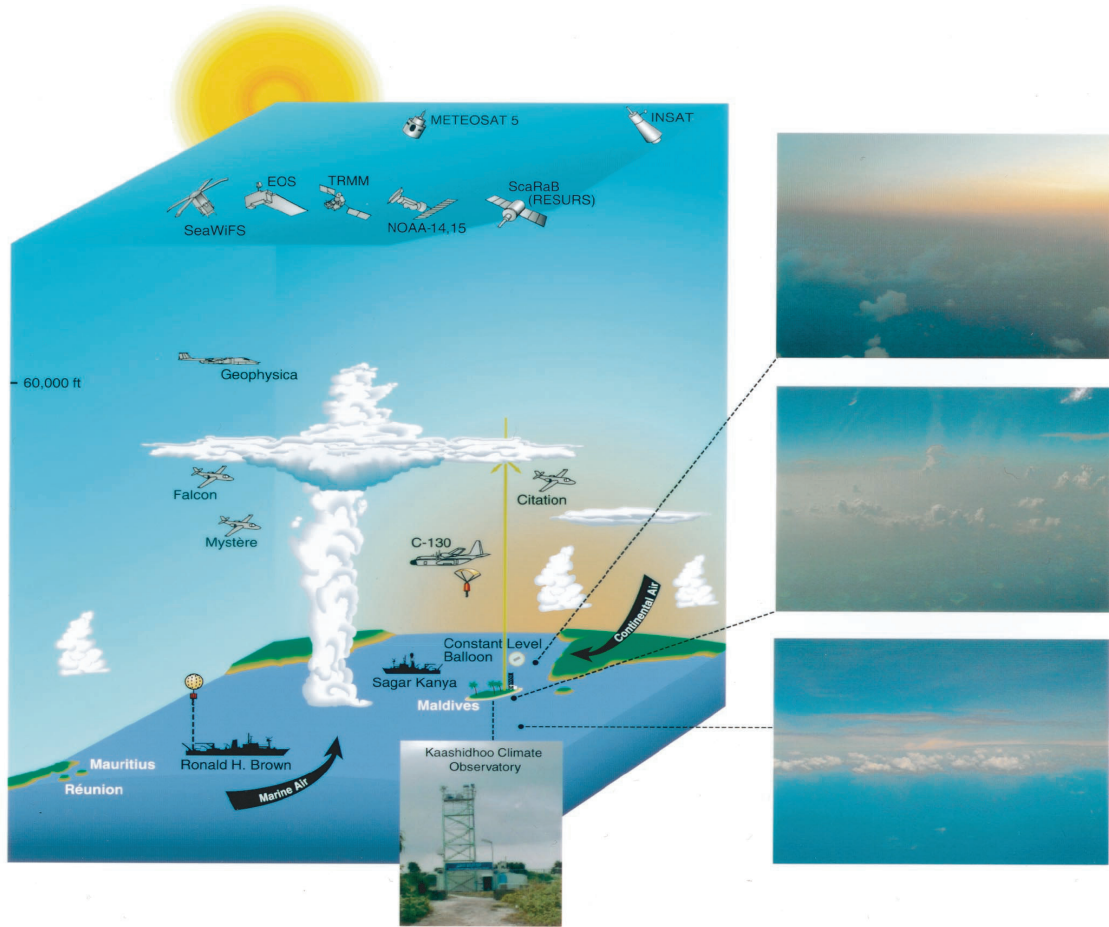


Figure 2.1: INDOEX—Region and Instrumentation (Ramanathan et al. 2001a).

During the intensive field phase from 15 February to 25 March 1999 about 50 research institutes from Europe, India, and the USA were involved in extensive measurement activities. Five aircraft probed air up to the lower stratosphere (the *C-130* of the National Center for Atmospheric Research, USA; the *Citation* from the Netherlands; the *Mystere* from France; the *Falcon* from the German Aerospace Center; the *Geophysica* from Russia). Two research vessels, the *Ronald H. Brown*, USA, and the *Sagar Kanya*, India, crossed the Indian Ocean. Ground stations were located at the Maldivian islands of Kaashidhoo (KCO) and Hulule, at Goa (India) and Dharward (India). Space-based satellite datasets of Meteosat 5, INSAT, ScaRaB, TRMM, NOAA 14 and 15 provided large-scale particle distributions and a meteorological overview of the INDOEX region. The IFT lidar, introduced in Sec. 2.2, was involved in three additional field campaigns. The time frames of all four campaigns are presented in Table 2.1.

Table 2.1: Time frames of the four INDOEX field campaigns conducted by the IFT Leipzig.

Campaign	Time frame	
	Date	Julian Day
Feb/Mar 1999	7 Feb–25 March 1999	31–83
July 1999	1–19 July 1999	181–199
October 1999	1–18 October 1999	274–290
March 2000	8–25 March 1999	67–84

The main goal of INDOEX was to characterize the anthropogenic Indo–Asian haze and to estimate the aerosol direct and indirect forcing on climatically relevant scales. Ramanathan et al. (2001a) published an article that reviews the knowledge gained with respect to this main objective. A summary of the lidar data analysis of IFT regarding the aerosol observations in the lower troposphere can be found in Franke et al. (2003), Franke (2003), and (Müller et al. 2003).

2.2 Lidar System

Most of the data used for this study were recorded by the containerized multi-wavelength aerosol lidar, developed and operated by the IFT. The lidar was located at Hulule (4° N, 73° E), the airport island of the Maldives. A detailed description of the system can be found in Althausen et al. (2000). A sketch of the lidar setup is shown in Fig. 2.2.

Two Nd:YAG and two dye lasers simultaneously emit pulses at 355, 400, 532, 710 (parallel polarized), 800, and 1064 nm with a repetition rate of 30 Hz. A beam-combination unit aligned the six laser beams onto one optical axis. The resulting beam is expanded by a factor of 10. The beam divergence reduces to less than 0.1 mrad in this way. This increases the diameter of the beams at 355, 532, and 1064 nm wavelength from about 10 to 100 mm and at 400, 710, and 800 nm wavelength from about 2.5 to 25 mm.

A scanning unit outside of the container, realized by a steerable mirror, permits measurements at zenith angles from -90° to 90° . During INDOEX typical scan angles (zenith angles) were 5° , 30° and 60° . Especially zenith angles of 30° , and 60° allow a high vertical resolution in the lower troposphere but reduce, in return, the maximum measurement altitude of the lidar.

A 0.53-m Cassegrain telescope collects the backscattered light. A beam-separation

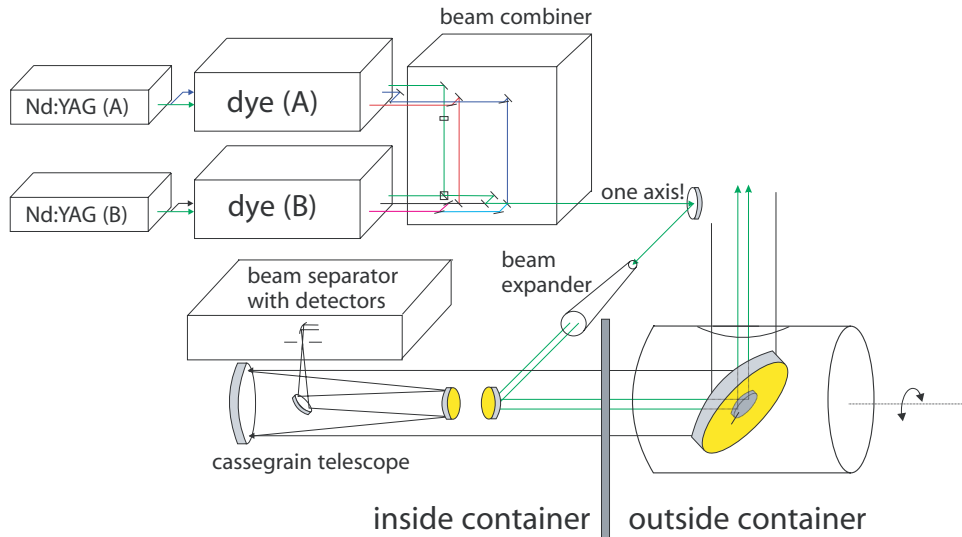


Figure 2.2: Setup of the six-wavelength lidar of the IFT.

unit separates the returned light into 11 channels with respect to wavelength and state of polarization. In addition to the elastic signals of the six emitted wavelengths, the inelastically scattered Raman signals of nitrogen at 387 nm (355 nm primary wavelength) and 607 nm (532 nm primary wavelength) as well as of water vapor at 660 nm (532 nm primary wavelength) are detected. A detection of Raman signals throughout the troposphere is only possible at night when the background signal is negligible. The 710-nm signal is split up into a parallel (co-) and a perpendicular (cross-) polarized channel. In this way, a vertical profile of the depolarization ratio is obtained. Photomultipliers amplify the signal of the detected photons. The amplified signals are acquired either in analog (400, 532, 710, 800, 1064 nm) or in photon-counting mode (355, 387, 532, 607, 660 nm).

From the lidar information of the 11 detected signals vertical profiles of particle backscatter and extinction coefficients at the six emitted wavelengths as well as the depolarization ratio at 710 nm can be obtained. When Raman signals are available vertical profiles of the particle lidar ratio (LR, extinction-to-backscatter ratio) can be calculated for 355 and 532 nm. The theoretical background of the analysis of lidar data is presented in Chapter 3.

2.3 Radio Soundings

Since there were no regular radio soundings available neither at Hulule nor in close distance to the island, radiosondes had to be launched directly from the lidar observa-

tion site. Between one and four radiosondes of the type Vaisala RS-80 were launched per day, resulting in a total number of 250 radiosonde ascents during the four field campaigns. The launch of the sondes usually was during lidar measurements, ensuring the availability of current meteorological data for each cirrus case. The Vaisala RS-80 radiosonde provides vertical profiles of pressure, height, temperature, and humidity. Before each launch a ground check had to be performed to assure a good calibration of the sensors. The vertical profiles delivered by the Vaisala RS-80 were in good agreement with the profiles of drop sondes, released by the *C-130*. The radiosondes reached altitudes of up to 25 km.

An example of a radiosonde temperature profile at 12:33 UTC (17:33 local time) on 16 March 1999 is shown in Fig. 2.3. The colored background of the graph shows a time-resolved vertical profile of the range-corrected 532-nm lidar signal (see Sec. 3.2). The lidar measurement was started at 12:22 UTC (17:22 local time) on 16 March 1999. Lapse-rate (WMO) tropopause¹ and minimum temperature are indicated by a red and a blue line, respectively. In the tropics the minimum temperature is also referred to as the cold-point tropopause (Highwood and Hoskins 1998).

2.4 Satellite Data

The main advantage of datasets obtained by satellites is that they provide a synopsis of atmospheric parameters covering vast regions of the globe. The question of which conditions characterized the area around the observation site can be answered in a convenient way by using satellite data. In the scope of this work data products from satellites helped solving two major questions:

1. How much aerosol in terms of optical depth was present in the INDOEX region at a specific time?
2. Where in the INDOEX region were zones with deep convection located?

The Advanced Very High Resolution Radiometer (AVHRR), carried by the polar-orbiting satellites NOAA 14 and 15, basically provides radiometric measurements. Based on this dataset information about aerosol optical depth as well as several additional atmospheric properties can be calculated (Ignatov and Stowe 2002; Ignatov et al. 2004). The retrieved aerosol optical depth represents a solution for the first

¹The lapse-rate tropopause, also referred to as the WMO tropopause, is defined as the lowest level at which the lapse rate decreases to 2 K km^{-1} or less, and the average lapse rate from this level to any level within the next higher 2 km does not exceed 2 K km^{-1} (Krishna Murthy et al. 1986).

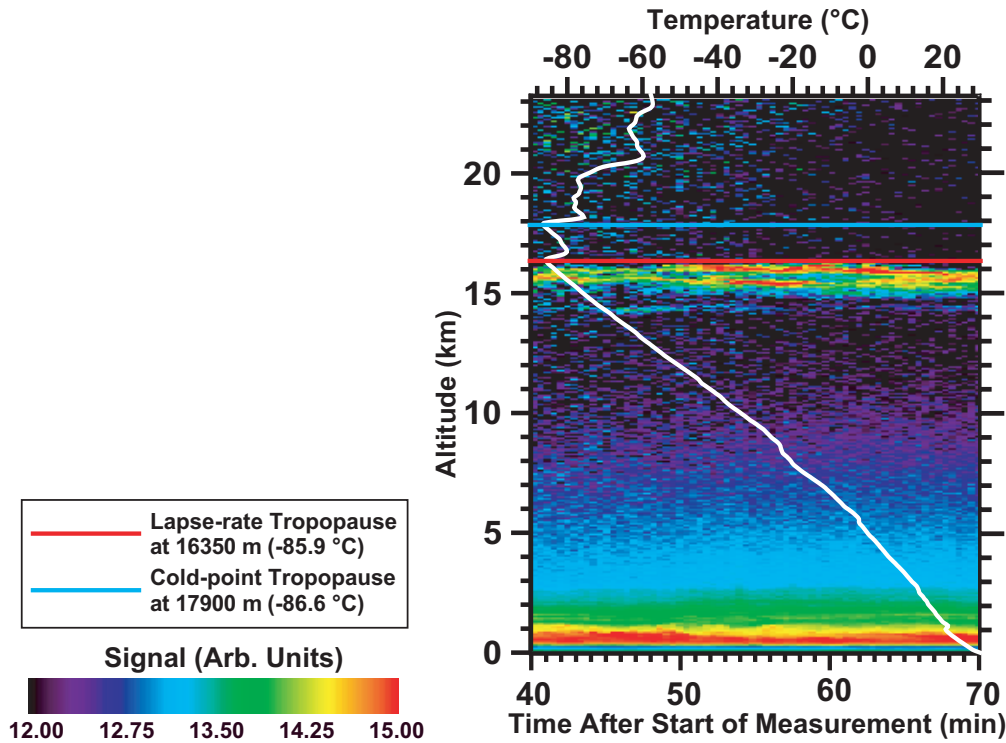


Figure 2.3: Radiosonde temperature profile (white line), lapse-rate tropopause (red line), minimum temperature (blue line), and time-resolved vertical profile of the lidar signal on 16 March 1999. The radiosonde was launched at 12:33 UTC, and the lidar measurement started at 12:22 UTC.

question defined above. The aerosol optical depth (AOD) presented in this study has been derived at the wavelength $\lambda = 630$ nm.

Polar-orbiting satellites are only capable of probing narrow swathes of the atmosphere during each rotation around the earth. It takes about one week to cover the whole surface of the earth because clouds frequently screen the surface and thus the lower-tropospheric aerosol layers. This is the reason for why information on aerosol optical depth is available on a weekly basis only [see Fig. 2.4 (a)]. Despite this fact, the aerosol-optical-depth information still sufficiently fulfills the need of giving an overview on the large-scale distribution and transport of aerosols.

Another data product delivered by the AVHRR aboard the NOAA satellites is the outgoing longwave radiation (OLR) at the top of the atmosphere calculated by the Climate Diagnostic Center (CDC), a division of NOAA (Liebmann and Smith 1996). OLR provides information on the temperature of the body, e.g., a cloud, that emits the radiation. Corresponding to Stefan's law $P = \sigma T^4$, with $\sigma = 5.6697 \times$

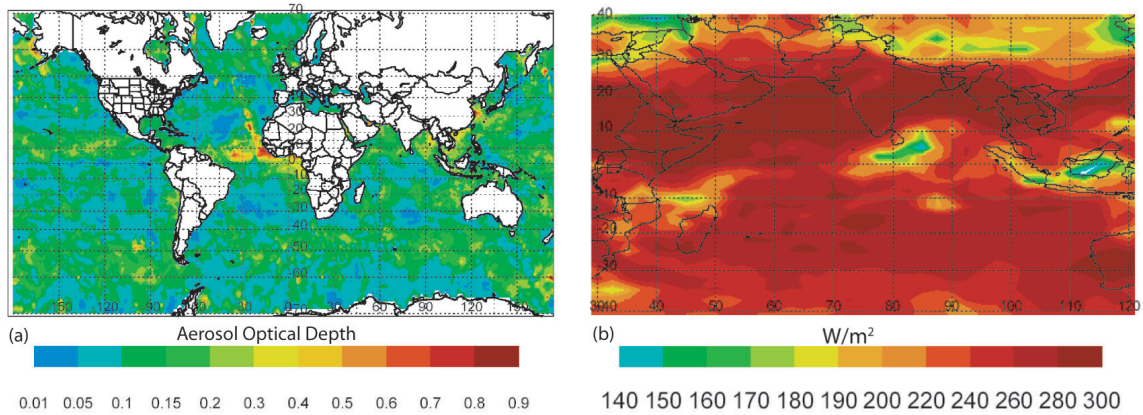


Figure 2.4: (a) AVHRR weekly aerosol optical depth from 15 to 22 Feb 1999, (b) CDC outgoing longwave radiation on 22 Feb 1999.

$10^{-8} \text{ Js}^{-1}\text{m}^{-2}\text{K}^{-4}$ being the Stefan-Boltzmann constant, the power P emitted by a radiant strongly depends on the radiant's temperature T . Therefore, OLR emitted by high, cold, deep convective clouds is much lower than the OLR emitted by warmer low clouds or the ground. Usually, values of less than 170 W m^{-2} indicate deep convection. Deep convection, in turn, indicates regions with extensive lifting of air that might play a role as source regions for cirrus clouds polluted by lower-tropospheric aerosol particles. Interpolated OLR datasets are available on a daily basis [see Figure 2.4 (b)].

2.5 Trajectories

In order to determine the source region of air masses that have been probed by the lidar, 10-day backward trajectories calculated by the Royal Netherlands Meteorological Institute (KNMI) are applied. The model calculations are based on three-dimensional wind and temperature fields obtained from the T213 forecast model of the European Centre for Medium-Range Weather Forecast (ECMWF). Further information can be found in Scheele et al. (1996).

The trajectories have a horizontal resolution of $1^\circ \times 1^\circ$ and a vertical resolution of 10 hPa. They are calculated for each six hours timespan and each 10 hPa span between 1000 and 100 hPa. According to the 1976 standard atmosphere the 100-hPa level corresponds to 16200-m height, what approximately corresponds to the highest cirrus clouds observed during INDOEX.

In this work, the trajectories are used for the determination of the source regions of air parcels in altitudes in which the lidar detected cirrus clouds. This was done in order

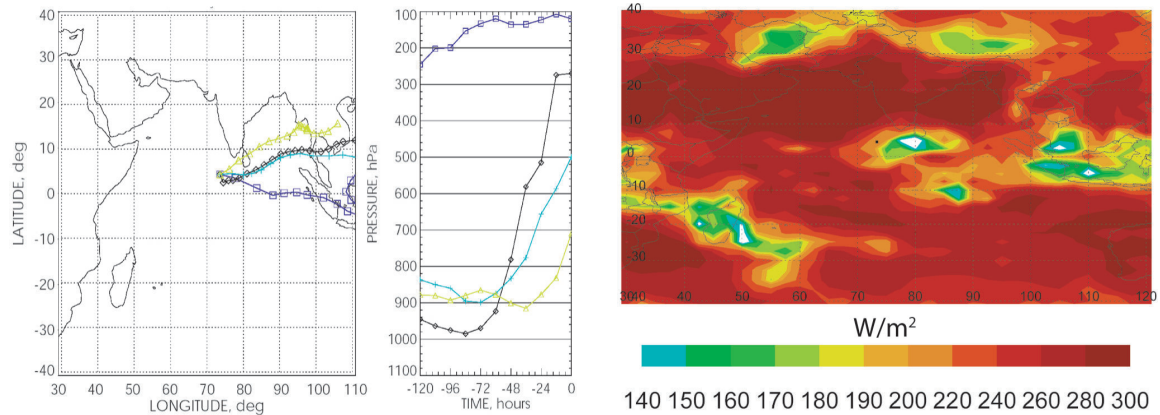


Figure 2.5: KNMI backward trajectories ending on 2 March 1999, 15:00 UTC at Hulule and OLR on 28 Feb 1999 showing a region of deep convection southeast of India that is responsible for the lifting of the trajectories.

to investigate whether the cirrus clouds might have been influenced by anthropogenic aerosol particles from the lower troposphere. Errors are expected to be quite large for such a purpose, since usually small-scale convective processes are responsible for the lifting of air and thus for the vertical transport of particles. But these convective processes are still only rudimentarily implemented in global weather models. However, comparisons of sections in trajectories which indicate lifting with the corresponding OLR data (see Sec. 2.4) are in good agreement, as shown in Fig. 2.5.

Chapter 3

Lidar Data Analysis

3.1 Lidar Principle

A lidar is an active remote-sensing instrument that uses the effects of atmospheric scattering and absorption to gather information about the state and the composition of the atmosphere with high temporal and vertical resolution. In principle, a lidar system consists of two parts, a transmitter and a receiver. The simplest transmitting unit is a laser that emits pulses of monochromatic and almost coherent light which then interacts with the atmospheric constituents. The receiving unit consists of a telescope which collects the returned light and a detector which counts the received photons. With the constant speed of light c the distance R between the telescope and the altitude where the scattering event occurred can be calculated from the time t between emission of the laser pulse and detection of the backscattered light by $R = \frac{1}{2}ct$. If the lidar features a scanning unit, the range R has to be converted to the actual altitude H by $H = R \cos \phi$, with ϕ being the zenith angle (between the zenith and the measurement direction).

The received power is described by the lidar equation. For elastically scattered light of the wavelength λ the lidar equation can be written as:

$$P(R, \lambda) = P_0 \underbrace{\frac{O(R)}{R^2}}_I \underbrace{E(\lambda)}_{II} \underbrace{\beta(R, \lambda)}_{III} \underbrace{\exp \left[-2 \int_0^R \alpha(r, \lambda) dr \right]}_{IV}. \quad (3.1)$$

According to Eq. (3.1) the power of the backscattered signal P received at a specific wavelength λ from a distance R depends on four terms which modify the power P_0 of the emitted laser pulse (Wandinger 2005).

Term (I) contains the range-dependent parameters of the lidar system. $O(R)$ de-

describes the overlap between the field of view of the receiver and the laser beam. In close distance to the lidar the overlap and thus the received signal is zero. The distance needed to achieve a complete overlap depends on the lidar system and can vary between a few meters and several kilometers. The factor R^{-2} describes the quadratic decrease of the received signal with increasing R .

The parameter $E(\lambda)$ of Term (II) represents the system efficiency. It contains all information about the performance of the individual system components, e.g., size of the telescope area, transmission of optical elements, efficiency of detectors as well as the length of the emitted laser pulse.

Term (III) describes the backscatter coefficient $\beta(R, \lambda)$ which is the scattering coefficient for a scattering angle $\Theta = 180^\circ$. It has the dimension of $\text{m}^{-1}\text{sr}^{-1}$.

Term (IV) can be referred to as the transmission term. It considers the fraction of the emitted light that is extinguished because of scattering and absorption on its way from the lidar to the scattering volume in the distance R and back. According to the Lambert–Beer–Bouguer law the transmission term describes the exponential attenuation of light by atmospheric compounds along the line of sight. The volume extinction coefficient α is given in m^{-1} . The factor 2 takes into account that the light has to pass the column of air twice until it reaches the detector of the lidar.

In the atmosphere air molecules (index m) and particles (index p) contribute to the backscatter and extinction coefficients. Therefore, $\beta(R)$ and $\alpha(R)$ can be written as:

$$\beta(R) = \beta_{\text{m}}(R) + \beta_{\text{p}}(R) \quad (3.2)$$

$$\alpha(R) = \alpha_{\text{m}}(R) + \alpha_{\text{p}}(R). \quad (3.3)$$

The molecular backscatter and extinction coefficients β_{m} and α_{m} , respectively, can be calculated by applying the Rayleigh scattering theory for a given number concentration of the air molecules and an effective scattering cross section. Air density can be calculated from temperature and pressure information that is provided by radio soundings or estimated from standard atmospheric conditions. Molecular absorption can be neglected for the wavelengths emitted by the lidar so that only volume scattering has to be taken into account as a contributor to the extinction coefficient.

3.2 Determination of Cloud Base and Top Height

The determination of the lower and upper boundaries of a cloud turns out to be a crucial task. Turbulences and inhomogeneous stratification of the atmosphere often

make it difficult to describe a cirrus cloud as a layer with a constant top and base height.

The determination of the cirrus geometrical properties first might pose the question how the cirrus itself is defined. Water droplets can exist down to temperatures of -37.5 to -40 °C (Heymsfield and Sabin 1989; Rosenfeld and Woodley 2000). Below this temperature only cirrus clouds can form, but at warmer conditions liquid-water and mixed-phase clouds like altocumulus can still occur. According to radiosondes launched at the Maldives (see Section 2.3) the temperature of -37 °C corresponds to altitudes between about 9000 m during the SW monsoon and 10500 m during the NE monsoon season. However, cirrus clouds were also detected at lower altitudes. Between 6000 and 10000 m a transition region was present where both water and ice clouds occurred. Most water clouds can easily be detected because they attenuate the lidar signal much stronger than cirrus clouds [see Fig. 3.1 (c)]. In addition, cirrus clouds below 10000 m usually descended from higher altitudes [see Fig. 3.4 (b)]. The cirrus cloud statistics presented later in this study contain 44 clouds with a base below 10000 m of which only two clouds had their base and top heights below 10000 m. All other clouds extended to altitudes of more than 10000 m and were therefore definitely considered as cirrus clouds.

When, as for this study, lidar data are available, the edges of the clouds can be derived from the received range-corrected signal PR^2 . After eliminating the quadratic dependence between the signal strength P and the distance R in the lidar equation (3.1), significant changes in the signal can only be caused by an increase of the backscatter or extinction coefficient. This is only the case when aerosol or cloud layers are present in the atmosphere. Cirrus clouds produce lidar return signals that are up to 10^2 times stronger than signals that are backscattered from clean regions of the atmosphere. The strong increase of the signal at the cloud base and the decrease at the cloud top indicate the edges of the cirrus clouds.

The steps that are needed to derive the geometrical cirrus properties are illustrated in Fig. 3.1 (a)–(c) and can be described as follows:

1. Create a height-time display (color plot) of the recorded range-corrected signal at $\lambda = 532$ nm for each lidar measurement.
 2. Determine the time periods during which a cirrus layer was present.
 3. Average the range-corrected signal over the respective time period. Altitudes with a strong increase and decrease of the averaged range-corrected signal are finally taken as cloud base height H_b and cloud top height H_t .
-

As obvious in Figure 3.1 the edges of the cirrus clouds are well defined in the colored plots and the mean signal profiles. Note that the determined values of H_b and H_t are the extreme values for a given time period and not the mean values of H_b and H_t for this interval. Thus a representative parameter to describe the height of a cirrus layer is the mid-cloud (center) height H_c , defined as:

$$H_c = \frac{H_t - H_b}{2}. \quad (3.4)$$

Figure 3.1 (a) shows the simplest case of a laminar, subvisible cirrus cloud and (b) shows a developing cirrus with a descending cloud base. The impact of a water cloud (strong attenuation at about 9-km height before minute 15) on the cirrus height determination is presented in Fig. 3.1 (c).

3.3 Determination of Cirrus Cloud Optical Properties

The backscatter and extinction coefficients $\beta_p(R)$ and $\alpha_p(R)$ [see Eqs. (3.2) and (3.3)] in the lidar equation (3.1) can be used to quantify the optical properties of cirrus clouds. Depending on the lidar system used and the ambient measurement conditions different methods are available to derive these values.

In the case of a standard elastic-backscatter lidar, both coefficients $\beta_p(R)$ and $\alpha_p(R)$ have to be determined from one signal. To solve this problem, a relation between $\beta_p(R)$ and $\alpha_p(R)$ has to be assumed. The technique which describes the retrieval of both values from only one available lidar signal is referred to as the Klett method (Klett 1981; Fernald 1984). The procedure is explained in Sec. 3.3.1.

In the case of a combined Raman elastic-backscatter lidar an elastically backscattered signal as well as an inelastically backscattered Raman signal is measured. Now the two parameters $\beta_p(R)$ and $\alpha_p(R)$ can be unambiguously determined from the two measured signals (Ansmann et al. 1992a, see Sec. 3.3.2). This method is known as Raman method. In fact, due to the R^{-2} dependence of the signal even at night only relatively homogeneous cirrus clouds with relatively high optical depths and a minimum occurrence of about 60 minutes are suitable for the Raman method. Therefore, the Raman method was only used to check the results of the Klett procedure under the mentioned favorable conditions. The Klett method, in turn, is applicable up to altitudes of 16000 to 18000 m even for thin, subvisible cirrus clouds that appeared only for a relatively short time. It was therefore applied to all cirrus cases.

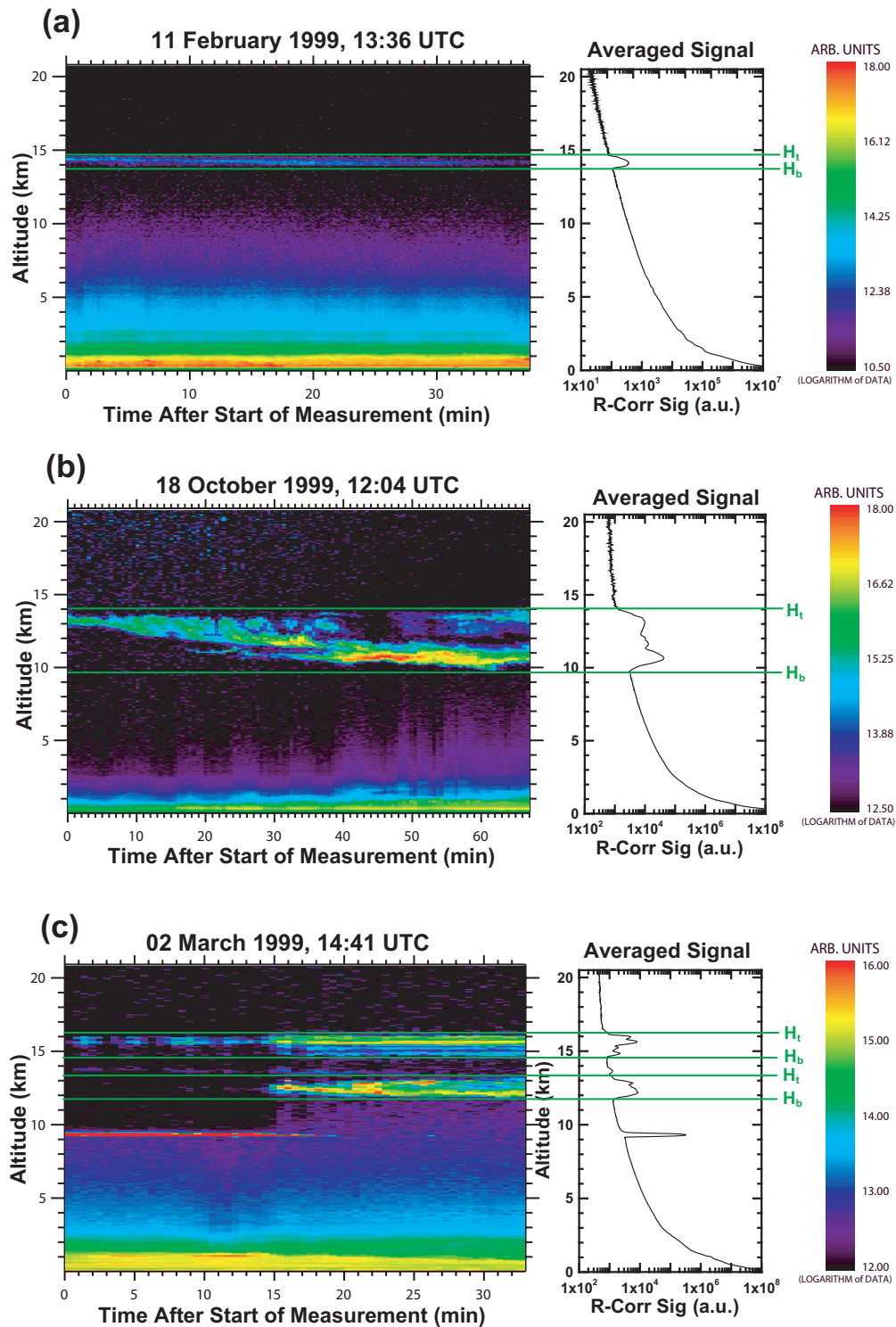


Figure 3.1: Three cases of cirrus observations during INDOEX. Time-resolved and averaged range-corrected signals at 532 nm are shown. Green lines indicate the determined cloud boundaries.

3.3.1 Klett Method

For laser light of a single wavelength and the simplifying assumptions of $E = 1$ and $O(R) = 1$, both values are either known or vanish in the following derivations, Eq. (3.1) becomes:

$$P(R, \lambda) = \frac{P_0}{R^2} \beta(R) \exp \left[-2 \int_0^R \alpha(r) dr \right]. \quad (3.5)$$

With $\alpha_p(R)$ and $\beta_p(R)$ two variables remain unknown in the lidar equation. They can only be derived if a constant relationship between both values is assumed. This relationship is referred to as the particle extinction-to-backscatter ratio, or particle lidar ratio, S_p :

$$S_p = \frac{\alpha_p(R)}{\beta_p(R)}. \quad (3.6)$$

Applying S_p to Eq. (3.5) the resulting Bernoulli equation can be solved for β_p (Fernald 1984):

$$\beta_p(R) = -\beta_m(R) + \frac{A(R_0, R)}{B(R_0) - 2S_p \int_{R_0}^R A(R_0, r) dr}, \quad (3.7)$$

with

$$A(R_0, x) = P(x)x^2 \exp \left[-2(S_p - S_m) \int_{R_0}^x \beta_m(\xi) d\xi \right] \quad (3.8)$$

and

$$B(R_0) = \frac{P(R_0)R_0^2}{\beta_p(R_0) + \beta_m(R_0)}. \quad (3.9)$$

$S_m = \frac{8\pi}{3}$ sr is the Rayleigh extinction-to-backscatter ratio. According to the definition of the particle lidar ratio, the particle extinction coefficient can be obtained from

$$\alpha_p = S_p \beta_p. \quad (3.10)$$

In order to solve Eq. (3.7) the parameter β_p in Eq. (3.9) has to be estimated for a specific reference height R_0 . In the case of cirrus clouds this can be done below and above the cloud without causing large errors, because usually the air is very clean in the upper troposphere. Below and above cirrus clouds one can therefore assume that $\beta_p(R_0) \ll \beta_m(R_0)$ for wavelengths $\lambda \leq 532$ nm (Ansmann 2002).

The formalism used to derive the information about the cirrus mean particle extinction coefficient and optical depth is illustrated in Fig. 3.2 and can be described as follows:

1. First, a cirrus cloud or at least a part of the cloud field, as shown in Fig. 3.2(1), with a relatively constant base, top, and signal has to be found. Averaging over the respective time period and vertical smoothing of the profile helps to minimize signal noise and thus the statistical error. Usually, the window smoothing length is 120 m for the Klett method.
2. Now the Klett algorithm [Eq. (3.7)] is applied to the averaged signal. In order to obtain the vertical profile of the particle backscatter coefficient β_p the missing parameter S_p has to be estimated and the reference height R_0 has to be selected in such a way that $\beta_p(R_0) \approx 0$. Starting with the so-called forward integration (R_0 below the cloud) the particle lidar ratio S_p has to be adjusted in such a way that $\beta_p \approx 0$ above the cloud, assuming that particle backscattering above the cloud is negligible. Next, the backward integration mode (R_0 above the cloud) is applied, and S_p is varied until $\beta_p(R_0) \approx 0$ below the cloud is fulfilled. Finally, the best solutions obtained with the backward and the forward integration are compared. They should give the same S_p value.

The effect of the variation of S_p is demonstrated in Fig. 3.2(2) and 3.2(3). Here it is shown that a lidar ratio of 15 sr (blue curve) underestimates the backscatter coefficient whereas a lidar ratio of 25 sr (red curve) overestimates it. The black curve for $S_p = 20$ sr fits best.

3. For a given vertical profile of β_p the profile of the particle extinction coefficient α_p can be obtained by using Eq. (3.10). Also, the geometrical depth of the cirrus cloud $d_c = H_t - H_b$ can be determined as shown in Fig. 3.2(3). With this information the cloud optical depth

$$\tau = \int_{H_b}^{H_t} \alpha_p(r) dr \quad (3.11)$$

and the mean cloud extinction coefficient

$$\bar{\alpha}_p = \frac{\tau}{d_c} \quad (3.12)$$

can be calculated.

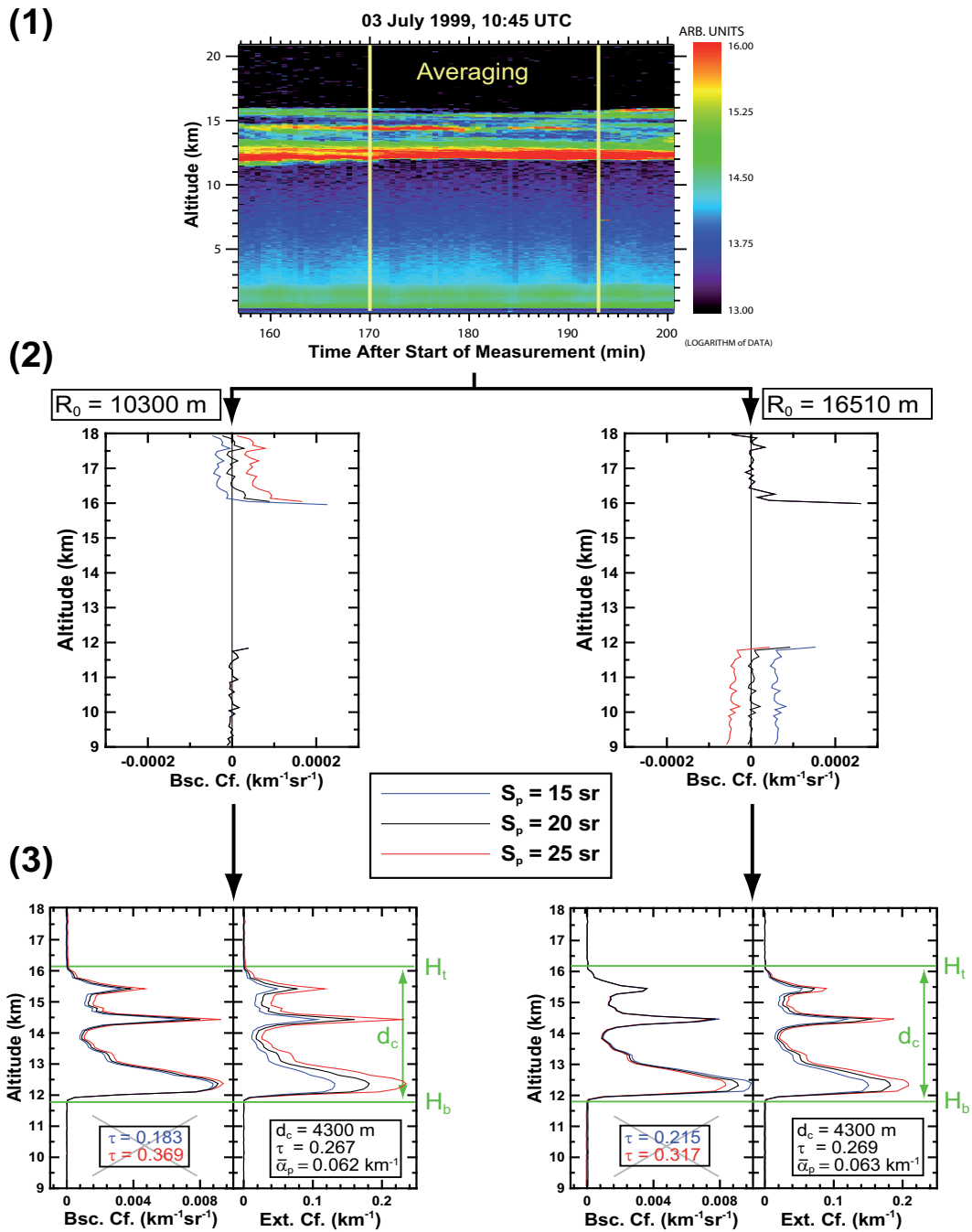


Figure 3.2: Klett method to determine cirrus cloud optical properties. (1) Signal averaging. (2) Determination of reference height R_0 and lidar ratio S_p . (3) Calculation of extinction coefficient α_p , cirrus mean extinction coefficient $\bar{\alpha}_p$, and cirrus optical depth τ . For further information see text.

A consequence of the assumption of a vertically constant lidar ratio for the whole cirrus cloud is that it is not possible to determine the actual vertical profile of the extinction coefficient. Since particle properties, especially size and shape characteristics, change within the cloud, the extinction-to-backscatter ratio changes as well, so that extinction and backscatter profiles deviate from each other. However, as demonstrated above, the Klett method allows us to accurately retrieve the mean cirrus extinction coefficient and the cirrus optical depth (Ansmann 2002).

3.3.2 Raman Lidar Method

As mentioned the Raman lidar method was used to sporadically check the Klett solutions. Before such a comparison of Klett and Raman lidar solutions is shown, the Raman lidar method is briefly explained. No assumption of the lidar ratio is necessary when the molecular backscatter signal is available in addition to the elastic (aerosol) backscatter signal. For that case the lidar equation has the form:

$$P(R, \lambda_{\text{Ra}}) = \frac{P_0}{R^2} \beta_{\text{Ra}}(R, \lambda_0) \exp \left\{ -2 \int_0^R [\alpha(r, \lambda_0) + \alpha(r, \lambda_{\text{Ra}})] dr \right\}. \quad (3.13)$$

Equation (3.13) describes the signal P of the Raman-shifted wavelength λ_{Ra} received from the distance R . The INDOEX lidar that provided the dataset for this study detected the nitrogen Raman signals at wavelengths of 387 and 607 nm, with 355 and 532 nm as primary emitted wavelengths, respectively.

The cirrus particle extinction coefficient can directly be determined from the Raman lidar signal profile $P(R, \lambda_{\text{Ra}})$:

$$\alpha_p(R, \lambda_0) = \frac{1}{2} \frac{d}{dR} \ln \frac{N_{\text{Ra}}(R)}{P(R, \lambda_{\text{Ra}}) R^2} - \alpha_m(R, \lambda_0) - \alpha_m(R, \lambda_{\text{Ra}}). \quad (3.14)$$

Equation (3.14) is valid for wavelength-independent extinction, as it is the case for cirrus in the visible wavelength range. N_{Ra} is the number concentration of the Raman-scattering molecules. The values of N_{Ra} and α_m can easily be estimated from the radiosonde temperature and pressure data.

The particle backscatter coefficient $\beta_p(R)$ at the emitted wavelength λ_0 can be obtained from the ratio of the received elastically backscattered signal $P(R, \lambda_0)$ and the Raman signal $P(R, \lambda_{\text{Ra}})$:

$$\begin{aligned}
\beta_p(R, \lambda_0) = & -\beta_m(R, \lambda_0) + [\beta_p(R_0, \lambda_0) + \beta_m(R_0, \lambda_0)] \\
& \times \frac{P(R_0, \lambda_{Ra})P(R, \lambda_0)N_{Ra}(R)}{P(R_0, \lambda_0)P(R, \lambda_{Ra})N_{Ra}(R_0)} \\
& \times \frac{\exp\left\{-\int_{R_0}^R [\alpha_p(r, \lambda_{Ra}) + \alpha_m(r, \lambda_{Ra})] dr\right\}}{\exp\left\{-\int_{R_0}^R [\alpha_p(r, \lambda_0) + \alpha_m(r, \lambda_0)] dr\right\}}.
\end{aligned} \tag{3.15}$$

As for the Klett method a reference value $\beta_p(R_0, \lambda_0)$ is needed in order to solve Eq. (3.15). The reference height R_0 is again set in a region with clear air.

A comparison of the Klett and the Raman method is presented in Fig. 3.3. As illustrated in the left of the four diagrams of the figure the best Klett solution is obtained with a lidar ratio of 18 sr (black curve). This value is also in good agreement with the backscatter coefficient obtained with the Raman method (red curve). A lidar ratio of 25 sr (blue curve) seems to overestimate the backscatter coefficient. This is confirmed by the comparison of the respective extinction coefficients. The profiles of the extinction coefficient and the lidar ratio obtained with the Raman method had to be smoothed over 1800 m in order to reduce the influence of signal noise. The Raman extinction-coefficient profile lies within the error range of 20% of the Klett solution for $S_p = 18$ sr. The Raman method itself has an error of about 25%. The cirrus mean lidar ratio obtained with the Raman method is 20 sr (± 10 sr standard deviation) for the 11.5–16.5-km height range. The standard deviation includes statistical uncertainties but also changes of the lidar ratio with height due to changes in the ice-crystal characteristics.

3.4 Error Discussion

In the following paragraphs only the errors arising from using the Klett method are discussed. Because the Klett method was used to establish the cirrus statistics, uncertainties of the Raman method are not subject of this section. Extensive error analyses, especially for the Raman lidar method, can be found in Ansmann et al. (1992b), Mattis (1996), and Mattis (2002).

3.4.1 Reference-Value Estimate

The first assumption that has to be made in order to calculate the backscatter coefficient with the Klett method concerns the reference value of the particle backscatter coefficient at a specific altitude. As already described in Sec. 3.3.1 the particle backscatter

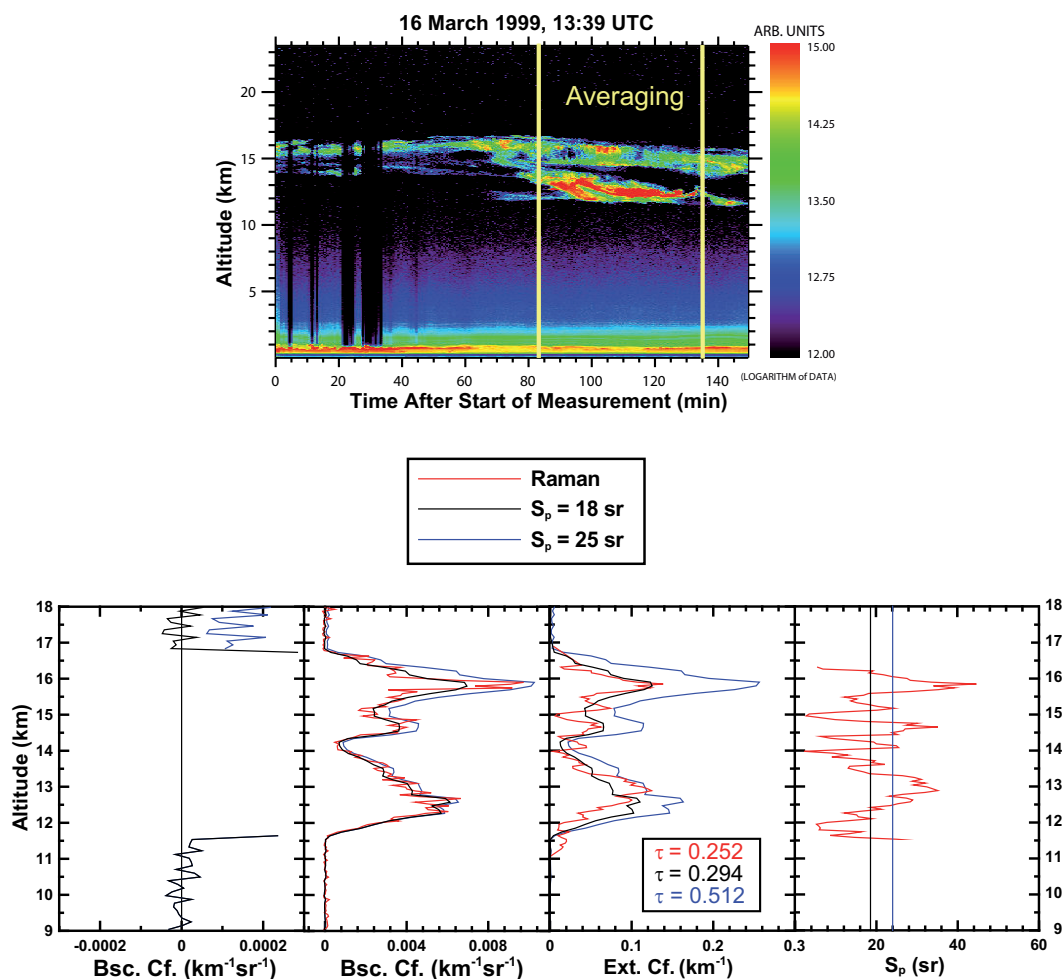


Figure 3.3: Comparison of the Klett and the Raman method at 532 nm for a cirrus cloud case on 16 March 1999. Window smoothing length for the Klett solutions and the Raman backscatter coefficient (Bsc. Cf.) is 120 m. For the Raman solution of the extinction coefficient (Ext. Cf.) and the lidar ratio (S_p) the window smoothing length is 1800 m. Vertical lines in the S_p plot indicate the assumed Klett lidar ratios of 18 and 25 sr. The layer mean lidar ratio derived by applying the Raman lidar method was about 20 sr.

coefficient was set to zero in the regions below and above the cirrus clouds. The impact of aerosol particles is assumed to be negligible in these regions of the atmosphere. For lidar data analysis in the lower troposphere Franke et al. (2003) assumed a reference value of $\beta_p(R_0) = 3 \times 10^{-4} \text{ km}^{-1}\text{sr}^{-1}$ at an altitude of $R_0 = 6000 \text{ m}$. Usually, R_0 was located above 10000 m for the cirrus analysis. If, however, particles had caused a $\beta_p(R_0) = 3 \times 10^{-4} \text{ km}^{-1}\text{sr}^{-1}$ in this height region as well, the error of the extinction coefficient would have been $3 \times 10^{-4} \text{ km}^{-1}\text{sr}^{-1} \times 20 \text{ sr} = 0.006 \text{ km}^{-1}$ [see Eq. (3.10)], assuming a lidar ratio of 20 sr. For a cirrus layer with a geometrical depth of 1 km the error in the derived optical depth would be less than 0.01. Thus the relative error on the particle extinction coefficient due to an incorrect reference value is less than 5% for most cirrus clouds. Only for optically thin and subvisible cirrus clouds this error has to be taken into account.

3.4.2 Lidar-Ratio Estimate

In order to discuss the uncertainties caused by the assumption of the particle lidar ratio S_p three different types of cirrus clouds, classified by their optical depths, have to be taken into account. An accurate determination of S_p with a relative error of $\pm 20\%$ with the Klett method is only possible for clouds with an optical depth between about 0.06 and 0.6. 62% of all analyzed cases fulfilled this criterion.

26% of all analyzed cirrus cases were clouds with an optical depth $\tau \leq 0.06$. In such cases the problem occurred that the Klett solution for the backscatter coefficient is almost invariant to changes of the lidar ratio. The extinction of light is too small to sensitively influence the backscatter retrieval. In other words, all reasonable lidar ratios lead to almost the same result. The only way to include these thin clouds in the cirrus cloud statistics was to assume a specific lidar ratio. Thus a lidar ratio of 20 sr, obtained as the mean value of all cirrus cases that were analyzed, was applied to these invariant cirrus cases. The value of 20 sr is in good agreement with theoretical studies of Sassen and Cho (1992), who also reported lidar ratios around 20 sr for thin (subvisible) cirrus. Sunilkumar and Parameswaran (2005) applied a lidar ratio of 20 sr to all analyzed cirrus clouds.

An example for a very thin cirrus cloud is given in Fig. 3.4 (a). The cloud extended from 15 to 17 km. The reference value was set to $\beta_p(R_0) = 0 \text{ km}^{-1}\text{sr}^{-1}$ below the cloud base. The left of the three graphs below the time-resolved signal profile demonstrates the invariability of the backscatter coefficient to changes of the lidar ratio. Hence, it is not possible to determine a correct value for the lidar ratio making it necessary to assume the value of 20 sr (blue curve). Additional uncertainties when analyzing

optically thin cirrus clouds are caused by low signal-to-noise ratios. This is also the case in Fig. 3.4 (a). The increase of the backscatter coefficient caused by the cirrus layer is small in comparison to the ambient signal noise. It should be noted that the signal noise for the cirrus case shown in Fig. 3.4 (a) is fairly low, it just appears to be high due to the weak signal caused by the cirrus layer.

Optically thick cirrus clouds with $\tau > 0.6$, representing 12% of the analyzed cases, sometimes completely attenuate the lidar signal, so that no information is available from above the cloud. As a first consequence the cloud top height may be underestimated. When applying the standard Klett method to such thick clouds the backscatter coefficient is often shifted to negative values above the cloud, when the reference value is set below the cloud. Choosing a reference value above the cloud is not possible. In order to add the optically thick clouds to the statistics another approach was applied. For optically thick clouds the solution of the Klett algorithm [see Eq. (3.7)] tends to instability with increasing lidar ratio, i.e., the backscatter and thus the extinction coefficients increase rapidly with height to ambiguous values. This behavior can be used to find the most appropriate lidar ratio (Ansmann et al. 1993). As usual a reference value has to be chosen below the cirrus. The lidar ratio is varied until the backscatter profile shows tendencies to become instable. The value of S_p that is closest to the instable value is taken as the valid lidar ratio and used to calculate the vertical profile of the particle extinction coefficient.

Figure 3.4 (b) shows a cirrus cloud with a high optical depth. As illustrated in the three graphs below the contour plot, slight variations of the lidar ratio cause strong variations of the resulting backscatter and extinction coefficients. Except for the instable solution (green curve) the backscatter coefficient above the cloud is always negative. The best solution for this case can be achieved with a lidar ratio of 19 sr (black curve) since the solution for 20 sr (green curve) is instable.

The relative error of the retrieved particle extinction-coefficient profile resulting from the assumption of the lidar ratio depends on the analyzed cloud type. For clouds with an optical depth between 0.06 and 0.6 the error is less than 25%. Since the values of the particle extinction coefficient are already fairly large for thick clouds, here the relative error is expected to be about 50%. In contrast, the relative error for the very thin clouds can be up to 100%, considering that the actual lidar ratio of these clouds might vary between 1 and 50 sr.

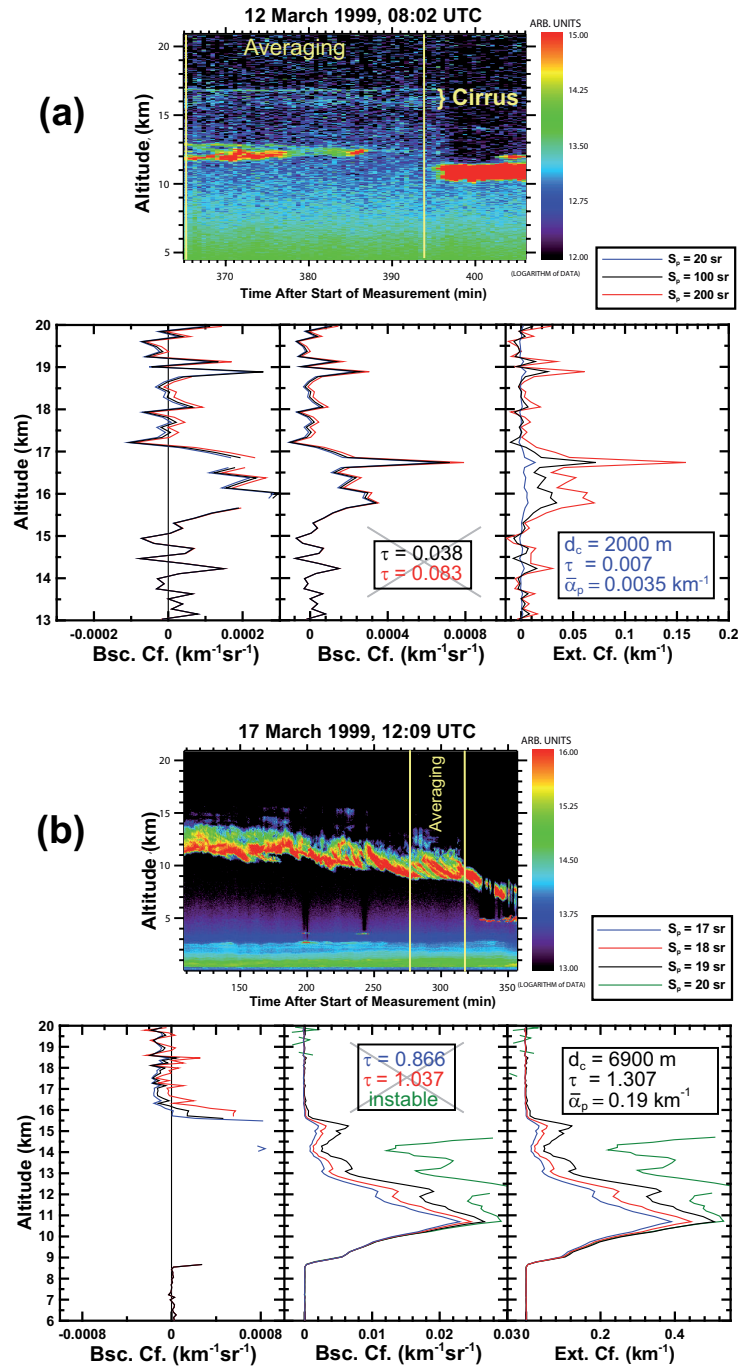


Figure 3.4: Examples for the error of backscatter and extinction coefficients in (a) optically thin and (b) optically thick cirrus clouds. Example (a) shows the invariance of the backscatter coefficient (Bsc. Cf.) with respect to changes of the lidar ratio S_p . Example (b) illustrates the tendency to instability with increasing lidar ratio for optically thick clouds.

3.4.3 Error due to Multiple Scattering

A fundamental assumption of the lidar signal analysis is the single-scattering approximation. According to the lidar equation (Eq. 3.1), photons that are scattered at angles $\neq 180^\circ$ are assumed to be lost for detection. However, due to strong forward scattering by ice crystals, about 50% of the light is scattered at rather small angles and remains in the receiver field of view (RFOV) of the lidar. This is illustrated in Fig. 3.5. As a consequence of multiple scattering, the attenuation of laser light in the ice cloud along the line of sight is much smaller than expected from the single-scattering approximation.

Multiple scattering causes an underestimation of the extinction coefficient and thus of the optical depth. The strength of multiple scattering primarily depends on the cirrus particle properties such as size and shape. But size and shape of the ice particles strongly depend on altitude, temperature, and the formation mechanism. In addition, the actual influence of multiple scattering depends on the observation geometry, i.e., RFOV and distance to the cloud.

The impact of multiple scattering on the determination of cirrus optical properties has been estimated in various previous publications (Sassen and Cho 1992; Platt and Dilly 1981; Platt et al. 1987). Optically thick clouds have been reported to cause higher amounts of multiple scattering than optically thin clouds. On average, the extinction coefficients in cirrus and the optical depths are underestimated by about 20%–30%, if multiple scattering is ignored (Wandinger 1998). But since the actual contribution of multiple scattering depends on multiple conditions, the determined

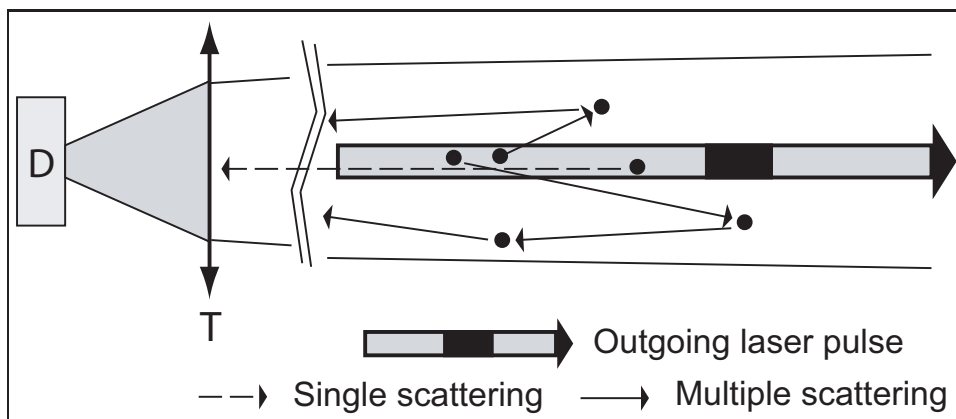


Figure 3.5: Illustration of multiple scattering of laser light. The outer tilted lines indicate the receiver field of view of the telescope (T). D is the detector. Complete overlap of laser beam and RFOV is assumed. Adapted from Bissonnette (2005).

values show substantial variations of 20% to 70% between the different publications (Sunilkumar and Parameswaran 2005). Thus the uncertain impact of multiple scattering on the different cirrus cloud types is not included in the results presented in Chapter 5.

Chapter 4

Tropical Cirrus

The following sections give an introduction to cirrus properties and formation mechanisms with focus on tropical cirrus clouds. The formation mechanisms are compared to findings during INDOEX. Possible effects of aerosol particles on cirrus clouds are discussed and indications for polluted cirrus clouds are examined.

4.1 Basic Cirrus Properties

Independent of the region, cirrus is defined as a high-altitude cloud consisting entirely of ice (WMO 1975). Sassen and Cho (1992) categorized cirrus clouds with respect to their optical properties. They defined three cirrus types — cirrostratus, thin cirrus, and subvisible cirrus. Subvisible cirrus is characterized by an optical depth of $\tau < 0.03$. Thin cirrus is found in the range from $0.03 < \tau < 0.3$, whereas cirrostratus has optical depths of $\tau > 0.3$, with maximum values reaching up to $\tau = 20$. The appearance of these cloud types is obvious from their names. Subvisible cirrus cannot visually be seen from the ground. Thin cirrus appears as bluish or transparent, mostly inhomogeneous cloud. Cirrostratus is opaque and has a layered structure. The categorization after Sassen and Cho (1992) is used in Sec. 5.2, where the optical properties of the INDOEX cirrus dataset are presented.

As briefly mentioned in the introduction to this study, cirrus clouds affect the radiation budget of the atmosphere. The primary problem is to quantify the greenhouse-versus-albedo effect. This is an all-day problem for a forecast meteorologist because cirrus clouds which cover the sky increase the minimum surface temperature at night and decrease the maximum surface temperature that can be reached during the day. Comstock et al. (2002) found that cirrus clouds with optical depths $\tau > 0.06$ significantly affect the OLR at the top of the atmosphere. A cirrus with an optical depth

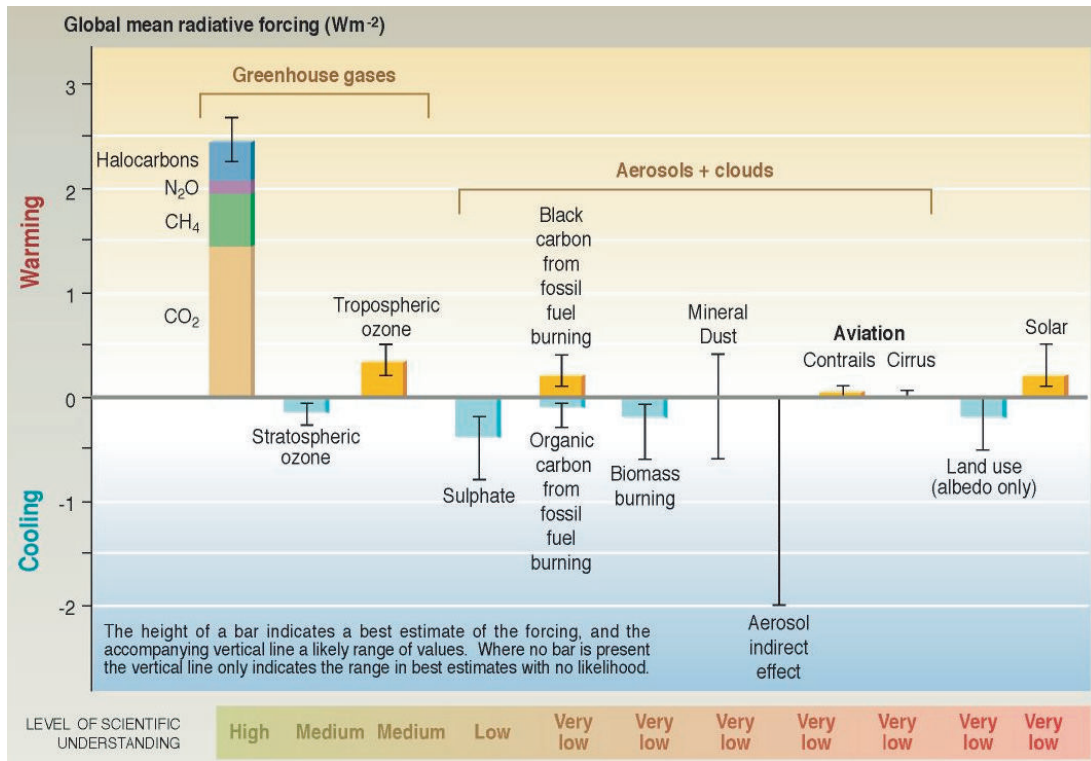


Figure 4.1: Sketch of the impact of anthropogenic climate effects on the radiation budget of the atmosphere (IPCC 2001). Cirrus is only considered in connection with aviation but might contribute to the highly uncertain value of the indirect aerosol effect.

of $\tau = 0.06$ reduces the outgoing longwave radiation by 10 Wm^{-2} . Values of $\tau = 0.8$ reduce the OLR by 80 Wm^{-2} . Radiative forcing of subvisible cirrus is small but not negligible (McFarquhar et al. 2000). Subvisible cirrus clouds can, e.g., bias satellite measurements because they are often not detectable with standard satellite radiometers. Thus subvisible cirrus can cause an error of about 2 K in the retrieval of sea surface temperature with satellites (Lynch and Sassen 2002).

The impact of cirrus in a climate perspective and anthropogenic effects on cirrus have not been exactly quantified yet. As shown in Fig. 4.1 (IPCC 2001) the estimated anthropogenic influence on the direct effect of cirrus is only considered in conjunction with aviation. But since cirrus clouds might also be affected by aerosols (see Sec. 4.3), they could also contribute to the indirect aerosol effect indicated by a huge error bar in Fig. 4.1.

4.2 Cirrus Formation Processes

According to the current understanding the primary formation mechanisms of cirrus in the tropics are (Jensen et al. 1996):

1. blow-off from deep convective systems,
2. large-scale uplift of humid layers,
3. cooling due to wave activity in the upper troposphere.

Convective cumulonimbus clouds are the primary source for blow-off cirrus which forms when upper tropospheric winds blow ice particles away from their anvils. Also the anvil clouds that remain in the troposphere after the deep convective cloud below dissolved are counted as blow-off cirrus. Such cirrus clouds appear as rather opaque, textured clouds with irregular boundaries (see Fig. 4.2). They can persist for 0.5 to 3 days. Their top heights are restricted to the maximum altitude deep convection can reach. Except for a small fraction of less than 1.8%, the upper boundary for deep convection is 14 km (Liu and Zipser 2005). Thus blow-off cirrus usually do not occur at altitudes above 14 km. An example can be seen in Fig. 4.3 (b) below 14 km.

Large-scale dynamic lifting of humid layers supports the formation of cirrus at higher altitudes. The lifting leads to a cooling of the layer until the air is super-saturated with water vapor and ice nucleation occurs. Jensen et al. (1996) named

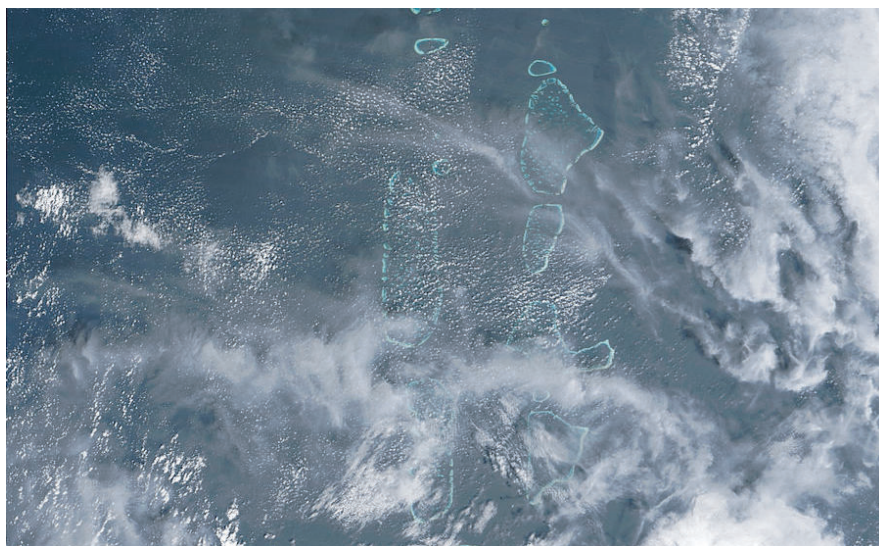


Figure 4.2: Cirrus clouds and lower cumulus clouds covering the sky over the Maldives. Picture taken from <http://modis.gsfc.nasa.gov/>

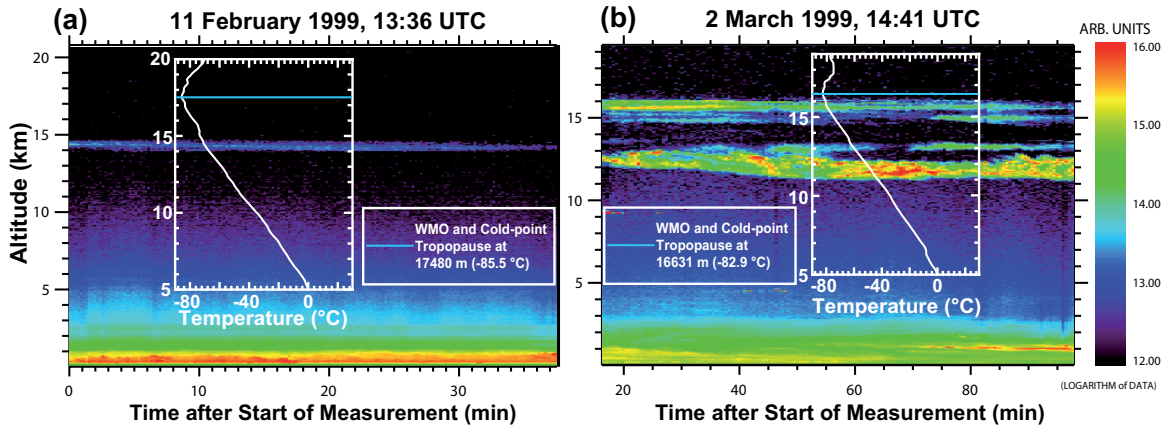


Figure 4.3: Two examples for specific cirrus clouds and corresponding radiosonde data with tropopauses. (a) Cirrus layer which most likely formed in the absence of deep convection. (b) Blow-off cirrus up to 14 km. The cirrus layer at 15 km might be induced by radiative cooling by the former deep convective cloud below it (Hartmann et al. 2001).

different processes that can cause dynamic lifting: flow over continental-scale bulges in the tropopause, flow over large-scale convective systems, and lifting above stratiform regions of mesoscale convective systems. Clouds induced by these processes usually appear as rather tenuous, laminar layers of low optical depth spreading homogeneously over large areas. They have a geometrical depth of about 1 km and are located at altitudes above 14 km, often close to the tropopause or to strong temperature inversions [see Fig. 4.3 (a)].

Deep convective clouds are also capable of causing considerable radiative cooling above their anvils. Hartmann et al. (2001) showed that thin and subvisible cirrus can form above deep convective clouds. These layers are comparable to pileus clouds but more stable. After the deep convective clouds dissolve the ‘trapped’ cirrus remains in the upper troposphere as a layer located above the remnant of the dissipating anvil cloud and the blow-off cirrus [see Fig. 4.3 (b) above 14 km].

Recent studies reveal a strong link between cirrus clouds and atmospheric waves which cause in-situ cooling on a synoptic scale. Massie et al. (2002) reported cirrus cloud fields that show similarities to gravity waves with wavelengths between 500 and 1000 km. Boehm and Verlinde (2000) found a strong correlation between descending stratospheric Kelvin waves and the occurrence of cirrus. According to this study negative temperature deviations from the average temperature in the upper troposphere are directly related to the occurrence of cirrus. The mechanism of the stratospheric Kelvin waves can be found in Holton (1992). The results of Boehm and Verlinde can be

reproduced with the INDOEX radiosonde dataset. Fig. 4.4 shows the radiosonde temperature field and the deviation from the average temperature of all 54 measurement days in spring 1999. The red line in both figures indicates the lapse-rate tropopause (see Sec. 2.3) and the white line the observed minimum temperature, or cold-point tropopause, of each radiosonde ascent. The dashed black line at an altitude of 6 km indicates times during which the lidar was operated. White vertical lines correspond to observed cirrus clouds. The red areas in Fig. 4.4 (b) correspond to a positive deviation of 5 K and the dark areas to a negative deviation of 5 K from the average temperature. Between Julian day 70 and 85 a cold perturbation can be found at an altitude of about 15 km. During this time period the highest frequency of cirrus clouds has been observed. During warmer periods, as between Julian day 64 and 70, almost no cirrus has been detected, despite the high number of lidar observations. The downward propagating Kelvin waves can best be recognized at altitudes above 17 km. They show a wavelength of about 12 days with an amplitude of more than 5 K.

The analysis of the three additional field campaigns in July and October 1999 and in March 2000 shows the same wave characteristics in the lower stratosphere and strong indications for the influence of deep convection on cirrus formation as well. Because of the shorter duration of these campaigns the graphs are less representative and are therefore not shown in this study.

As shown in Fig. 4.5 (c) the occurrence of cirrus is also strongly correlated with the distance to deep convection. Figures 4.5 (a) and (b) present the same temperature and temperature-deviation fields as Fig. 4.4. Tropopauses and lidar measurement times are left out. Only data from Julian day 41 (11 Feb) to 84 (25 March) in 1999 are shown, because lidar data were scarce for the days before. The data for the bar chart in Fig. 4.5 (c) were calculated from the CDC OLR dataset. For each Julian day, the bars show the geographical distance between Hulule, where the lidar was located, and the nearest location with deep convection. It is obvious from the graph that especially between Julian day 70 and 85 there was strong convective activity close to Hulule. On day 75, corresponding to the 16 March 1999, deep convection was observed directly at the lidar site. In the scope of this study a comparison of the cirrus occurrences reported by Boehm and Verlinde (2000) with their distance to deep convection revealed similar correlations as shown in Fig. 4.5.

We may conclude that ice clouds found below approximately 14 km most probably result from the convective activity around Hulule, whereas the occurrence of cirrus with a base above 14 km may be modulated by large-scale processes such as stratospheric-wave and gravity-wave activity.

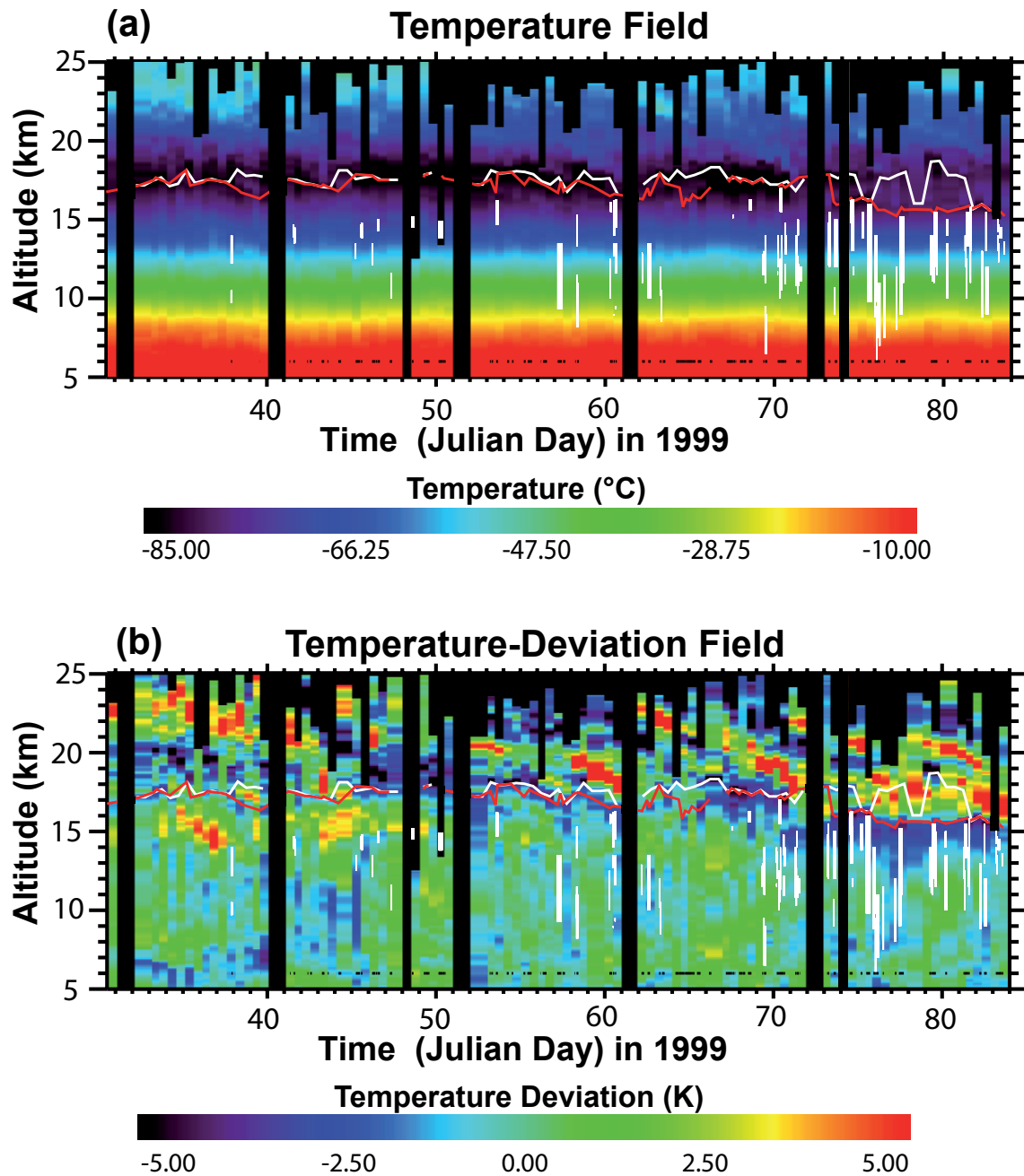


Figure 4.4: (a) Temperature field created from 54 days of radiosonde data in spring 1999. (b) Temperature deviation from the average temperature of all radiosondes for the same time period. Descending stratospheric waves are visible. Red line: WMO tropopause; white line: cold-point tropopause; white vertical lines: observed cirrus; black dashed line at 6 km: periods of lidar operation.

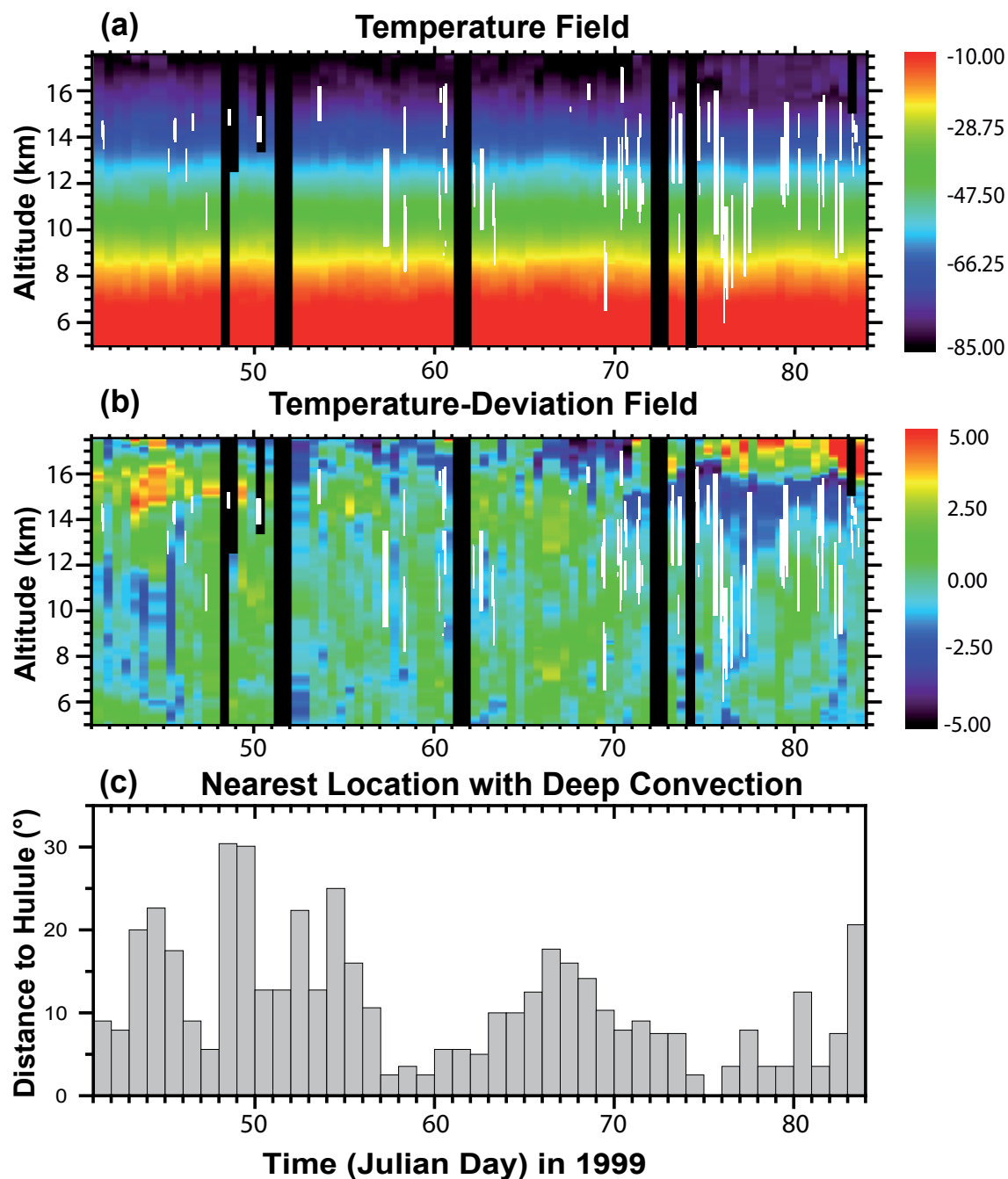


Figure 4.5: (a) and (b) same as Figure 4.4 but without tropopauses and lidar measurement times. (c) Distance between Hulule and nearest location with deep convection ($OLR < 170 \text{ W m}^{-2}$). $1^\circ \approx 110 \text{ km}$. The correlation between distance to deep convection and cirrus occurrences is noteworthy.

4.3 Anthropogenic Pollution and Cirrus

Anthropogenic pollution is supposed to primarily affect cirrus in an indirect way. The most prominent example of anthropogenically influenced cirrus is cirrus induced by contrails. The impact of contrail cirrus on the global climate is not yet completely quantified but has already been discussed in numerous publications (Sassen 1997; Minnis et al. 2002; Marquart et al. 2003). The IPCC 2001 report specified a positive climate forcing of 0.1 to 0.3 W m⁻² for aviation-induced cirrus (see Fig. 4.1).

Contrail cirrus and its formation is not subject of this study, because these clouds primarily affect climate and radiative processes in the mid-latitudes where aviation traffic is much stronger than in the tropics. Thus the approach in the case of the INDOEX region is a different. Here, lower tropospheric aerosol might affect the cirrus properties in an indirect way. First, it has to be distinguished between the northeast and the southwest monsoon. As already mentioned in Sec. 2.1 anthropogenically polluted air from southeast Asia is supposed to advect toward the Maldives during the NE monsoon season only. At this time of the year the ITCZ is located south of the equator and thus south of the Maldives (Ramanathan et al. 2001a). The aerosol layers present over the Maldives at this time of the year extend up to altitudes of 4 km (Franke et al. 2003). Convective clouds which form in such layers might be affected by the enhanced concentration of aerosol particles. These could act as additional cloud condensation nuclei (CCN, Twomey 1974). For a constant liquid-water content, enhanced particle concentrations increase the cloud droplet number concentration. As a consequence, the mean cloud droplet diameter decreases, providing conditions for the first indirect aerosol effect (Ramanathan et al. 2001b). Increasing life time, decreasing precipitation, and increasing albedo, the so-called Twomey effect, are possible effects on water clouds (Lohmann and Feichter 2005). Heymsfield and McFarquhar (2001) reported droplet number concentrations in maritime convective clouds north of the ITCZ that were up to five times higher than in convective clouds south of the ITCZ. They also reported higher reflectivity (albedo) of these polluted clouds which was further confirmed by satellite measurements (Liu et al. 2003). Thus the Twomey effect on water clouds north of the ITCZ could be verified during INDOEX in spring 1999.

In the case of smaller droplets an important ice production process in tropical clouds, the Hallett–Mossop process (Hallett and Mossop 1974; Mossop and Hallett 1974; Pruppacher and Klett 1997), might be suppressed (Rosenfeld 2000). The Hallett–Mossop process describes the important role ice particle splintering plays during the riming process in clouds. The resulting ice splinters act again as ice nuclei,

supporting the Bergeron–Findeisen ice production process. In order to be effective the Hallett–Mossop process requires relatively high number concentrations of large droplets. Since droplets are comparably small in polluted clouds ice production at relatively high temperatures might be less effective than it would be in clean maritime clouds. Hence, more droplets would be lifted up to altitudes with temperatures below -37.5 °C. At such temperatures the droplets finally freeze homogeneously. According to this theory, cirrus clouds that are influenced by anthropogenic pollution should have more and smaller ice particles than pristine cirrus clouds (Ramanathan et al. 2001b). This would lead to cirrus clouds with a higher reflectivity. Thus a Twomey effect for ice clouds can be expected.

4.4 Are There Indications for Polluted Cirrus Clouds?

In this section the primary assumption that the Maldives region is affected by pollution during the northeast monsoon season only is checked. Beside the indications for ‘polluted’ water clouds given by Heymsfield and McFarquhar (2001) and Liu et al. (2003), results of Franke (2003) and backward trajectory calculations strengthen the approach described in Sec. 4.3. Franke (2003) reported mean aerosol optical depths between 0.29 and 0.33 over Hulule for the NE monsoon season. During the SW monsoon in July and October 1999 the mean value was only 0.12. Franke (2003) also published trajectory cluster analyses for the NE monsoon season. The clusters were calculated for the lower troposphere from the same KNMI dataset as introduced in Sec. 2.5. They confirm the assumption that the source regions of air masses observed at the Maldives during the NE monsoon season are located over southeast Asia and India.

A trajectory case study for a cirrus layer detected on 2 March 1999 is presented in Fig. 4.6. The backward trajectories define southeast Asia as the source region of the air parcels arriving at 200, 350, 500, and 700 hPa over Hulule. The trajectories [see Fig. 4.6 (b)] crossed the Gulf of Bengal until strong lifting occurred at about -48 hours. The CDC OLR data [see Fig. 4.6 (c)] confirm the existence of a deep convective system east of the Maldives. This system seems to be responsible for the lifting shown in the trajectories. High values of aerosol optical depth (AOD) of up to 0.4 along the way of the trajectories and of about 0.3 in the Maldives region are indicated in Fig. 4.6 (d). Of specific interest is the lifting of air masses from below 500 hPa to pressure levels between 300 and 150 hPa which roughly correspond to altitudes between 9.5 and

14 km. As described in Sec. 4.2 cirrus induced by deep convection is generally located below altitudes of 14 km. Thus cirrus clouds located at higher altitudes should not be affected by the indirect aerosol effect described in Sec. 4.3.

It should be noted that no cluster analysis of backward trajectories was performed in order to check the source regions of upper tropospheric air masses. Instead, trajectories were calculated only for specific cirrus cases. This was done in order to validate the primary assumption that the source regions of the air masses differ between NE and SW monsoon. In general, the trajectories confirm that there are different air masses involved in the cirrus formation process during the two monsoon seasons. At pressure levels below 300 hPa easterly wind regimes dominated during both monsoon seasons. These winds can be explained by the presence of the tropical easterly jet. This jet stream especially dominates the circulation in the northern Indian Ocean region during the SW monsoon (Gosh et al. 2001). The dominating presence of easterly winds yields to the suggestion that cirrus clouds detected over Hulule probably originated east of the Maldives. This is assumed to be the case as long as deep convection was not located right above or close to the Maldives.

During the SW monsoon deep convection was permanently found very close to the Maldives. This is shown in Fig. 4.7 (c) and (d). Figure 4.7 (a) and (b) show the distance to deep convection during the NE monsoon season. On some days in July [Fig. 4.7 (c)] and October 1999 [Fig. 4.7 (d)] deep convection was located directly over the Maldives. This is indicated by a distance of zero degrees (no bars visible) in the graphs. Taking the permanent presence of deep convection at the lidar site into account, one might conclude that most detected cirrus clouds originated from these deep convective systems. This would also be the case during the convectively active periods during the NE monsoon, when most cirrus clouds occurred. One can also assume the AOD values reported by Franke (2003) to be valid in the vicinity of the Maldives. Thus pollution affecting deep convective systems would be restricted to the NE monsoon season, when the AOD at the Maldives was about three times as high as during the SW monsoon.

However, trajectory analyses and AVHRR AOD indicate that pollution could still be involved in cirrus formation during the SW monsoon. Figures 4.8 and 4.9 show two cirrus cases from July and October 1999, respectively. As expected, the source regions of the backward trajectories were primarily located in the open Indian Ocean [Fig. 4.8 (b) and 4.9 (b)]. Easterly winds dominated the circulation in the upper troposphere below the pressure level of 300 hPa. In contrast to Fig. 4.6 deep convection was omnipresent over India and the northern Indian Ocean [Fig. 4.8 (c) and 4.9 (c)]. This finding reflects that the ITCZ was located north of the Maldives at that time.

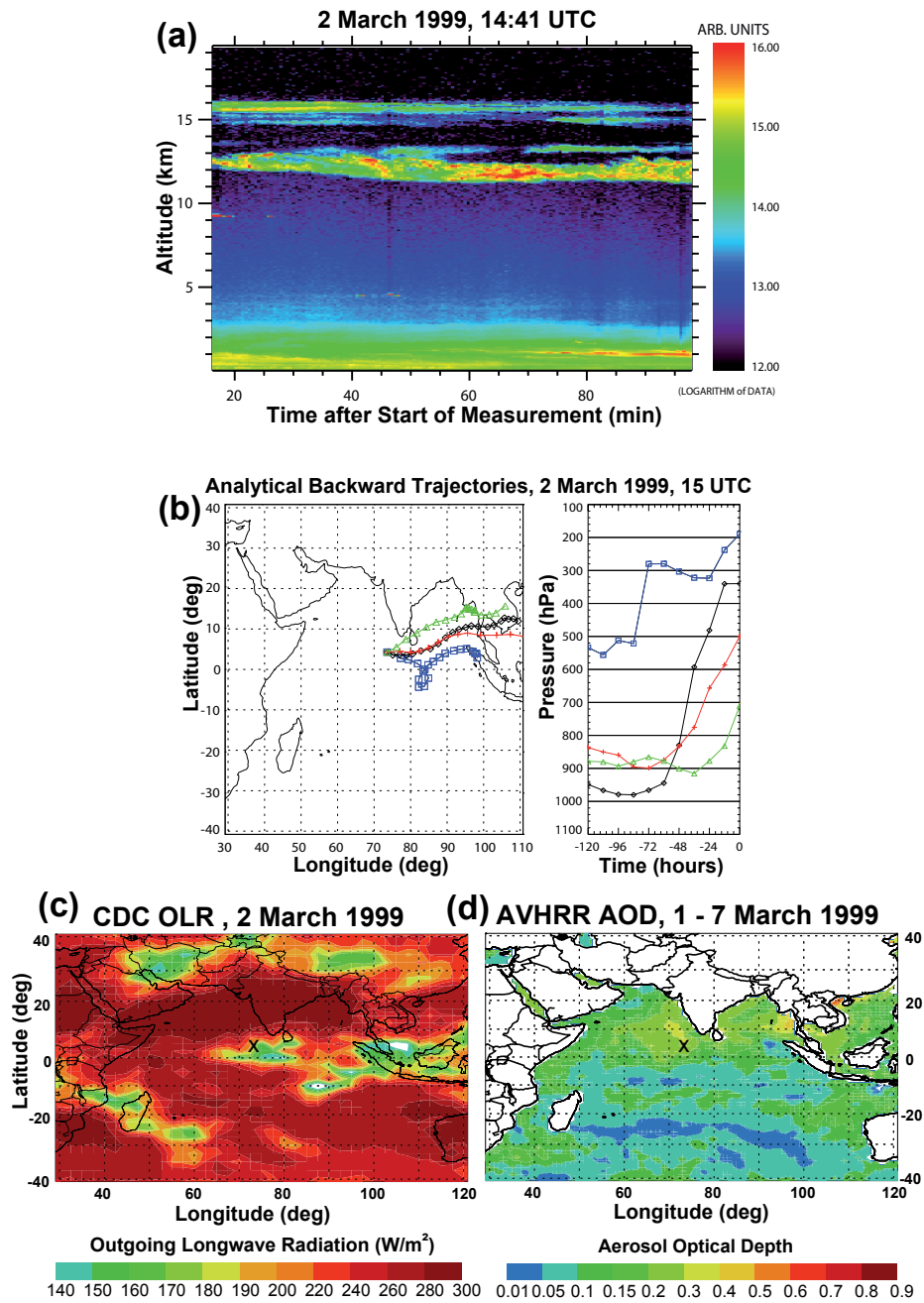


Figure 4.6: (a) Signal profile, (b) backward trajectories, (c) CDC OLR, and (d) AVHRR AOD for a cirrus case on 2 March 1999 (NE monsoon). The source regions of the trajectories ending over Hulule are located at the South China Sea and the Gulf of Bengal. Both region show relatively high values of aerosol optical depth. High values of OLR are omnipresent over the open sea of the Indian Ocean south of the Maldives. The 'x' marks the location of the lidar site.

Despite the complete change in the circulation pattern the lidar still detected aerosol layers in July 1999 [see Fig. 4.8 (a) at about 5 km]. As shown by the red trajectory in Fig. 4.8(b), these layers originated from the Arabian Peninsula. They have been identified as desert-dust layers (Müller et al. 2003; Franke 2003). According to Franke (2003) these lofted layers contributed up to 0.24 to the overall AOD. Even higher values of AOD were found in the northern Arabian Sea [see Fig. 4.8 (d)]. But due to its large distance and the location northwest of the Maldives these aerosols should not have had an impact on clouds detected by the lidar. Because the mean AOD value for July 1999 was 0.12, the isolated layers did not contribute much to the average values.

In October 1999 the air was clear in an area of about 10° around the Maldives [see Fig. 4.9 (d)]. The AVHRR AOD values were about 0.1 to 0.15, representing maritime conditions. However, high values of AOD were found over the open Indian Ocean west of Indonesia. A possible source for these aerosols are forest fires. Especially in fall of 1997 and 1998 scientists reported extensive, wide-spread forest fires in Indonesia (Anderson et al. 1999). For September 1999, Anderson and Bowen (2000) reported

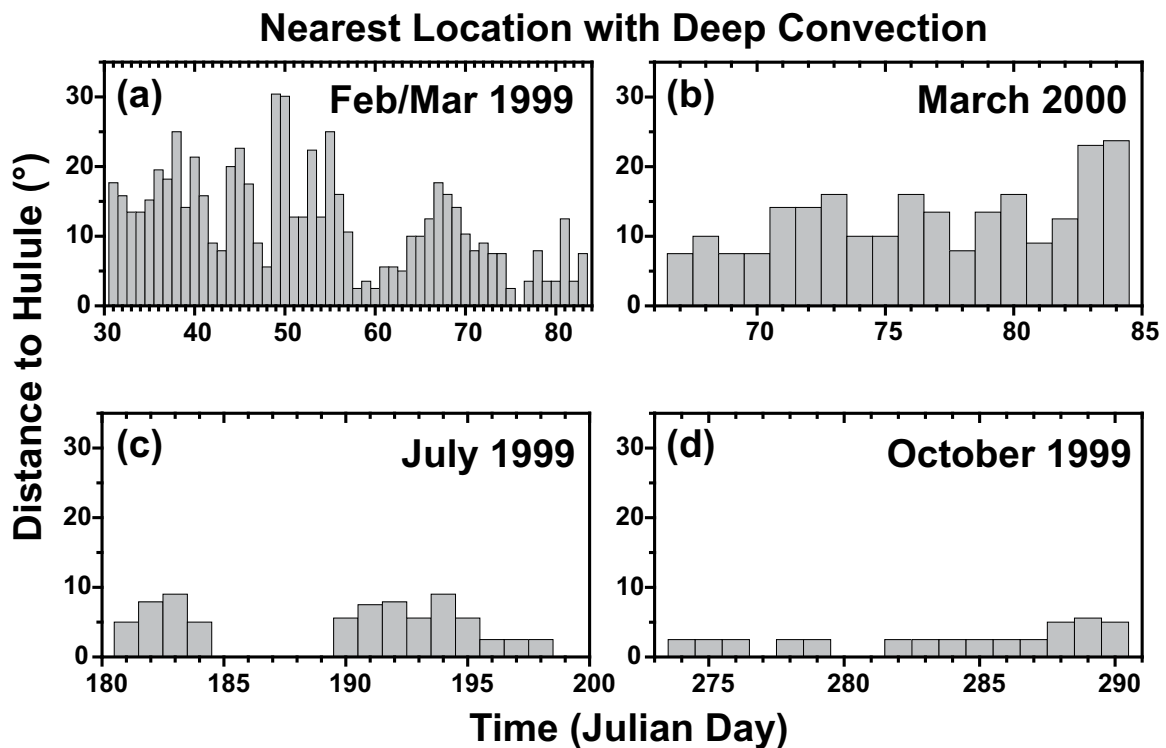


Figure 4.7: Distance of regions with deep convection to Hulule for all four campaigns. Values retrieved from CDC OLR data. $1^\circ \approx 110$ km.

the longest lasting fire in South Sumatra since 1996. 14,000 ha of swamp burnt, and this has probably contributed to the pollution plume shown in Fig. 4.9 (d).

From Fig. 4.8 and 4.9 it might be concluded that the southwest monsoon does not lead to absolutely clean conditions over the Maldives. Possible sources for pollution are desert dust from Arabia and forest-fire aerosol from Indonesia. The impact of these aerosols is still lower than that of the Indo-Asian dust which is advected to the Maldives during the NE monsoon season. The AVHRR AOD data might also be affected by uncertainties in the data processing algorithm. Especially the unknown vertical distribution and single-scattering albedo of aerosols lead to considerable uncertainties of the AOD values (Chung et al. 2005). Nevertheless, especially the dust layers observed by the lidar in July 1999 should be considered in the comparison of the optical properties between the NE and the SW monsoon.

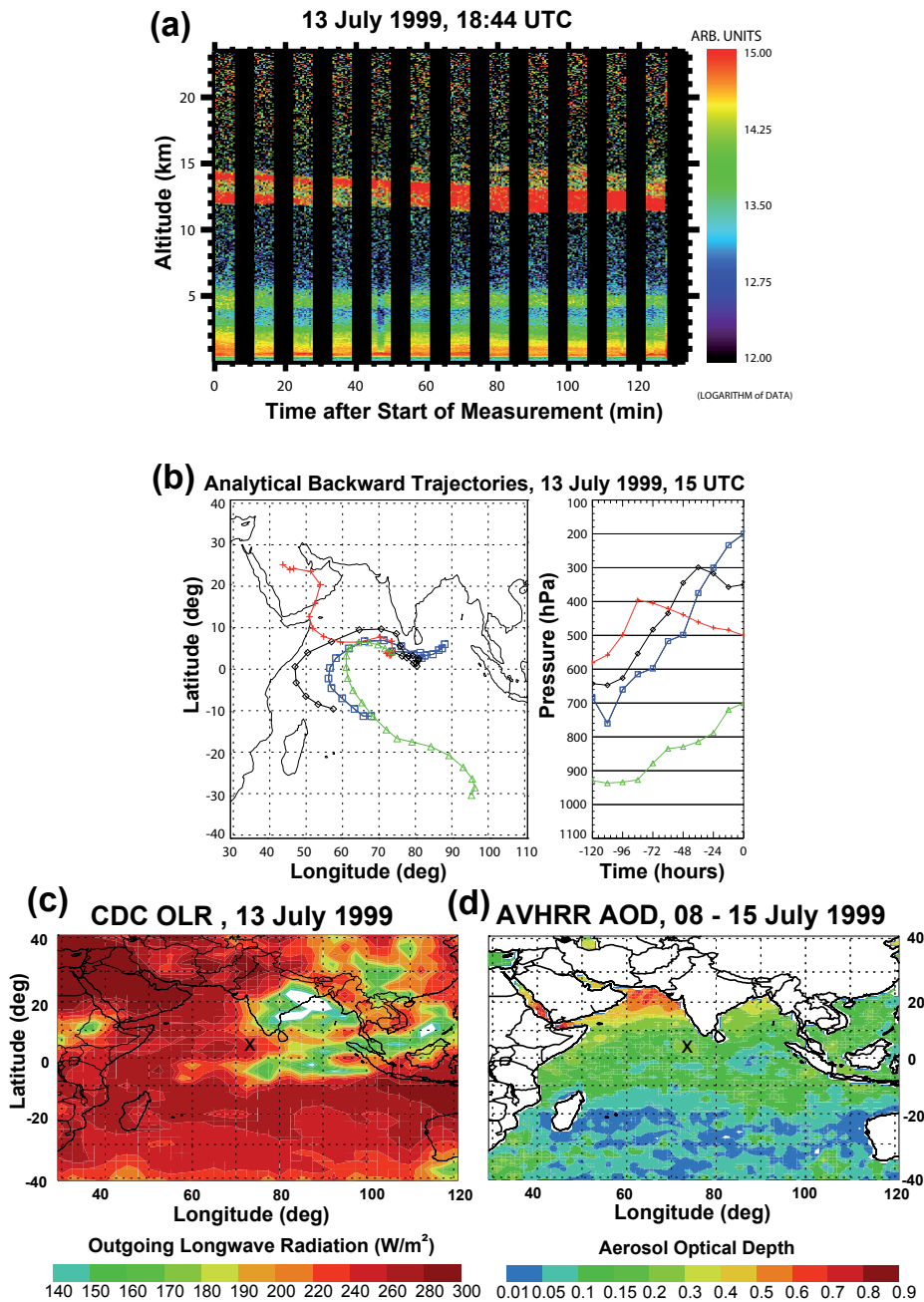


Figure 4.8: (a) Signal profile, (b) backward trajectories, (c) CDC OLR, and (d) AVHRR AOD for a cirrus case on 13 July 1999. The trajectories and the OLR show characteristics of the SW monsoon. The red trajectory indicates the source region of the dust layer at about 5 km in panel (a). Black vertical stripes in panel (a) are caused by measurements at two different zenith angles (30°, 60°). Only measurements at 30° zenith angle are shown. The ‘x’ marks the location of the lidar site.

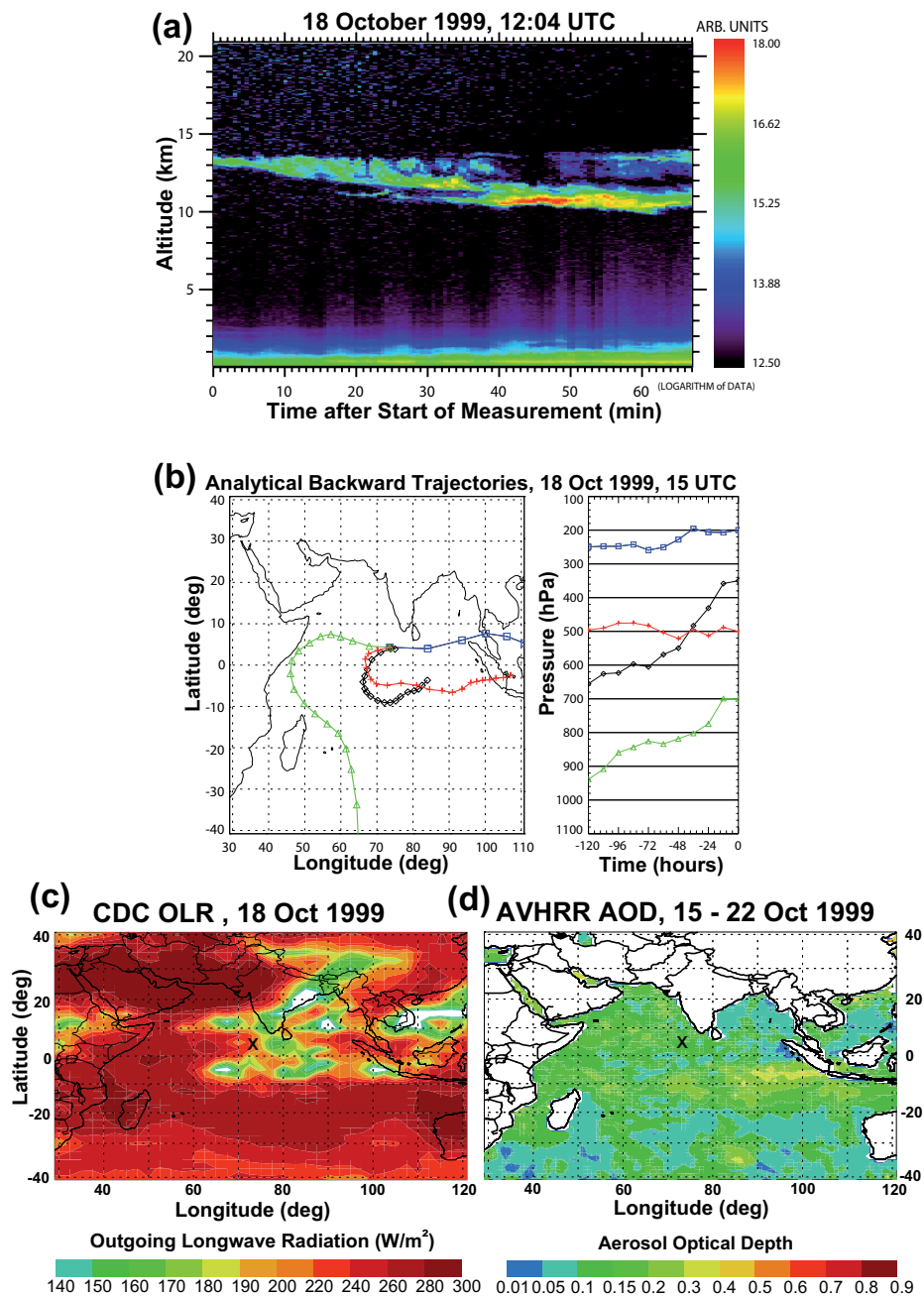


Figure 4.9: a) Signal profile, (b) backward trajectories, (c) CDC OLR, and (d) AVHRR AOD for a cirrus case on 18 October 1999 (SW monsoon). The relatively high AOD values shown over the open Indian Ocean in panel (d) are most likely forest-fire plumes from Indonesia. The ‘x’ marks the location of the lidar site.

Chapter 5

Results and Discussion

This chapter presents the results of the lidar data analysis. Cirrus cloud geometrical and optical properties are discussed by means of statistical datasets and time series. The findings are compared with existing cirrus cloud statistics from different regions of the tropics. Datasets for each monsoon season have been evaluated separately. This procedure is motivated by the fact that the two monsoon seasons are characterized by contrasting meteorological conditions. The need for the separation is also given by the ambition of this study to investigate whether there are pollution-induced differences in the cirrus characteristics between both monsoon seasons. Therefore, the lidar data of February and March 1999 and March 2000 have been merged to yield one dataset for the northeast monsoon. The data of July 1999 and October 1999 provide the basis for the southwest-monsoon dataset.

Table 5.1 presents basic information on the four field campaigns conducted by the IFT. Most observations have been performed in February and March 1999 during the intensive field phase of INDOEX. Together with the data of March 2000, 114 cirrus cases have been counted during the NE monsoon season. Nevertheless, a sufficient amount of 79 cirrus cases is still available for the SW monsoon season, providing a solid basis for statistical analyses. Altogether, a total number of 193 cirrus clouds were detected during an observational time of 14900 minutes out of a total measurement time of 29500 minutes. This corresponds to an occurrence frequency of 51%. It should be noted that during several measurements in October 1999 closed fields of altocumulus obscured the upper troposphere from the view of the lidar from the start to the end of the measurement. Hence, the detection of cirrus was not possible during these time periods. Of the total amount of 4004 measurement minutes in October 1999 altocumulus obscured the sky for about 1400 minutes. Periods with altocumulus shields during October 1999 have been excluded from the dataset. During the other

three field campaigns screening by lower-tropospheric and mid-tropospheric cloud layers was a negligible issue. Each cirrus is primarily characterized by its geometrical properties, i.e., cloud top height, cloud base height, and mean height, depth, and duration. Temperature information is provided by radiosonde data.

The white and the blue columns in the time series in Fig. 5.1 illustrate for how long the lidar was operated and for how long cirrus was detected by the lidar per measurement day, respectively. Figure 5.1 (a) and (b) present NE monsoon data. Both graphs show strong temporal fluctuations of the ratio between measurement time and cirrus occurrence. As discussed in Sec. 4.2, these variations are strongly correlated to stratospheric waves and the distance to deep convection. The SW monsoon data in panels (c) and (d) of Fig. 5.1 do not show such a considerable variation in the ratio between cirrus occurrence and measurement length. The permanent presence of deep convection in the Maldives region during this season, caused by the close distance to the ITCZ, provides continual conditions for cirrus formation.

Table 5.1: Basic information about the underlying lidar dataset of this study. The columns are arranged with respect to the monsoon seasons. The total measurement time in October 1999 is shown in parentheses. During 1400 minutes of this time altocumulus obscured the sky, so that no cirrus clouds could be detected.

	NE Monsoon		SW Monsoon	
	Feb/Mar 1999	March 2000	July 1999	October 1999
Per Field Campaign				
No. of meas. days	41	16	16	20
No. of meas. min.	16274	4487	6085	2600 (4004)
Cirrus cases	97	17	49	30
Cirrus detected (min)	7391	1081	4802	1609
Cirrus detected (%)	45	24	79	62
Per Season				
No. of meas. min.	20761		9289	
Cirrus cases	114		79	
Cirrus detected (min)	8472		6411	
Cirrus detected (%)	41		69	

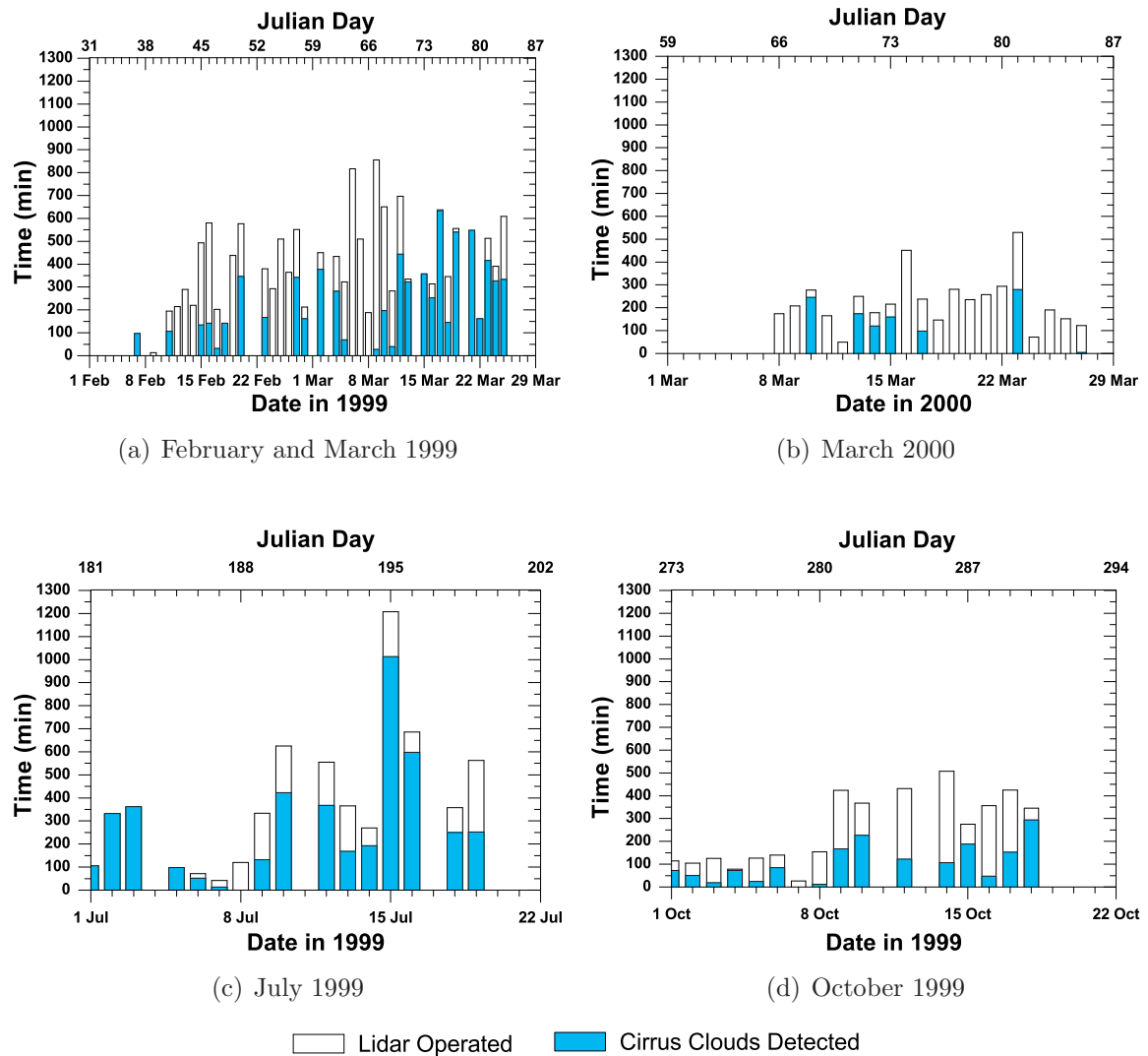


Figure 5.1: The four graphs illustrate for how many minutes per day the lidar was operated (white columns) and for how long cirrus was detected during the measurements (blue columns). Each graph shows one campaign; (a) and (b) represent the NE monsoon and (c) and (d) the SW monsoon season.

5.1 Geometrical Cirrus Properties

5.1.1 Results

In this section, primary macrophysical cloud properties are presented. The results are based on all observed cirrus cases mentioned in Table 5.1. Table 5.2 provides an overview of the seasonal mean values of height and temperature of the cloud boundaries and of the cloud depth. Standard deviations are given in parentheses behind the mean values. Mid-cloud values for height and temperature are given as additional information.

The mean lower boundary of all cirrus clouds detected during the four field campaigns is 11.6 km. This value corresponds to an average temperature of -48 °C. The mean cloud top is located at an altitude of 13.5 km or at -63 °C. The cirrus clouds are on average 1.9 km thick with a seasonal variation of 0.6 km. The lower mean cloud depth with a value of 1.6 km was observed during the NE monsoon. The mean cloud base during the SW monsoon is located about 0.5 km below the NE-monsoon cloud base. Remarkable is the agreement between the mean cloud top heights of the NE and the SW monsoon. During both seasons the mean cloud top is located at 13.5 km. In contrast to the altitude of the cloud top, the mean temperature of the upper cirrus boundary during the NE monsoon is about 1 K lower than during the SW monsoon.

Figure 5.2 shows seasonal and total frequency distributions of cirrus cloud base height, cloud top height, and cloud depth. Frequency distributions of cloud-base, mid-cloud, and cloud-top temperatures are shown in Fig. 5.3. As can be seen from Fig. 5.2

Table 5.2: Mean values and standard deviations (in parentheses) of primary macrophysical cloud properties. The values are given for all observed cirrus cases as well as for the northeast monsoon and the southwest monsoon.

	All Cases		NE Monsoon		SW Monsoon	
Analyzed cases	193		114		79	
Cloud Base Height (km)	11.6	(1.9)	11.8	(1.9)	11.3	(2.0)
Cloud Top Height (km)	13.5	(1.5)	13.5	(1.6)	13.5	(1.5)
Cloud Depth (km)	1.9	(1.1)	1.6	(0.9)	2.2	(1.3)
Mid-Cloud Height (km)	12.6	(1.6)	12.7	(1.6)	12.4	(1.6)
Cloud Base Temperature (°C)	-48	(15)	-49	(15)	-46	(15)
Cloud Top Temperature (°C)	-63	(12)	-63	(12)	-62	(12)
Mid-Cloud Temperature (°C)	-56	(13)	-56	(13)	-54	(13)

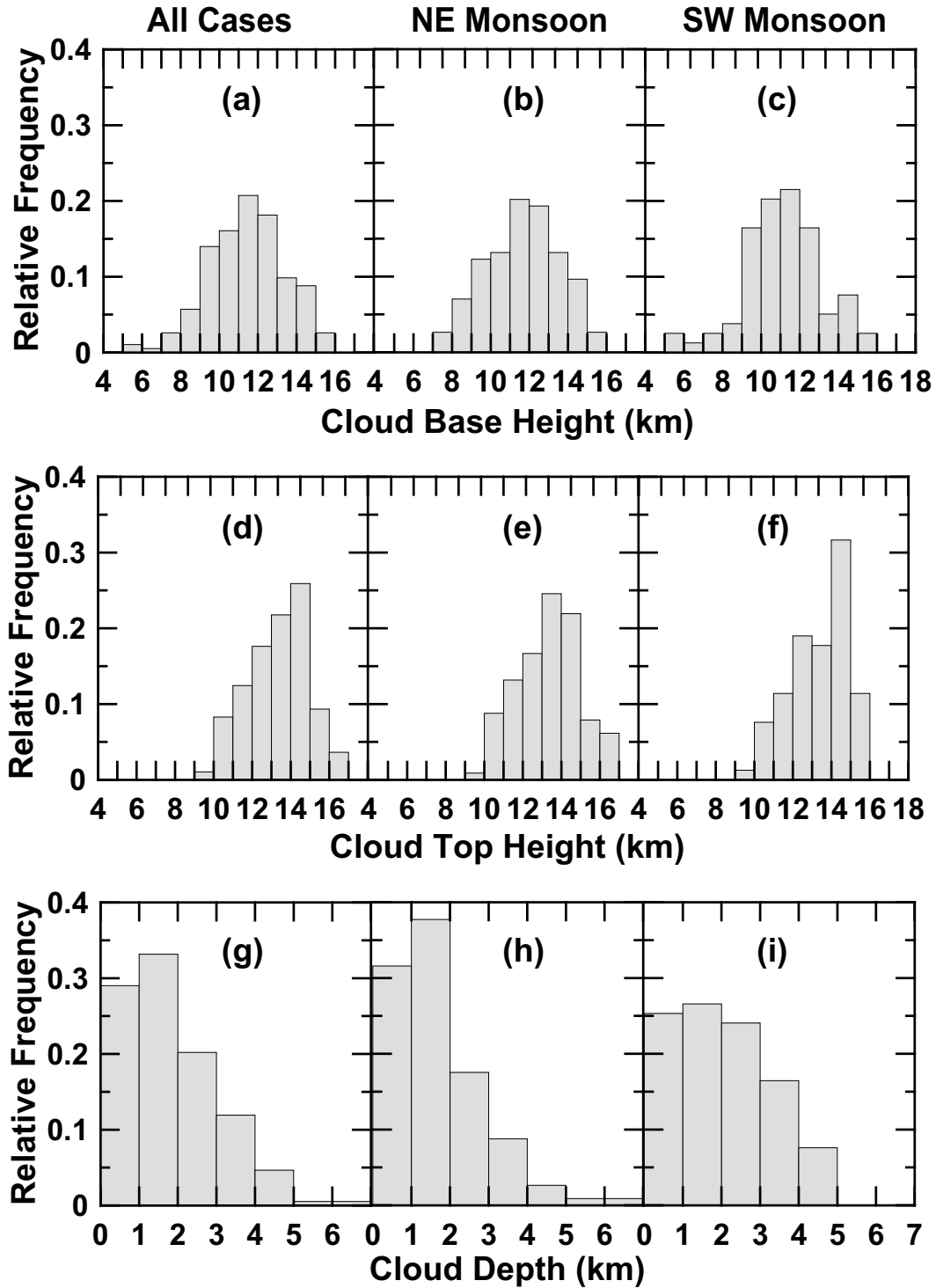


Figure 5.2: Frequency distributions of (a)–(c) cloud base height, (d)–(f) cloud top height, and (g)–(i) cloud depth for all observed cirrus cases, the NE monsoon season, and the SW monsoon season.

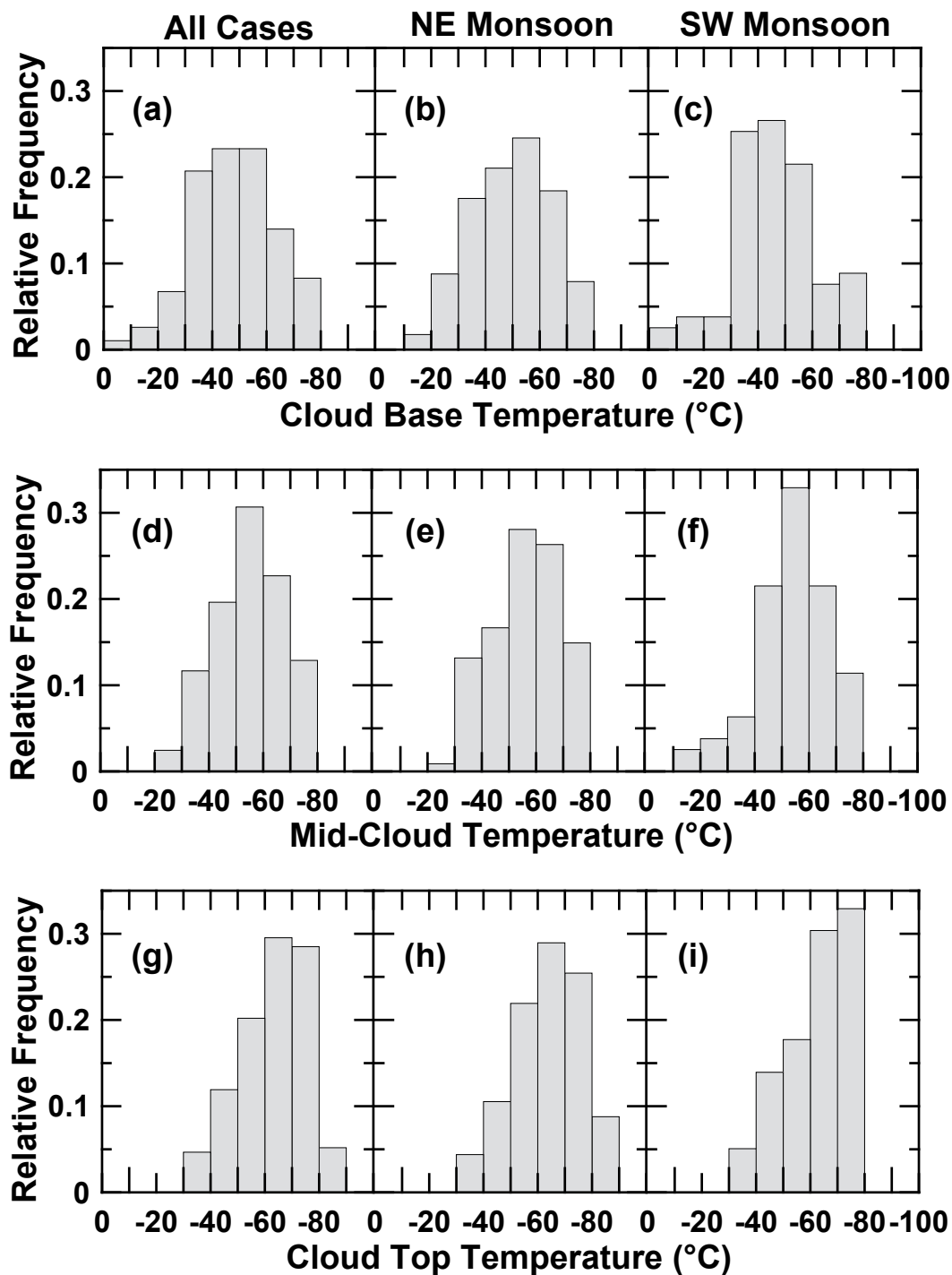


Figure 5.3: Frequency distributions of (a)–(c) cloud-base temperature, (d)–(f) mid-cloud temperature, and (g)–(i) cloud-top temperature for all observed cirrus cases, the NE monsoon season, and the SW monsoon season.

(a)–(c) only a small fraction of the cloud bases is located at altitudes below 9 km. The lowest base heights have been observed during the SW monsoon. It should be noted that these clouds, with a cloud base below 6 km and temperatures close to -10 °C, were definitively cirrus clouds. They appeared like cirrus fibratus¹ in the time-resolved signal profile. Most other clouds below 9 km that are included in the statistics show cirrostratus-like characteristics.

The comparison of Fig. 5.2 (b) and 5.2 (c) shows a higher frequency of clouds with a base above 13 km during the NE monsoon. As can be seen in Fig. 5.2 (f) clouds were never detected above 16 km during the SW monsoon. Instead, there is a pronounced peak showing that about 32% of all SW monsoon clouds had their upper boundary between 14 and 15 km. Only a small percentage of clouds appeared above 15 km. This boundary is also shown in Fig. 5.3 (i), where no cloud top reaches a temperature level of less than -80 °C. Instead, 33% of all cloud tops are located between -70 and -80 °C. The NE monsoon provided different conditions. 10% of all cirrus clouds reached temperature levels below -80 °C [see Fig. 5.3 (h)], and clouds with tops above 16 km occurred [see Fig. 5.2 (e)]. Remarkable differences between both monsoon seasons are also given in the distribution of the cloud depth [Fig. 5.2 (h)–(i)]. Cirrus clouds during the NE monsoon more frequently appeared rather thin in comparison to clouds detected during the SW monsoon.

5.1.2 Discussion

A possible reason for the observed differences between both seasons are the contrasting meteorological conditions during the NE and the SW monsoon. Especially the stronger convective activity in July and October 1999 should play a dominant role. Due to the permanent presence of deep convection around Hulule during the SW monsoon (see Fig. 4.7) the detected clouds were most likely fresh remnants of cumulonimbus anvils. Thus they should appear rather thick, which is the case (see Table 5.2). Deep convection could also be responsible for the sharp boundary of the cloud top between 13 and 14 km during the SW monsoon [see Fig. 5.2 (f)]. The dissolution process might not have started before clouds were detected at the upper edge of deep convective cells (Liu and Zipser 2005). In contrast, NE monsoon clouds usually had their origin in greater distance to the Maldives. Therefore, they had already aged before they were detected with the lidar. Entrainment and detrainment of air at the cloud boundaries during the life cycle of the cirrus layer cause a decrease of the cloud thickness until

¹Cirrus fibratus: Detached clouds or thin cloud veils, consisting of nearly straight or irregularly curved filaments.

the cloud decays (Platt et al. 1989; Sassen et al. 1989; Sivakumar et al. 2003). The maintenance of anvil cirrus for several hours to more than a day also requires a slow ascent of the clouds, because radiative heating affects the cirrus. If the cirrus clouds would remain at their initial level, they would dissolve quickly (Ackerman et al. 1988; Jensen et al. 1996).

The location of the tropopause level which varies in height and temperature between both monsoon seasons probably also plays a role in the distribution of the clouds. Table 5.3 shows mean values of the lapse-rate tropopause for the NE and the SW monsoon seasons. According to the values determined from about 200 radiosonde ascents, the lapse-rate tropopause is on average located at an altitude of 16.3 km at a temperature level of -81 °C. With 16.7 km and -83 °C the NE monsoon tropopause lies about 1 km above and 5 K below the tropopause during the SW monsoon season. These differences at least explain why there were no clouds observed at temperatures below -80 °C during the SW monsoon [see Fig. 5.3 (i)].

The general opinion that upper-tropospheric cirrus is decoupled from lower-tropospheric processes as deep convection is corroborated by the underlying dataset. As described in Sec. 4.2, formation mechanisms and appearance vary between both cirrus types. Upper-tropospheric cirrus formed by large-scale uplift or wave activity is usually physically thin and has a laminar structure. Blow-off and anvil cirrus appears more structured and has variable cloud boundaries. Figure 5.4 presents three different frequency distributions of the cloud depth. The thick line represents the depth distribution of clouds with a base below 10 km. These clouds show the highest variability in cloud depth. They represent 17% of all observed cirrus cases and are on average 3.3 km thick. Clouds with a base between 10 and 14 km (dashed line) have a lower variability in cloud depth but are still, on average, about 1.9 km thick. They have a mean base height of 11.7 km and with 69% the highest frequency of occurrence. The lowest variability in cloud depth is shown by the 14% of all observed cirrus clouds with a base above 14 km. The mean depth of these clouds is 0.8 km. Table 5.4 summarizes the derived values for the three cloud-base intervals.

The indications for different cloud types are further emphasized in Fig. 5.5 which

Table 5.3: Mean values of height and temperature of the lapse-rate tropopause.

Standard deviations are given in parentheses.

	All Cases	NE Monsoon	SW Monsoon
Tropopause Height (km)	16.3 (1.0)	16.7 (0.9)	15.5 (0.4)
Tropopause Temperature (°C)	-81 (4)	-83 (3)	-77 (2)

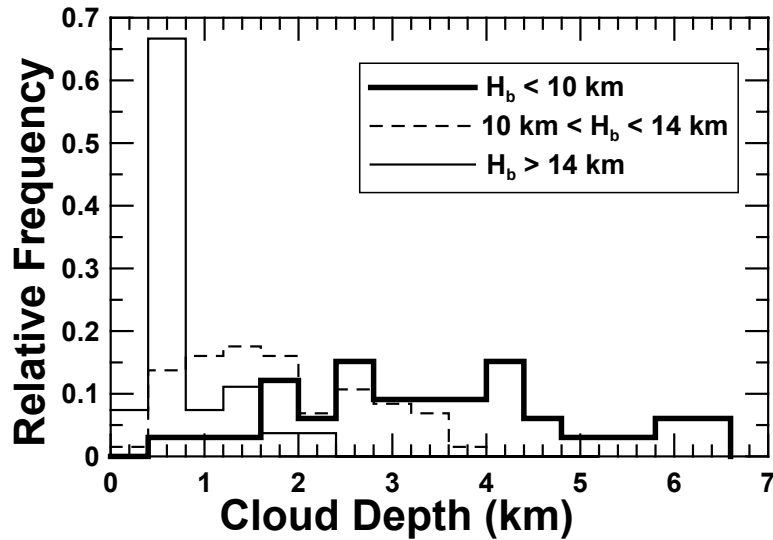


Figure 5.4: Frequency distributions of cloud depth for clouds with $H_b < 10$ km (thick solid line), $10 \text{ km} < H_b < 14$ km (dashed line), and $H_b > 14$ km (thin solid line). Data of both monsoon seasons are included.

shows the distribution of the distance between the cirrus cloud top and the lapse-rate tropopause. The graph contains the data of 140 cirrus cases of both monsoon seasons. The most recent available radiosonde with respect to the cirrus occurrence time was used to calculate the distance. Two maxima are shown in the distribution. One distinct maximum of occurrence is located right below the tropopause level, where about 18% of all cirrus tops were found. Another one can be found about 3 km below the tropopause. Whereas the maximum of occurrence close to the tropopause most likely is dominated by cirrus clouds induced by wave activity, the lower maximum appears to be related to blow-off and anvil cirrus from cumulonimbus clouds. About 7% of the cirrus cloud tops were found above the lapse-rate tropopause level. Clouds above the tropopause have been reported previously (Winker and Trepte 1998; Sivakumar et al. 2003).

Table 5.4: Frequency of occurrence, mean geometrical depth, and mean cloud base height for cirrus clouds with a base H_b below 10 km, between 10 and 14 km, and above 14 km.

	$H_b < 10$ km	$10 \text{ km} < H_b < 14$ km	$H_b > 14$ km
Frequency of Occurrence (%)	17.1	68.9	14.0
Mean Cloud Base Height (km)	8.8	11.7	14.6
Mean Geometrical Depth (km)	3.3	1.9	0.8

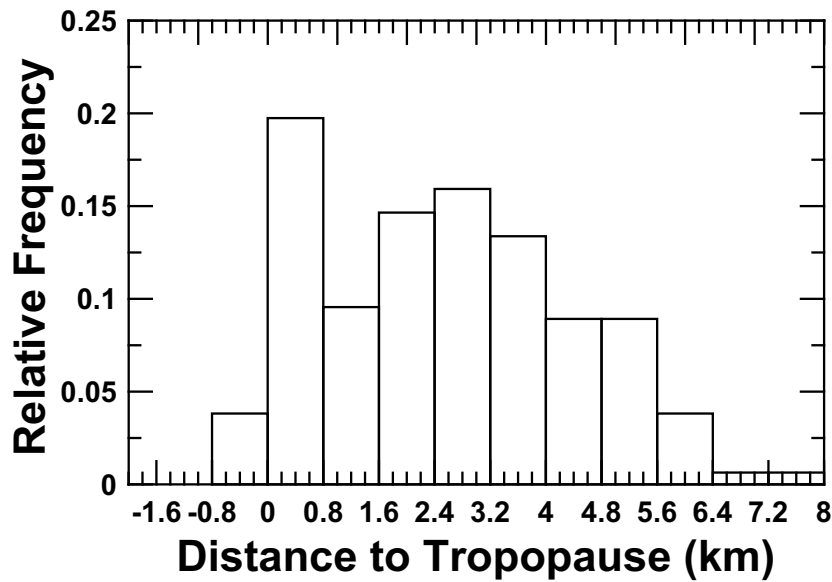


Figure 5.5: Frequency distribution of the distance between cloud top and the respective lapse-rate tropopause. The underlying dataset contains the data of both monsoon seasons.

However, uncertainties arise from the necessary conversion of pressure, measured by the radiosonde, into height. Furthermore, temporal and spatial changes in the vertical temperature profile are unknown. Because of the drift of the balloon, radiosonde and lidar measure at different locations in the upper troposphere.

Similar characteristics of cloud-depth distributions for the three different cloud base height intervals shown in Fig. 5.4 were also found by Comstock et al. (2002) and Pace et al. (2003). Differences result from the definition of the upper cloud base height only. Whereas it was 14 km at the Maldives, Comstock et al. (2002) found a characteristic value of $H_b > 15$ km and Pace et al. (2003) came up with $H_b > 14.5$ km. The differences are probably due to the different measurement sites. The dataset presented by Comstock et al. (2002) was collected at Nauru (0° , 167° E) in the western Pacific region which is known to have the highest altitude of occurrence of thin cirrus clouds (Wang et al. 1996). Pace et al. (2003) characterized clouds at the Seychelles (4.4° S, 55.3° E).

The differences in the cloud characteristics between Nauru and the Maldives are also obvious from the height of the cloud boundaries. At Nauru the highest occurrence frequency of the cloud base is at about 14 km, whereas it lies between 11 and 12 km at the Maldives [see Fig. 5.2 (a)]. In contrast to about 14 km at the Maldives [see Fig. 5.2 (d)], the cloud top in the western Pacific region has its maximum of occur-

rence at about 16 km. A higher mean tropopause height of 16.9 km over the western Pacific warm pool (Sassen et al. 2000) in contrast to 16.3 km over the Maldives (see Table 5.3) implies differences in the meteorological conditions between both regions. High sea surface temperatures in the western Pacific region are also supposed to enhance deep convection (Ramanathan and Collins 1991; Liu and Zipser 2005). The observed differences in the height distribution of the cirrus clouds cannot be explained by different definitions of cirrus. Comstock et al. (2002) included all ice clouds with a base above 7 km in their statistics. The three cirrus cases with a base below 7 km that are included in this study for the Maldives do not have a considerable impact on the statistics.

The four-year geometrical cirrus cloud statistics of the tropical Indian station Gadanki (13.5° N, 79.2° E) presented by Sivakumar et al. (2003) and Sunilkumar and Parameswaran (2005) are also in relatively good agreement with the Maldives dataset. Both publications deal with the same dataset but consider different aspects of the cloud properties. The occurrence frequency decreases in the same manner with increasing cloud depth as shown in Fig. 5.2 (g). The clouds at Gadanki show a similar frequency distribution of the mid-cloud height as presented in Fig. 5.6 (a). However, the distribution of the cloud centers at Gadanki is shifted by 0.5 km towards higher altitudes or by 5 K towards lower temperatures. It therefore agrees better with the frequency distribution shown in Fig. 5.3 (e) which presents the situation as it was during the NE monsoon. The distribution of the cloud depth per mid-cloud temperature interval that is shown in Fig. 5.6 (b) is in good agreement with the studies from

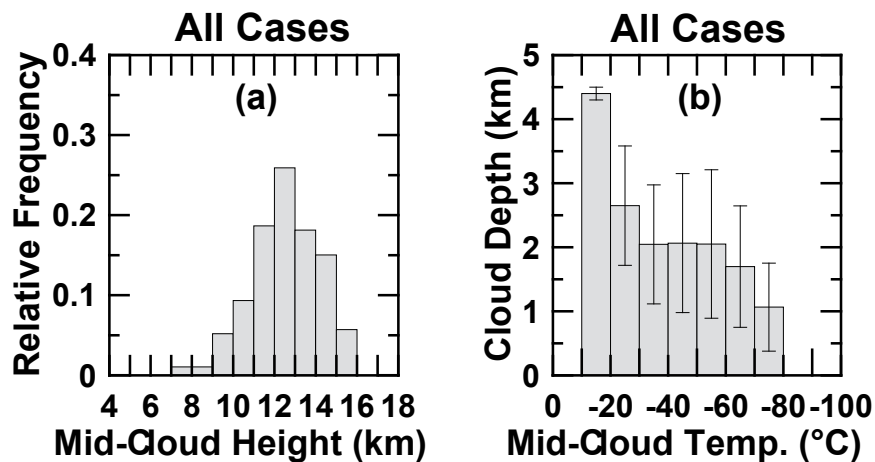


Figure 5.6: (a) Relative frequency of occurrence of mid-cloud height. (b) Mean cloud depth per mid-cloud temperature interval and standard deviations. Both graphs include the cirrus cases of both monsoon seasons.

Gadanki, Nauru, and the Seychelles. The values vary in the range of the standard deviation given in Fig. 5.6 (b), but show all the same tendency of decreasing cloud depth with decreasing temperature.

Sivakumar et al. (2003) also observed the distribution of the cloud top's distance to the tropopause (see Fig. 5.5) with one maximum right below the tropopause and another one about 3 to 4 km below the tropopause. In contrast to the findings for the Maldives region, 25% of the cirrus clouds at Gadanki were very close to the tropopause and another 25% of all clouds were even reported to have appeared in altitudes up to 3 km above the tropopause. This is possibly caused by the fact that Sivakumar et al. (2003) used radiosonde data from a station located 120 km away from Gadanki.

5.2 Optical Cirrus Properties

5.2.1 Results

The characterization of the optical cirrus properties is based on a smaller dataset than presented in Sec. 5.1. Several cirrus cases had to be excluded from the primary dataset because of insufficient accuracy of the retrieved optical properties (see Sec. 3.4). In general, the following conditions led to an exclusion: too much signal noise, too short cloud occurrence time, too inhomogeneous cloud structure, lower clouds obstructing cirrus layers.

Figure 5.7 shows the number distribution of analyzed cirrus cases per mid-cloud temperature interval of 10 K. Temperature is the dominant parameter in cloud processes. It determines the radiative transfer and thus the strength of the adiabatic processes in the cloud. Microphysical parameters such as particle phase, size, and shape strongly depend on temperature. It is therefore a preferred parameter for optical and microphysical cirrus studies (Sassen and Comstock 2001; Heymsfield and McFarquhar 2002; Pace et al. 2003; Sunilkumar and Parameswaran 2005).

A first overview of the optical properties of the analyzed clouds is given in Table 5.5. Seasonal values of frequency, mean optical depth $\bar{\tau}$, and mean extinction coefficient $\bar{\alpha}$ of subvisible cirrus, thin cirrus, and cirrostratus are shown. The classification of the cloud types follows the scheme published by Sassen and Cho (1992) which was introduced in Chapter 4. About 20% of all analyzed cases are classified as subvisible cirrus, about 50% as thin cirrus, and 30% as cirrostratus. The seasonal values vary, indicating more

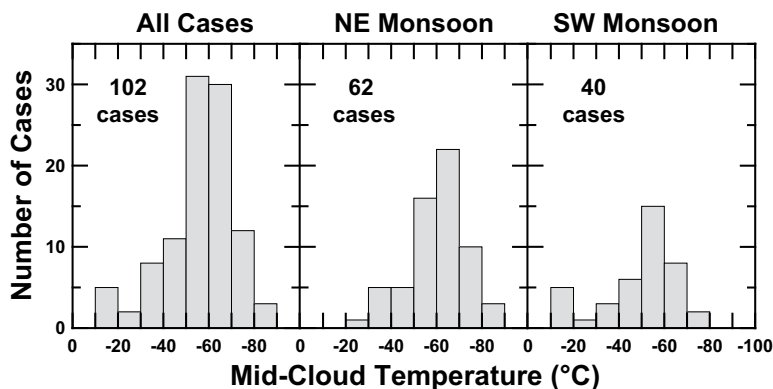


Figure 5.7: Frequency distributions showing the number of cases per mid-cloud temperature interval that have been analyzed in order to obtain optical cirrus properties. Distributions are given for all cases, NE monsoon, and SW monsoon.

Table 5.5: Seasonal frequency, mean optical depth $\bar{\tau}$, and mean extinction coefficient $\bar{\alpha}$ of subvisible cirrus, thin cirrus, and cirrostratus. Standard deviations of the mean values are given in parentheses. The cloud types are classified after Sassen and Cho (1992).

	Subvisible Ci $\tau < 0.03$	Thin Cirrus $0.03 < \tau < 0.3$	Cirrostratus $\tau > 0.3$
All Cases			
Frequency	18%	52%	30%
$\bar{\tau}$	0.015 (0.008)	0.13 (0.08)	0.64 (0.30)
$\bar{\alpha}$ (km ⁻¹)	0.012 (0.009)	0.06 (0.03)	0.21 (0.11)
NE Monsoon			
Frequency	24%	56%	20%
$\bar{\tau}$	0.014 (0.008)	0.13 (0.07)	0.57 (0.22)
$\bar{\alpha}$ (km ⁻¹)	0.013 (0.009)	0.07 (0.03)	0.22 (0.10)
SW Monsoon			
Frequency	5%	48%	47%
$\bar{\tau}$	0.014 (0.003)	0.14 (0.08)	0.68 (0.33)
$\bar{\alpha}$ (km ⁻¹)	0.010 (0.005)	0.05 (0.03)	0.20 (0.12)

subvisible cirrus (24%) during the NE monsoon and more cirrostratus (47%) during the SW monsoon. The mean optical depth $\bar{\tau}$ of thin cirrus and cirrostratus is a little lower during the NE monsoon than during the SW monsoon. The opposite is the case for the mean cloud extinction coefficient $\bar{\alpha}$. Here, the values of all cirrus types are slightly higher during the NE monsoon season. However, taking the standard deviation into account, the values of the NE and the SW monsoon do not differ significantly. In general, $\bar{\alpha}$ increases with increasing optical depth.

The dependence of cirrus optical depth, mean extinction coefficient, and cloud depth on temperature is presented in Fig. 5.8. Optical depth and mean extinction coefficient strongly decrease with decreasing temperature. Geometrical and optical depth also show seasonal differences. As shown in Fig. 5.8 (h) and (i) the analyzed clouds are generally thicker during the SW monsoon. The same is the case for the optical depth. Except for the range between -20 and -30 °C, τ is approximately 30% higher during the SW monsoon [see Fig. 5.8 (b) and (c)]. The mean extinction coefficient does not indicate a seasonal variation.

No relevant correlation between the retrieved lidar ratio and mid-cloud temperature was found (see Fig. 5.9). For all temperatures the values vary around 18 sr. On average,

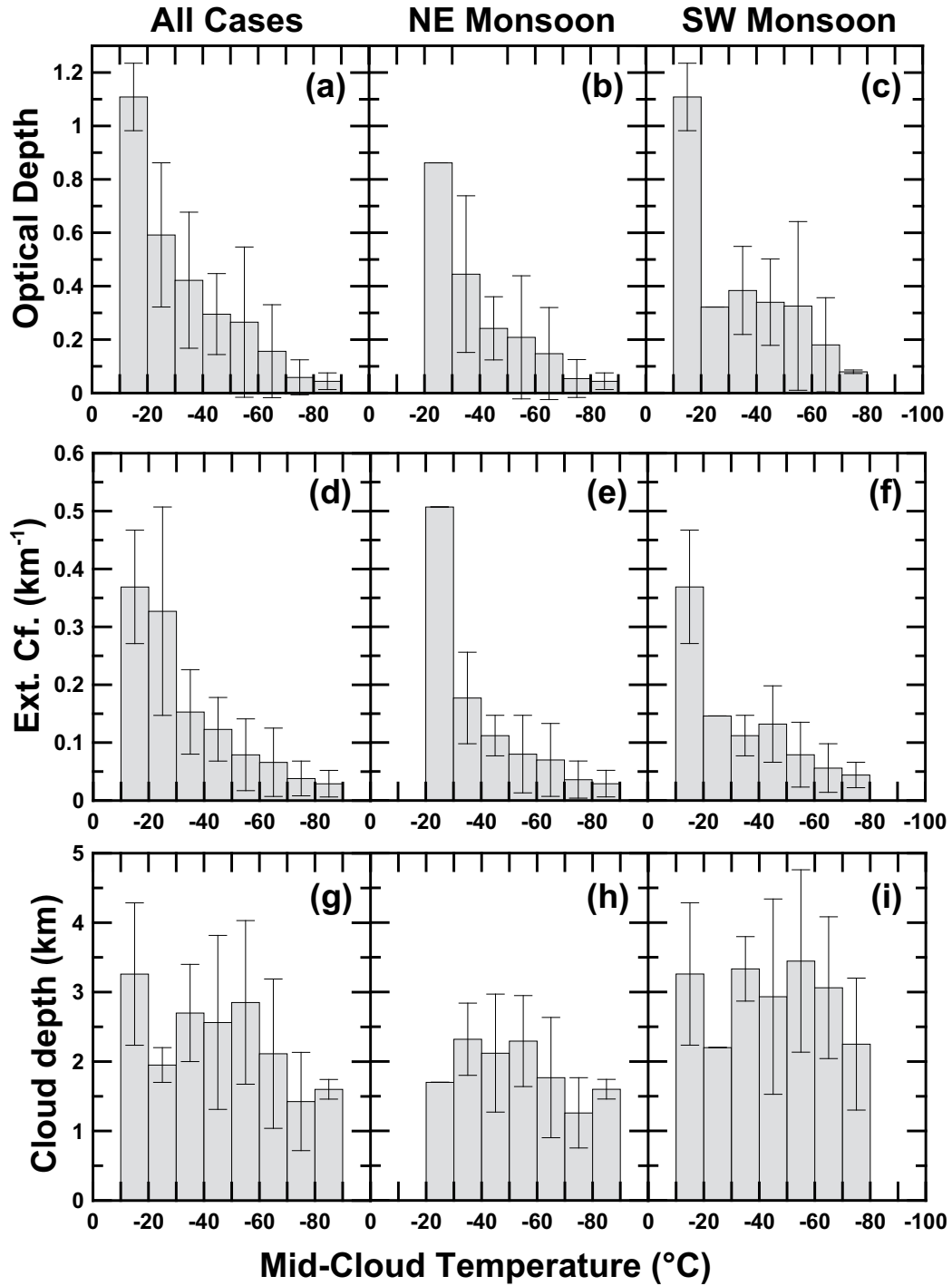


Figure 5.8: Frequency distributions of (a)–(c) mean optical depth , (d)–(f) mean extinction coefficient, and (g)–(i) cloud geometrical depth with respect to mid-cloud temperature intervals of 10 K for all cases, NE monsoon, and SW monsoon.

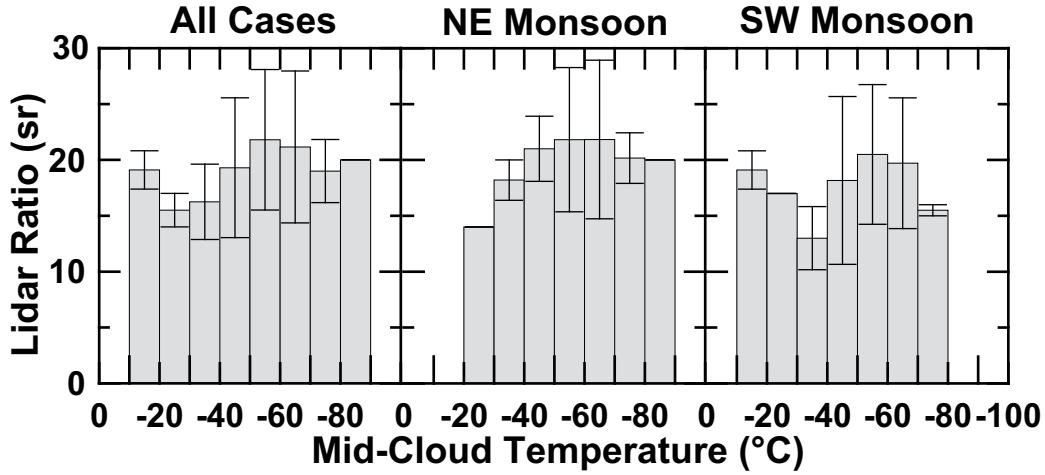


Figure 5.9: Mean lidar ratio per mid-cloud temperature interval. The dataset includes values retrieved with the forward-backward and the instability methods (see Sec. 3.4.2).

the lidar ratio is $S = 21 \pm 6$ sr during the NE monsoon and $S = 19 \pm 6$ sr during the SW monsoon season. The data presented in Fig. 5.9 include only those cases for which the lidar ratio could be retrieved with the forward-backward or the instability method (see Sec. 3.4.2).

5.2.2 Discussion

Figure 5.8 (c) shows higher values of the optical depth during the SW monsoon. This basically results from the higher cloud depth [Fig. 5.8 (i)] during this season. Thus the impact of deep convection that was omnipresent in the Maldives region during the SW monsoon is reflected in these high values of optical and geometrical depth.

Figure 5.8 (a) presents the average optical depth per temperature interval derived from all analyzed cirrus cases. It shows a well-defined slope of the optical depth with increasing temperature. Such a behavior cannot be found in any other publication. Nevertheless, Sunilkumar and Parameswaran (2005) found a relatively strong, almost exponential increase of the optical depth with increasing temperature. But their optical-depth values are lower than those determined from the Maldives dataset. Sunilkumar and Parameswaran (2005) found a mean optical depth of about 0.13 for temperatures between -40 and -50 °C, whereas it was 0.3 for the Maldives.

The analysis of the dataset from the Seychelles (Pace et al. 2003) revealed a rather constant average optical depth of about 0.7 at temperatures above -60 °C. But at temperatures between -60 and -90 °C the optical depth decreased rapidly from

about 0.5 to 0.003. Reasons for the observed differences between the three datasets of Gadanki, the Seychelles, and the Maldives are unclear. They might result from different data analysis methods. One possibility may be differences in the definition of a single cirrus cloud layer. Pace et al. (2003) defined cloud layers separated by more than 400 m as different clouds. In the present study layers were evaluated separately when more than 800 m of clear air appeared between them. Thinner clouds would also lead to lower optical depths. For the analysis of the Gadanki dataset, Sunilkumar and Parameswaran (2005) applied a constant lidar ratio of $S = 20$ sr to all cirrus cases. This might lead to an underestimation of the optical depth of clouds that actually had a higher lidar ratio. The strong increase of the optical depth at temperatures above -30 °C is not shown by Pace et al. (2003) and Sunilkumar and Parameswaran (2005). These authors excluded ice clouds warmer than -30 °C from their statistics.

Figure 5.10 presents frequency distributions of optical depth, mean extinction coefficient, and lidar ratio of the Maldives dataset. During the NE monsoon the optical depth and the mean extinction coefficient show a higher frequency of low values than during the SW monsoon. Whereas 50% of all analyzed cirrus cases of the NE monsoon had optical depths of $\tau < 0.1$, only 25% fulfilled this criterion during the SW monsoon. According to the average frequency of subvisible clouds of about 25% during the NE monsoon (see Table 5.5), 50% of all cirrus clouds with $\tau < 0.1$ in Fig. 5.10 (b) were subvisible ($\tau < 0.03$).

The distributions of the mean cloud extinction coefficient α given in Fig. 5.10 (d)–(f) show similar characteristics as the distributions of the optical depth τ . During the NE monsoon season a higher frequency of low values of α was found, whereas α tended to higher values during the SW monsoon.

A tendency to lower values of the lidar ratio during the SW monsoon is obvious from the comparison of Fig. 5.10 (h) and (i). The lidar ratio basically varies around 20 sr. During the SW monsoon about 25% of all lidar ratios were < 15 sr. During the NE monsoon season only about 10% were below that value.

Various publications report much higher occurrence rates for clouds with an optical depth below 0.1 than shown in Fig. 5.10 (a). In the study of Cadet et al. (2003) on a cirrus dataset collected at Réunion Island (21° S, 55° E) during a time period of five years, 80% of all analyzed cirrus clouds had an optical depth below 0.1. 50% of all analyzed cirrus clouds were subvisible. Comstock et al. (2002) published similar results for the frequency distribution of the optical depth. About 70% of all cirrus clouds had an optical depth of < 0.1 and about 25% to 30% were subvisible. For Gadanki, Sunilkumar and Parameswaran (2005) found that 65% of all observed cirrus clouds were subvisible.

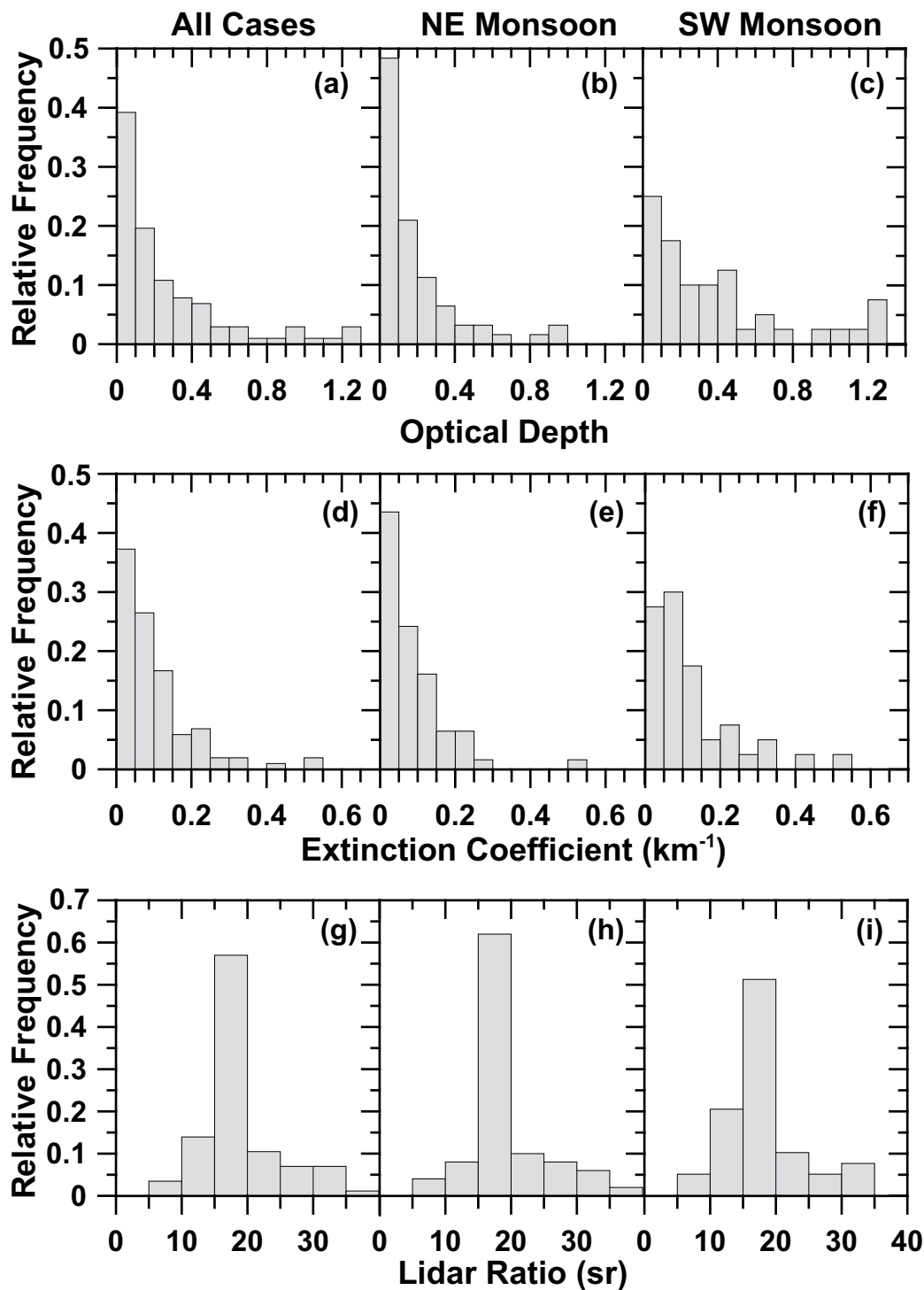


Figure 5.10: Frequency distribution of (a)–(c) cloud optical depth, (d)–(f) mean cloud extinction coefficient, and (g)–(i) lidar ratio for all analyzed cases, the NE monsoon, and the SW monsoon.

Figure 5.11 summarizes the findings for the extinction-to-temperature relations of nine different field campaigns. The original figure and further information can be found in Heymsfield and McFarquhar (2002). Values of the NE and the SW monsoon derived in this study and the values for the Seychelles (Pace et al. 2003) are added to the graph as colored circles. The data of the original figure were collected with aircraft. They include measurements of the First International Satellite Cloud and Climatology Project Regional Experiment I and II (FIRE I and FIRE II; Heymsfield et al. 1990; Heymsfield and Miloshevich 1995), the European Cloud and Radiation Experiment (EUCREX; Raschke et al. 1998), the Subsonic Aircraft: Contrail and Cloud Effects Special Study (SUCCESS; Toon and Miake-Lye 1998), the Central Pacific Experiment (CEPEX; Heymsfield and McFarquhar 1996), and measurements in Russia (Mazin 1995). As shown in Fig. 5.11, the values for the Maldives and for the Seychelles are very similar. Except for the temperature interval between -50 and -60 °C all lidar-derived values (Maldives and Seychelles) are in good agreement with the data of SUCCESS. SUCCESS was conducted over the continental USA between April and May 1996. CEPEX was carried out in the tropical Pacific Ocean, whereas all other campaigns were mid-latitude cirrus studies. However, only in the temperature ranges between -20 and -30 °C and -50 to -60 °C the mean extinction coefficients determined from the Maldives dataset are in good agreement with those from CEPEX. For the remaining temperature intervals the mean extinction coefficients of CEPEX are higher than the corresponding values of the Maldives dataset. All field campaigns, except the Russian one which is based on 20 years of measurements, show a decrease of the extinction coefficients with temperature.

Beside some similarities between the lidar and the aircraft data noted above, a strong variation in the determined mean extinction coefficients is obvious from Fig. 5.11. Differences result from different instrumentation of the aircraft and from datasets that are limited to specific cirrus types (Heymsfield and McFarquhar 2002). It should be noted that the extinction coefficients of the aircraft measurements were calculated from the cross-sectional area of the probed ice particles. For typical ice crystals and visible wavelengths, the volume extinction coefficient is just twice the cross-sectional area, because the extinction efficiency is approximately two under typical atmospheric conditions (Heymsfield and McFarquhar 2002).

Figure 5.12 shows the dependence of optical depth (a), extinction coefficient (b), and lidar ratio (c) on mid-cloud temperature for all single data points. Crosses represent the NE monsoon data and triangles the SW monsoon data. The horizontal lines in Fig. 5.12 (a) indicate the thresholds for cirrostratus, thin cirrus, and subvisible cirrus. Most data points for temperatures above -40 °C are in the optical-depth range

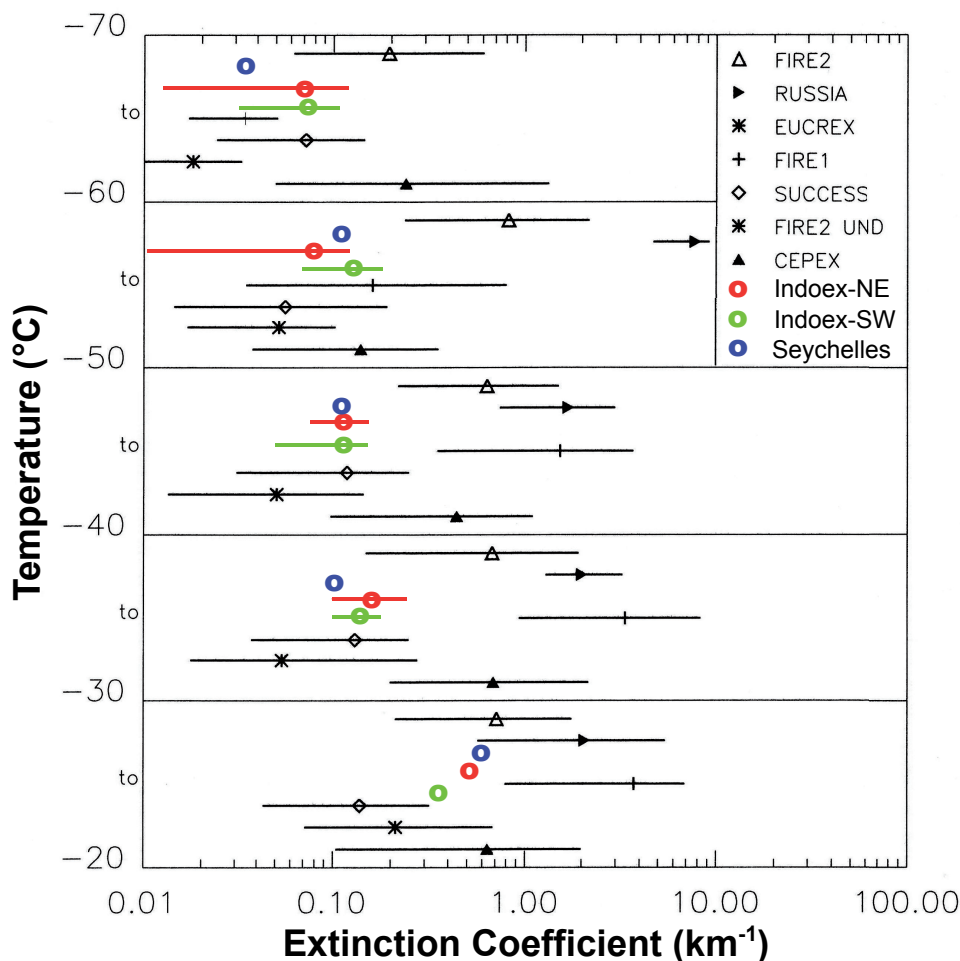


Figure 5.11: Mean cloud extinction coefficient in dependence on temperature for various field campaigns. The red, green, and blue circles were added to the original figure from Heymsfield and McFarquhar (2002) and show the distributions for the NE monsoon, the SW monsoon and the Seychelles (Pace et al. 2003), respectively.

of cirrostratus. This corroborates the hypothesis that deep convection dominates the cirrus formation process at temperatures above $-40\text{ }^{\circ}\text{C}$.

Despite the relatively strong scattering of the data points, the decrease of the optical depth [Fig. 5.12 (a)] and the mean cloud extinction coefficient [Fig. 5.12 (b)] with temperature is an unambiguous characteristic of these two parameters. The data points of both parameters spread over more than two orders of magnitude. Cirrus clouds of the NE monsoon expand the spectra of optical depth and extinction coefficient to lower temperatures down to $-82\text{ }^{\circ}\text{C}$. Cirrus cases of the SW monsoon, on the other hand, provide values for temperatures above $-35\text{ }^{\circ}\text{C}$.

A slope similar to the one of the mean cloud extinction coefficient in Fig. 5.12 (b) was also reported by Pace et al. (2003). In general, the results presented in other studies (Pace et al. 2003; Sunilkumar and Parameswaran 2005) are in good agreement with the distribution of the extinction coefficient presented in Fig. 5.12 (b). It should also be noted that all of them show the same magnitude of variation.

Whereas the mean values of $S \approx 19$ sr for the SW monsoon and of $S \approx 21$ sr for the NE monsoon do not differ considerably, the single values in Fig. 5.12 (c) show a strong variation, especially in the temperature range between -50 and $-70\text{ }^{\circ}\text{C}$. Model results for optical properties of ice crystals with weak shape distortion (slight deviations from the perfect hexagonal structure, rough surface) may help to explain the observed variation of S . They show that column-like crystals mostly produce lidar ratios of the order of 5–20 sr, whereas plate-like crystals lead to lidar ratios in the range of 10–35 sr (Reichardt et al. 2002). These values are calculated for single-scattering events. Considering the influence of multiple scattering (see Sec. 3.4.3), the lidar ratios shown in Fig. 5.12 (c) have to be corrected roughly by a factor of 1.5 to obtain single-scattering values. The resulting lidar ratios around 30 sr are consistent with dominant scattering and backscattering by plates.

Columns and plates can best be distinguished by the depolarization measurement, i.e., by determining the ratio of the cross-polarized to the parallel-polarized signal component. This parameter was measured at 710 nm during INDOEX (see Sec. 2.2). Columns cause depolarization ratios around 0.6, whereas plates lead to values lower than 0.3. The INDOEX depolarization observations were of low quality and are not discussed in detail here. However, they indicate in most cases depolarization values below 0.3, disregarding the season. From these observation one can also conclude that the dominating particle shape is the plate-like form.

Model results further indicate that the lidar ratio increases with increasing shape distortion, increasing complexity of the crystal form toward aggregates like bullet rosettes, and increasing size of the particles. Reichardt et al. (2002) concluded

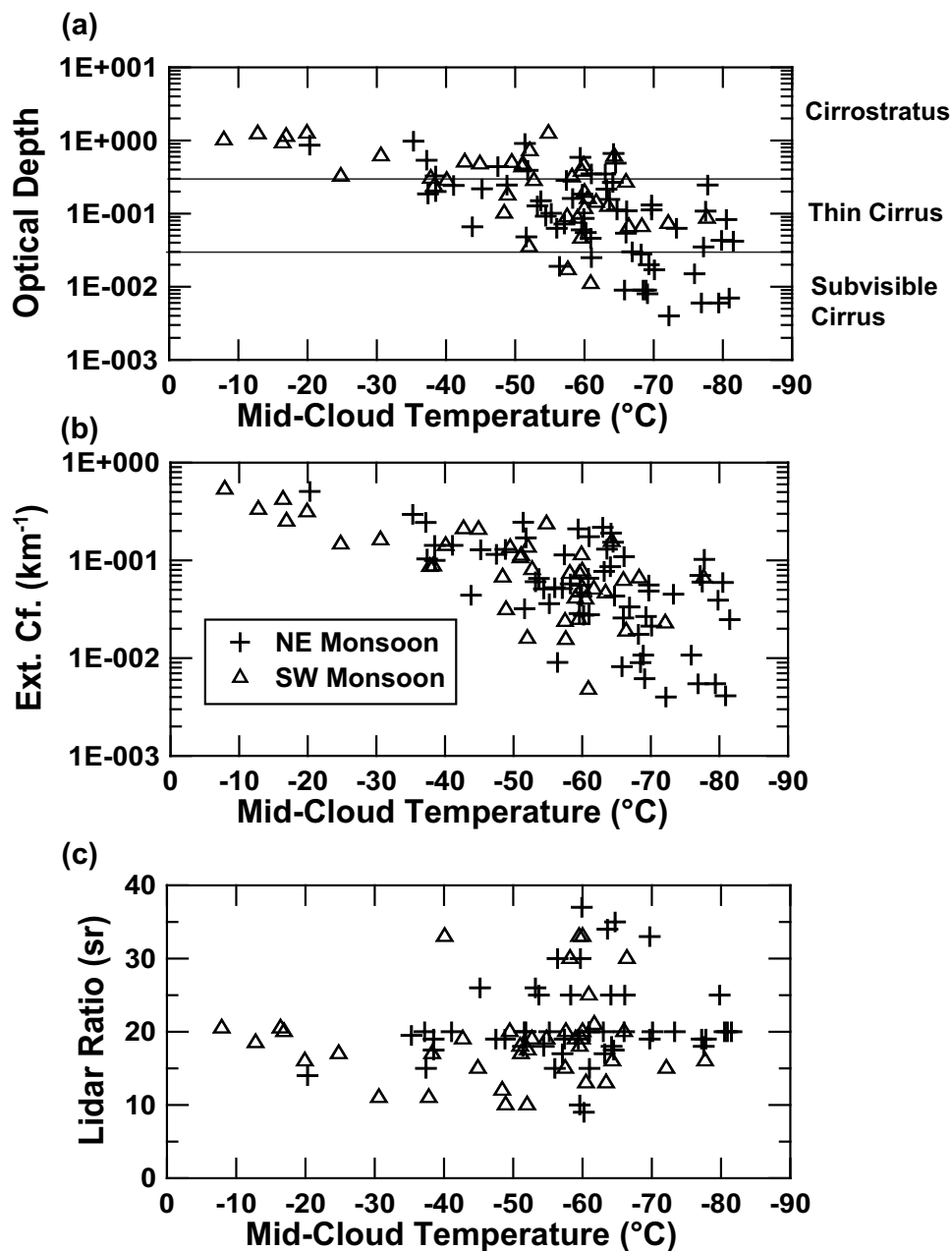


Figure 5.12: (a) optical depth, (b) extinction coefficient, and (c) lidar ratio in dependence on mid-cloud temperature.

that cirrus clouds usually contain crystals of various sizes and shapes, and that the relationship between microphysical and optical properties is not straightforward. In some of the INDOEX cases complex structures may have been present leading to lidar ratios around 40 sr (or 60 sr for single scattering) as shown in Fig. 5.12 (c).

Possible Influence of Anthropogenic Pollution on Cirrus Optical Properties

As discussed in Sec. 4.3, higher concentrations of aerosol particles in the lower troposphere might lead to higher concentrations and smaller sizes of ice particles in cirrus clouds. Because of the suppressed Hallet–Mossop process homogeneous freezing at temperatures below $-37.5\text{ }^{\circ}\text{C}$ is supposed to play a dominant role for the ice production process. Ice nucleation at these temperatures would lead to the formation of regular hexagonal plate- and column-like ice crystals (Hallett et al. 2002). In comparison to cirrus not affected by pollution, the comparably high concentration of ice crystals should lead to higher values of the cloud-mean extinction coefficients and lower lidar ratios during the NE monsoon season.

Table 5.6 shows the mean extinction coefficient $\bar{\alpha}$ and the mean lidar ratio \bar{S} for the NE and SW monsoon seasons. Only cirrus clouds with a base between 10 and 14 km were included in the calculation of the mean values. Lower clouds were excluded from the calculation, because heterogeneous freezing is the dominating ice formation process at temperatures higher than about $-37.5\text{ }^{\circ}\text{C}$ ($\approx 10\text{ km}$). The indirect effect of aerosol particles discussed here is supposed to affect homogeneous freezing only. Above approximately 14 km cloud formation is not directly influenced by deep convection. Thus clouds above 14 km should not be affected by aerosol particles.

The comparison of $\bar{\alpha}$ and \bar{S} of the NE monsoon with those of the SW monsoon in Table 5.6 reveals no statistically significant differences between both seasons. Also when the data points for the period from 9 July to 13 July 1999, for which Franke (2003) reported aerosol layers over Hulule (see Sec. 4.4), are excluded, the mean extinction coefficient and the mean lidar ratio do not change. Thus the expected effect of aerosol particles on the optical cloud properties could not be verified by the comparison of these values of both seasons.

Also the comparison of the INDOEX extinction coefficients with those observed during the CEPEX campaign does not indicate that cirrus clouds over the Maldives are affected by pollution. This is obvious from Fig. 5.11. CEPEX was carried out in the tropical western Pacific. High values of AOD have not been reported in the vicinity of the CEPEX region during the campaign. The extinction coefficients determined

Table 5.6: Seasonal-mean extinction coefficient $\bar{\alpha}$ and lidar ratio \bar{S} of cirrus clouds with base heights between 10 and 14 km. Standard deviations are given in parentheses.

	NE Monsoon		SW Monsoon	
Mean Ext. Cf. $\bar{\alpha}$	0.07	(0.06)	0.06	(0.05)
Mean Lidar Ratio \bar{S}	22	(6)	20	(7)

for cirrus clouds during CEPEX are always higher than the extinction coefficients determined for the Maldives, disregarding seasonal differences.

Parameterization of the Temperature Dependence of the Extinction Coefficient

In order to accurately determine the radiative properties of clouds, improved knowledge on the cirrus extinction coefficient as a function of temperature is a basic requirement (Heymsfield and McFarquhar 2002). Parameterization functions determined from distributions of the extinction coefficient in dependence on temperature are useful to improve cirrus modeling.

The coefficients of one parameterization function derived from the INDOEX dataset is given in Table 5.7. The function is a polynomial function of second order of the form $\bar{\alpha}(T) = A_0 + A_1 T + A_2 T^2$. Only two of these functions derived from lidar data have been published up to now. One is for Gadanki (Sunilkumar and Parameswaran 2005) and one for the mid-latitudes (Sassen et al. 2003). They are also presented in Table 5.7. All three functions together with the measured mean cloud extinction

Table 5.7: Coefficients of a polynomial function of second order to parameterize the mean dependence of cloud extinction coefficient α on temperature for the Maldives, Gadanki (Sunilkumar and Parameswaran 2005), and the mid-latitudes (Sassen et al. 2003). The respective curves are presented in Fig. 5.13.

Coefficients	Polynomial Fit: $\bar{\alpha}(T) = A_0 + A_1 T + A_2 T^2$		
	A_0	A_1	A_2
INDOEX	5.683×10^{-4}	1.375×10^{-5}	8.833×10^{-8}
Gadanki	9.73×10^{-5}	1.9×10^{-6}	9×10^{-9}
Mid-latitudes	7.072×10^{-4}	7.36×10^{-6}	-2.329×10^{-9}

coefficients at the Maldives are shown in Fig. 5.13. A few additional functions that have linear or exponential slopes can be found in the literature. The polynomial function fits best for the INDOEX dataset, at least for temperatures between -80 and -10 °C. As mentioned above, the derived values of the mean extinction coefficient at Gadanki (blue curve) are much smaller than the respective parameters from the Maldives (red curve). Mid-latitude cirrus (green curve) seems to permanently have higher values of the extinction coefficient.

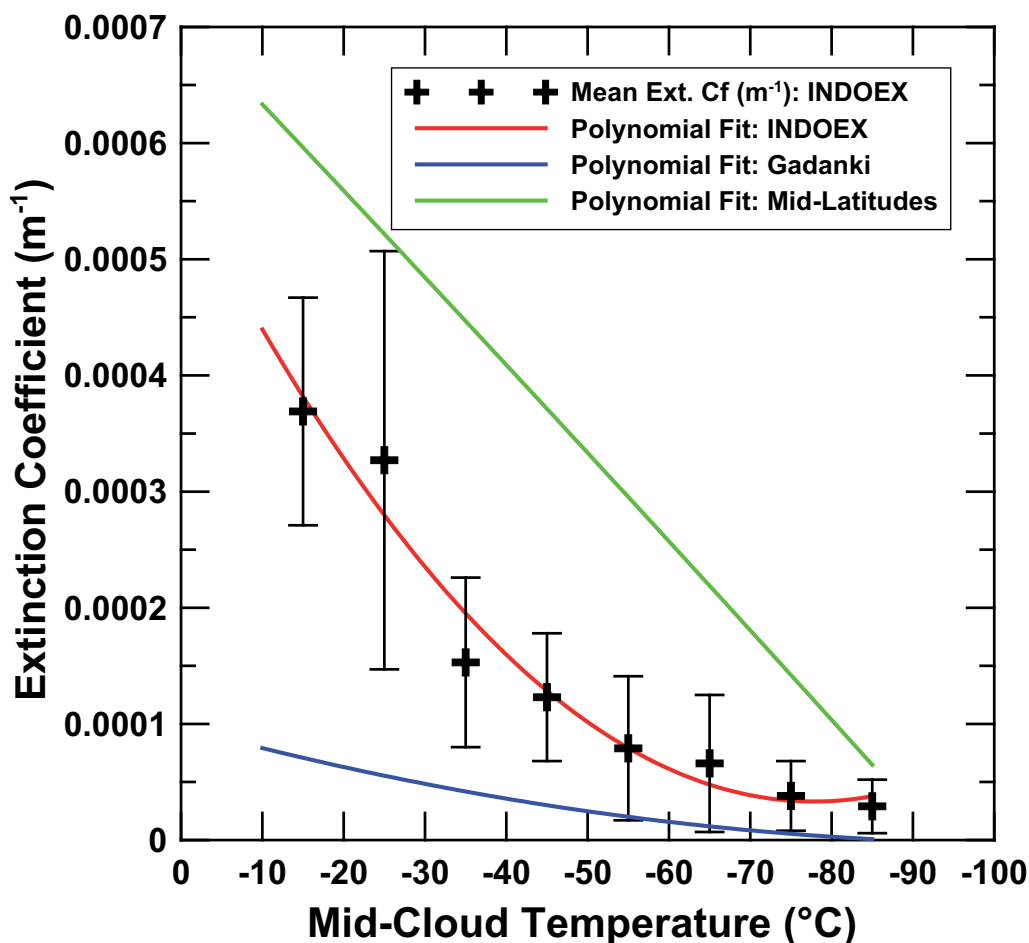


Figure 5.13: Mean extinction coefficient per 10 K temperature interval determined from the entire Maldives dataset (crosses). The red curve shows the polynomial fit function of second-order parameterization of the mean cloud extinction coefficient $\bar{\alpha}$ for the Maldives dataset. The blue curve is the polynomial fit function of the respective Gadanki distribution (Sunilkumar and Parameswaran 2005), and the green curve shows the polynomial fit function of mid-latitude cirrus clouds (Sassen et al. 2003). The corresponding polynomial coefficients are presented in Table 5.7.

Chapter 6

Summary

This diploma thesis presented the first seasonal-dependent, height-resolved cirrus cloud statistics for the tropical Indian Ocean (Hulule, Maldives). The study is not supposed to be a climatology, but its goal is to give an insight in the characteristics of cirrus clouds observed over the Maldives. With lidar data of four separate field campaigns, which covered two seasons of the northeast monsoon and one season of the southwest monsoon, it was possible to examine seasonal characteristics of cirrus cloud properties.

Disregarding the season, deep convection was found to be primarily responsible for the formation and the properties of cirrus clouds up to altitudes of about 14 km. Up to this height the dominant cloud types were outflow cirrus and remnant clouds of cumulonimbus anvils. The analysis of outgoing-longwave-radiation data revealed that deep convection was present within 500 km around the lidar site during most of the time of the southwest monsoon season in July and October 1999. During the northeast monsoon in February and March 1999 and in March 2000 the lidar site had a mean distance to deep convection of about 1000 km. The differences in the convective activity in the vicinity of the Maldives between both seasons are reflected in various cirrus cloud properties. Whereas cirrus was observed during 69% of the time in the SW monsoon season, ice clouds occurred only during 41% of the time in the NE monsoon season. With a geometrical depth of 2.2 km the clouds observed during the SW monsoon were on average about 0.6 km thicker than NE monsoon cirrus. Differences were also found for the optical depth $\bar{\tau}$. During the SW monsoon $\bar{\tau}$ was on average 0.38, with $\bar{\tau} \approx 0.014$ for subvisible cirrus, $\bar{\tau} \approx 0.14$ for thin cirrus, and $\bar{\tau} \approx 0.68$ for cirrostratus. During the NE monsoon season we found $\bar{\tau} \approx 0.18$, with $\bar{\tau} \approx 0.014$ for subvisible cirrus, $\bar{\tau} \approx 0.13$ for thin cirrus, and $\bar{\tau} \approx 0.57$ for cirrostratus. The mean cloud extinction coefficient $\bar{\alpha}$ did not vary considerably between both monsoon seasons. $\bar{\alpha}$ was on average 0.06, with values ranging from $\bar{\alpha} \approx 0.013 \text{ km}^{-1}$ for subvisible cirrus, $\bar{\alpha} \approx 0.07 \text{ km}^{-1}$ for thin cirrus, and $\bar{\alpha} \approx 0.22 \text{ km}^{-1}$ for cirrostratus.

Different indications were found which suggest that cirrus clouds with a base above about 14 km have different properties than clouds below 14 km. Clouds above 14 km, which represented 14% of all observed clouds, were on average only 0.8 km thick. Clouds with a base below 14 km, in contrast, had a geometrical depth of about 2 to 3.3 km. In addition, it was found that there were two maxima in the average distance of the cloud tops to the mean lapse-rate tropopause. One maximum was located directly at the tropopause. A second maximum was found about 3 km below the tropopause. As stated above, cirrus clouds with base heights below 14 km were most likely formed by deep convection. The geometrically thin clouds close to the tropopause with a base above 14 km were, in contrast, most likely formed by large-scale processes such as gravity waves and Kelvin waves. Downward-propagating stratospheric Kelvin waves, already reported by Boehm and Verlinde (2000), were also found in the analyzed radiosonde data of INDOEX. They are supposed to support cirrus formation by adiabatic cooling (Jensen et al. 1996).

The temperature information derived from radiosonde measurements was also used to determine the temperature dependence of cirrus optical depth, mean extinction coefficient, and extinction-to-backscatter ratio (lidar ratio). It was found that optical depth and extinction coefficient decrease with decreasing temperature. The slope of the extinction coefficient was parameterized by a polynomial function of second order. Because the extinction coefficient strongly depends on microphysical cloud properties, the parameterization may help to improve modeling of cirrus radiative processes. A correlation between lidar ratio and temperature could not be found. The comparison of the derived lidar ratios with modeling studies suggests that the clouds observed during INDOEX most likely consisted of plate-like ice particles which produced lidar ratios of about 20 sr. A lidar ratio of 20 sr is the average value determined from all analyzed cirrus cases. Only a few cirrus clouds produced lidar ratios up to 40 sr which indicate irregular crystal shapes.

The comparison of the derived geometrical and optical properties with other tropical cirrus statistics revealed regional differences. Top heights of cirrus clouds over the western Pacific Ocean are on average about 2 km higher than the ones measured during INDOEX. The geometrical cirrus properties observed over central India and the Seychelles are generally in good agreement with the INDOEX dataset. The frequency of subvisible cirrus with an optical depth $\tau < 0.03$ over the Maldives was 18%. Statistics for the western Pacific, Central India, the Seychelles, and Réunion Island report higher frequencies of subvisible cirrus clouds. Nevertheless, all publications show a similar decrease of the extinction coefficient with temperature as found at the Maldives, even though the parameterization functions vary.

Analysis of backward trajectories, AVHRR aerosol optical depth, and OLR data

revealed indications that the cirrus clouds over the Maldives were affected by anthropogenic aerosols. This seemed especially to be the case during the NE monsoon, when northeasterly winds dominated the circulation and advected aerosol layers from Southeast Asia to the Maldives. However, an indirect aerosol effect on the cirrus cloud optical properties, expressed by higher extinction coefficients and lower lidar ratios, could not be found. The derived extinction coefficients of the northeast and the southwest monsoon do not differ considerably. Also the lidar ratios do not show the supposed seasonal difference that would indicate an influence of aerosol particles on the number concentration and the size of the ice particles. This does not mean that there is generally no aerosol effect on the cirrus properties. However, the lidar data cannot be used to identify such an effect. Furthermore, because the meteorological conditions vary between both seasons, a comparison is not easy to perform. Cirrus clouds during the northeast monsoon season most likely form in larger distance to the Maldives than during the southwest monsoon. Hence, the evolution state of the observed clouds may be different during both seasons. This should also affect the ice particle properties. In addition, continental aerosol layers were present over the Maldives also during the southwest monsoon. They may have influenced the SW monsoon statistics as well.

Appendix A

List of Abbreviations

AOD	Aerosol Optical Depth
AVHRR	Advanced Very High Resolution Radiometer
Bsc. Cf.	Backscatter Coefficient
CCN	Cloud Condensation Nuclei
CDC	Climate Diagnostics Center
CEPEX	Central Pacific Experiment
ECMWF	European Centre for Medium-Range Weather Forecast
Ext. Cf.	Extinction Coefficient
IFT	Leibniz Institute for Tropospheric Research
INDOEX	Indian Ocean Experiment
INSAT	Indian National Satellite
IPCC 2001	Intergovernmental Panel on Climate Change 2001
ISCCP	International Cloud Climatology Project
ITCZ	Intertropical Convergence Zone
KCO	Kaashidoo Climate Observatory
Laser	Light Amplification by Stimulated Emission of Radiation
Lidar	Light detection and ranging
Meteosat	Meteorological Satellite
Nd:YAG	Neodymium-doped Yttrium Aluminium Garnet
NE	Northeast
NOAA	National Oceanic and Atmospheric Administration
OLR	Outgoing Longwave Radiation

Radar	Radio detection and ranging
RFOV	Receiver Field of View
SAGE II	Stratospheric Aerosol and Gas Experiment II
ScaRaB	Scanner for Radiation Budget
SW	Southwest
SUCCESS	Subsonic aircraft: Contrail & Clouds Effects Special Study
TRMM	Tropical Rainfall Measuring Mission
UTC	Coordinated Universal Time (Hulule UTC = Hulule local time – 5 hours)
WMO	World Meteorological Organization

Bibliography

- Ackerman, T. P., K.-N. Liou, F. P. Valero, and L. Pfister (1988). Heating rates in tropical anvils. *Journal of the Atmospheric Sciences* *45*, 1606–1623.
- Althausen, D., D. Müller, A. Ansmann, U. Wandinger, H. Hube, E. Clauer, and S. Zörner (2000). Scanning 6-wavelength 11-channel aerosol lidar. *Journal of Atmospheric and Oceanic Technology* *17*, 1469–1482.
- Anderson, I. P. and M. R. Bowen (2000). Firezones and the threat to the wetlands of Sumatra, Indonesia. *Forest Fire Prevention and Control Project, Report, available at <http://www.ssffmp.or.id/>*, 58 pp.
- Anderson, I. P., M. R. Bowen, et al. (1999). Vegetation fires in Indonesia: The fire history of the Sumatra provinces 1996–1998 as a predictor of future areas at risk. *Forest Fire Prevention and Control Project, Report, available at <http://www.ssffmp.or.id/>*, 47 pp.
- Ansmann, A. (2002). Molecular-backscatter lidar profiling of the volume-scattering coefficient in cirrus. In D. K. Lynch, K. Sassen, D. O. Starr, and G. L. Stephens (Eds.), *Cirrus*, pp. 197–210. Oxford University Press.
- Ansmann, A. et al. (1993). Lidar network observations of cirrus morphological and scattering properties during the International Cirrus Experiment 1989: The 18 October 1989 case study and statistical analysis. *Journal of Applied Meteorology* *32*, 1608–1622.
- Ansmann, A., M. Riebesell, U. Wandinger, C. Weitkamp, E. Voss, W. Lahmann, and W. Michaelis (1992a). Combined Raman elastic-backscatter lidar for vertical profiling of moisture, aerosol extinction, backscatter, and lidar ratio. *Applied Physics* *55*, 18–28.
- Ansmann, A., U. Wandinger, M. Riebesell, C. Weitkamp, and W. Michaelis (1992b). Independent measurement of extinction and backscatter profiles in cirrus clouds by using a combined Raman elastic-backscatter lidar. *Applied Optics* *31*, 7113–7131.
-

- Bissonnette, L. R. (2005). Lidar and multiple scattering. In C. Weitkamp (Ed.), *Lidar: Range-Resolved Optical Remote Sensing of the Atmosphere*, pp. 43–103. Springer.
- Boehm, M. T. and J. Verlinde (2000). Stratospheric influence on upper tropospheric tropical cirrus. *Geophysical Research Letters* 27, 3209–3212.
- Cadet, B., L. Goldfarb, D. Faduillhe, S. Baldy, V. Giraud, P. Keckhut, and A. Réchou (2003). A sub-tropical cirrus clouds climatology from Réunion Island (21° S, 55° E) lidar data set. *Geophysical Research Letters* 30, 1–30.
- Chung, C. E., V. Ramanathan, D. Kim, and I. A. Podgorny (2005). Global anthropogenic aerosol direct forcing derived from satellite and ground-based observations. *Journal of Geophysical Research* 110, D24207.
- Comstock, J. M., T. P. Ackerman, and G. G. Mace (2002). Ground-based lidar and radar remote sensing of tropical cirrus clouds at Nauru Island: Cloud statistics and radiative impacts. *Journal of Geophysical Research* 107, 4714.
- Fernald, F. G. (1984). Analysis of atmospheric lidar observations: some comments. *Applied Optics* 23, 652–653.
- Franke, K. (2003). *Optische und physikalische Eigenschaften süd- und südostasiatischer Aerosolpartikel: Beobachtungen mit einem Sechswellenlängenlidar auf den Malediven während INDOEX*. Ph. D. thesis, Leibniz Institute for Tropospheric Research, 97 pp.
- Franke, K., A. Ansmann, D. Müller, D. Althausen, C. Venkataraman, M. S. Reddy, F. Wagner, and R. Scheele (2003). Optical properties of the Indo-Asian haze layer over the tropical Indian Ocean. *Journal of Geophysical Research* 108, 4059.
- Gosh, A. K., K. K. K. Sivakumar, and A. R. Jain (2001). VHR radar observations of atmospheric winds, associated shears and Cn^2 at a tropical location: Interdependence and seasonal pattern. *Annales Geophysicae* 19, 965–973.
- Hallett, J., W. P. Arnott, M. P. Bailey, and J. T. Hallett (2002). Ice crystals in cirrus. In D. K. Lynch, K. Sassen, D. O. Starr, and G. L. Stephens (Eds.), *Cirrus*, pp. 41–77. Oxford University Press.
- Hallett, J. and S. C. Mossop (1974). Production of secondary ice particles during the riming process. *Nature* 249, 26–28.
- Hartmann, D. L., J. Holton, and Q. Fu (2001). The heat balance of the tropical tropopause, cirrus and stratospheric dehydration. *Geophysical Research Letters* 28, 1969–1972.
-

- Heymsfield, A. J. and G. McFarquhar (1996). High albedos of cirrus in the tropical Pacific warm pool: microphysical interpretations from CEPEX and from Kwajalein, Marshall Islands. *Journal of the Atmospheric Sciences* 53, 2424–2451.
- Heymsfield, A. J. and G. M. McFarquhar (2001). Microphysics of INDOEX clean and polluted trade cumulus clouds. *Journal of Geophysical Research* 106, 26,653–28,676.
- Heymsfield, A. J. and G. M. McFarquhar (2002). Mid-latitude and tropical cirrus. In D. K. Lynch, K. Sassen, D. O. Starr, and G. L. Stephens (Eds.), *Cirrus*, pp. 78–101. Oxford University Press.
- Heymsfield, A. J., K. M. Miller, and J. D. Spinhirne (1990). The 2728 October 1986 FIRE IFO cirrus case study: cloud microstructure. *Monthly Weather Review* 118, 2313–2328.
- Heymsfield, A. J. and L. M. Miloshevich (1995). Relative humidity and temperature influences on cirrus formation and evolution: observations from wave clouds and FIRE II. *Journal of the Atmospheric Sciences* 52, 4302–4326.
- Heymsfield, A. J. and R. M. Sabin (1989). Cirrus crystal nucleation by homogeneous freezing of solution droplets. *Journal of the Atmospheric Sciences* 46, 2252–2264.
- Highwood, E. J. and B. J. Hoskins (1998). The tropical tropopause. *Quarterly Journal of the Royal Meteorological Society* 124, 1579–1604.
- Holton, J. R. (1992). Middle atmosphere dynamics. In *An Introduction to Dynamic Meteorology* (3rd ed.), pp. 402–432. Academic Press.
- Ignatov, A., J. Sapper, S. Cox, I. Laszlo, N. R. Nalli, and K. B. Kidwell (2004). Operational aerosol observations (AEROBS) from AVHRR/3 on board NOAA-KLM satellites. *Journal of Atmospheric and Oceanic Technology* 21, 3–26.
- Ignatov, A. and L. Stowe (2002). Aerosol retrievals from individual AVHRR channels. Part I: retrieval algorithm and transition from Dave to 6S radiative transfer model. *Journal of the Atmospheric Sciences* 59, 313–334.
- IPCC (2001). *Climate Change 2001: The Scientific Basis*. Cambridge University Press, 314–416.
- Jensen, E. J., O. B. Toon, H. B. Selkirk, J. D. Spinhirne, and M. R. Schoeberl (1996). On the formation and persistence of subvisible cirrus clouds near the tropical tropopause. *Journal of Geophysical Research* 101, 21,361–20,735.
- Klett, J. D. (1981). Stable analytical solution for processing lidar returns. *Applied Optics* 20, 211–220.
-

- Krishna Murthy, B. V., K. Parameswaran, and K. O. Rose (1986). Temporal variations of the tropical tropopause characteristics. *Journal of the Atmospheric Sciences* 43, 914–922.
- Liebmann, B. and C. A. Smith (1996). Description of a complete (interpolated) outgoing longwave radiation dataset. *Bulletin of the American Meteorological Society* 77, 1275–1277.
- Liou, K. N. (1986). Influence of cirrus clouds on weather and climate processes: A global perspective. *Monthly Weather Review* 114, 1167–1199.
- Liu, C. and E. J. Zipser (2005). Global distribution of convection penetrating the tropical tropopause. *Journal of Geophysical Research* 110, D23104.
- Liu, G., H. Shao, J. A. Coakley, J. A. Curry, J. A. Haggerty, and M. A. Tschudi (2003). Retrieval of cloud droplet size from visible and microwave radiometric measurements during INDOEX: Implication to aerosols' indirect radiative effect. *Journal of Geophysical Research* 108, 4006.
- Lohmann, U. and J. Feichter (2005). Global indirect aerosol effects: a review. *Atmospheric Chemistry and Physics* 5, 715–737.
- Lynch, D. K. and K. Sassen (2002). Subvisual cirrus. In D. K. Lynch, K. Sassen, D. O. Starr, and G. L. Stephens (Eds.), *Cirrus*, pp. 256–264. Oxford University Press.
- Lynch, D. K., K. Sassen, D. O. Starr, and G. Stephens (2002). Preface. In D. K. Lynch, K. Sassen, D. O. Starr, and G. Stephens (Eds.), *Cirrus*. Oxford University Press.
- Marquart, S., M. Ponater, F. Mager, and R. Sausen (2003). Future development of contrail cover, optical depth and radiative forcing: impacts of increasing air traffic and climate change. *Journal of Climate* 16, 2890–2904.
- Massie, S., A. Gettelman, and W. Randel (2002). Distribution of tropical cirrus in relation to convection. *Journal of Geophysical Research* 107, 4591.
- Mattis, I. (1996). Zeitliche Entwicklung des stratosphärischen Aerosols nach dem Ausbruch des Pinatubo: Analyse von Raman-Lidarmessungen. Diploma thesis, University of Leipzig. 132 pp.
- Mattis, I. (2002). *Aufbau eines Feuchte-Temperatur-Aerosol-Ramanlidars und Methodenentwicklung zur kombinierten Analyse von Trajektorien und Aerosolprofilen*. Ph. D. thesis, University of Leipzig. 67 pp.
- Mazin, I. (1995). Cloud water content in continental clouds of middle latitudes. *Atmospheric Research* 35, 283–297.
-

- McFarquhar, G. M., A. J. Heymsfield, J. Spinhire, and B. Hart (2000). Thin and subvisual tropopause tropical cirrus: Observations and radiative impacts. *Journal of the Atmospheric Sciences* 57, 1841–1853.
- Minnis, P., L. Nguyen, D. P. Duda, and R. Palikonda (2002). Spreading of isolated contrails during the 2001 air traffic shutdown. In *Proceedings of the 10th AMS Conf. Aviation, Range, and Aerospace Meteorol.*, Portland, OR, May 13-16, 33-36.
- Mossop, S. C. and J. Hallett (1974). Ice crystal concentration in cumulus clouds: Influence of the drop spectrum. *Science* 186, 632–634.
- Müller, D., K. Fanke, A. Ansmann, D. Althausen, and F. Wagner (2003). Indo-Asian pollution during INDOEX: Microphysical particle properties and single scattering albedo inferred from multiwavelength lidar observations. *Journal of Geophysical Research* 108, 4600.
- Pace, G., M. Gacciani, A. di Sarra, G. Fiocco, and D. Fuà (2003). Lidar observations of equatorial cirrus clouds at Mahé, Seychelles. *Journal of Geophysical Research* 108, 4236.
- Platt, C. M. R. and A. C. Dilley (1981). Remote sounding of high clouds. IV: Observed temperature variations in cirrus optical properties. *Journal of the Atmospheric Sciences* 38, 1069–1082.
- Platt, C. M. R., S. C. Scott, and A. C. Dilley (1987). Remote sounding of high clouds. Part VI: Optical properties of midlatitude and tropical cirrus. *Journal of the Atmospheric Sciences* 44, 729–747.
- Platt, C. M. R., J. D. Spinhire, and W. D. Hart (1989). Optical and microphysical properties of a cold cirrus cloud: Evidence for regions of small ice particles. *Journal of Geophysical Research* 94, 11,151–11,164.
- Pruppacher, H. R. and J. D. Klett (1997). *Microphysics of Clouds and Precipitation*. Springer, 954 pp.
- Ramanathan, V., J. Coakley, A. Clarke, W. Collins, et al. (1996). U.S. INDOEX proposal. <http://www-indoex.ucsd.edu/publications/proposal/>.
- Ramanathan, V. and W. Collins (1991). Thermodynamic regulation of ocean warming by cirrus clouds deduced from observations of the 1987 El Niño. *Nature* 351, 27–32.
- Ramanathan, V., P. Crutzen, J. T. Kiehl, and D. Rosenfeld (2001b). Aerosols, climate, and the hydrological cycle. *Science* 294, 2119–2124.
-

- Ramanathan, V., P. J. Crutzen, J. Lelieveld, A. P. Mitra, D. Althausen, et al. (2001a). Indian Ocean Experiment: An integrated analysis of the climate forcing and effects of the great Indo-Asian haze. *Journal of Geophysical Research* 106, 28,371–28,398.
- Raschke, E., P. Flamant, Y. Fouquart, P. Hignett, H. Isaka, P. Jonas, H. Sundquist, and P. Wendling (1998). Cloud radiation studies during the european cloud and radiation experiment (EUCREX). *Surveys in Geophysics* 19, 89–138.
- Reichardt, J., S. Reichardt, M. Hess, and T. J. McGee (2002). Correlations among the optical properties of cirrus-cloud particles: Microphysical interpretation. *Journal of Geophysical Research* 107, 4562.
- Rosenfeld, D. (2000). Suppression of rain and snow by urban and industrial air pollution. *Science* 287, 1793–1796.
- Rosenfeld, D. and W. L. Woodley (2000). Deep convective clouds with sustained supercooled liquid water down to -37.5 degrees. *Nature* 405, 440–442.
- Sassen, K. (1997). Contrail cirrus and their potential for regional climate change. *Bulletin of the American Meteorological Society* 78, 1885–1903.
- Sassen, K., R. P. Benson, and J. D. Spinhirne (2000). Tropical cirrus cloud properties from TOGA/COARE airborne polarization lidar. *Geophysical Research Letters* 27, 673–676.
- Sassen, K. and B. S. Cho (1992). Subvisual thin cirrus lidar data set for satellite verification and climatological research. *Journal of Applied Meteorology* 31, 1275–1285.
- Sassen, K. and J. M. Comstock (2001). A midlatitude cirrus cloud climatology from the Facility for Atmospheric Remote Sensing. Part III: Radiative properties. *Journal of the Atmospheric Sciences* 58, 2113–2127.
- Sassen, K., M. K. Griffin, and G. C. Dodd (1989). Optical scattering and microphysical properties of subvisual cirrus clouds, and climatic implications. *Journal of Applied Meteorology* 28, 91–98.
- Sassen, K., Z. Wang, C. M. R. Platt, and J. M. Comstock (2003). Parameterization of infrared absorption in midlatitude cirrus clouds. *Journal of the Atmospheric Sciences* 60, 428–433.
- Scheele, M., P. Sigmund, and P. van Velthoven (1996). Sensitivity of trajectories to data resolution and its dependence on the starting point: in or outside the tropopause fold. *Meteorology Applied* 3, 267–273.
-

- Schiffer, R. A. and W. Rossow (1983). The International Satellite Cloud Climatology Project (ISCCP): The first project of the World Climate Research Programme. *Bulletin of the American Meteorological Society* 64, 779–784.
- Sivakumar, V., Y. Bhavanikumar, P. B. Rao, K. Mizutani, T. Aoki, M. Yasui, and T. Itabe (2003). Lidar observed characteristics of the tropical cirrus clouds. *Radio Science* 38, 1094.
- Stephens, G. L. (2002). Cirrus, climate, and global change. In D. K. Lynch, K. Sassen, D. O. Starr, and G. L. Stephens (Eds.), *Cirrus*, pp. 433–448. Oxford University Press.
- Sunilkumar, S. V. and K. Parameswaran (2005). Temperature dependence of tropical cirrus properties and radiative effects. *Journal of Geophysical Research* 110, D13205.
- Toon, O. B. and R. C. Mialke-Lye (1998, April). Subsonic aircraft: Contrail and cloud effects special study (SUCCESS). *Geophysical Research Letters* 25, 1109–1112.
- Twomey, S. (1974). Pollution and the planetary albedo. *Atmospheric Environment* 8, 1251.
- Wandinger, U. (1998). Multiple-scattering influence on extinction- and backscatter-coefficient measurements with Raman and high-spectral-resolution lidars. *Applied Optics* 37, 417–427.
- Wandinger, U. (2005). Introduction to lidar. In C. Weitkamp (Ed.), *Lidar: Range-Resolved Optical Remote Sensing of the Atmosphere*, pp. 1–18. Springer.
- Wang, P. H., P. Minnis, M. P. McCormick, G. S. Kent, and K. M. Skeens (1996). A 6-year climatology of cloud occurrence frequency from Stratospheric Aerosol and Gas Experiment II observations (1985–1990). *Journal of Geophysical Research* 101, 29,407–29,429.
- Wendisch, M., P. Pilewskie, J. Pommier, S. Howard, P. Yang, A. Heymsfield, C. G. Schmitt, D. Baumgardner, and B. Mayer (2005). Impact of cirrus crystal shape on solar spectral irradiance: A case study for subtropical cirrus. *Journal of Geophysical Research* 110, D03202.
- Winker, D. M. and C. R. Trepte (1998). Lamina cirrus observed near the tropical tropopause by LITE. *Geophysical Research Letters* 25, 3351–3354.
- WMO (1975). *International Cloud Atlas*. Volume I. WMO Publ. 407, World Meteorological Organization. 155 pp.
-

Wylie, D. P., W. P. Menzel, H. M. Woolf, and K. I. Strabala (1994). Four years of global cirrus cloud statistics using HIRS. *Journal of Climate* 7, 1972–1986.

Acknowledgments

This diploma thesis was written from 1 February 2005 to 30 January 2006 at the Leibniz Institute for Tropospheric Research. Between 13 June and 31 July 2005 I did an internship at the National Center for Atmospheric Research (NCAR) in Boulder (CO, USA). The goal of the internship was to find indications for the anthropogenic effect of aerosol particles on cirrus clouds and to verify the indications with satellite and lidar data.

Without the support of several people my studies would not have been as enjoyable and fruitful as they were. Therefore I would like to say thank you to:

- Albert Ansmann for his excellent supervision of my thesis work at the IFT. At the NCAR I was supervised by Andrew J. Heymsfield and Steven T. Massie who did a great job as well. In this scope I would also like to say thank you to Kathleen Franke who was my adviser at the IFT before I started with my diploma thesis. Together we created the basic INDOEX cirrus cloud dataset.
- Prof. J. Heintzenberg and Prof. G. Tetzlaff for reviewing this diploma thesis. I would also like to thank them for their support of my internship by writing the references I needed for the application for a grant from the Deutscher Akademischer Austauschdienst (DAAD).
- Detlef Müller for supporting me in the organization and preparation for the internship at the NCAR
- Ulla Wandinger, Albert Ansmann and Heike Eichler for proof reading this thesis
- Larry Miloshevich, Steven T. Massie, Kathleen Franke, Ulla Wandinger, Dietrich Althausen, Albert Ansmann, and Stefan Horn for providing me program code and knowledge that made data processing more convenient
- my fellow students for the great time we had during the last years

At the end I would like to say a few words in German to my family:

Ein herzliches Dankeschön gilt meinen Eltern und Großeltern für die moralische und finanzielle Unterstützung während des Studiums! Ohne sie wäre wohl alles ganz anders gekommen.

Statement of Authenticity

This diploma thesis contains no material which has been accepted for the award of any other degree or diploma in any tertiary institution, and to the best of the author's knowledge and belief, this diploma thesis contains no copy or paraphrase of material previously published or written by another person, except where due reference is made in the text of this thesis.

Upon positive assessment, copies of this diploma thesis will be provided for the libraries of the Faculty of Physics and Earth Sciences, University of Leipzig, and the Leibniz-Institute for Tropospheric Research, Leipzig.

Leipzig, January 30, 2006

.....
Patric Seifert